Thèse

présentée à

l'Université Pierre et Marie Curie

Ecole doctorale de Physique de la Particule à la Matière Condensée

par

Lucile Veissier

pour le titre de Docteur

Specialité Optique Quantique

Quantum memory protocols in large cold atomic ensembles

Soutenue le 5 décembre 2013 devant le jury composé de

Mme Maria CHAMARRO	Examinateur
M. Thierry CHANELIERE	Rapporteur
M. Jürgen ESCHNER	Rapporteur
Mme Elisabeth GIACOBINO	Membre invité
M. Julien LAURAT	Directeur de thèse
M. Hugues DE RIEDMATTEN	Examinateur
M. Yvan SORTAIS	Examinateur

Abstract

Quantum memories are an essential building block for quantum information science, and in particular for the implementation of quantum communications across long distances. A quantum memory is defined as a system capable of storing and retrieving quantum states on-demand, such as quantum bits (qubits). Atomic ensembles are good candidates for this purpose because they enables strong light-matter coupling in case of a large number of atoms. Moreover, the collective effect, enhanced in the regime of large optical depth, can lead to storage efficiency close to unity. Thus, in this thesis, a large magneto-optical trap for cesium atoms is used as a atomic medium in order to implement a quantum memory protocol based on electromagnetically induced transparency (EIT).

First, the EIT phenomenon is studied through a criterion for the discrimination between the EIT and the Autler-Townes splitting models. We then report on the implementation of an EIT-based memory for photonic qubits encoded in orbital angular momentum (OAM) of light. A reversible memory for Laguerre-Gaussian modes is implemented, and we demonstrate that the optical memory preserves the handedness of the helical structure at the single-photon level. Then, a full quantum state tomography of the retrieved OAM encoded qubits is performed, giving fidelities above the classical bound. This showed that our optical memory operates in the quantum regime. Finally, we present the implementation of the so-called DLCZ protocol in our ensemble of cold atoms, enabling the generation of heralded single photons. A homodyne detection setup allows us to realize the quantum tomography of the created photonic state.

Key words quantum information science, quantum memories, magneto-optical trap, electromagnetically induced transparency, orbital angular momentum of light, quantum tomography.

Résumé

Les mémoires quantiques sont un élément essentiel dans le domaine de l'information quantique, en particulier pour la mise en œuvre de communications quantiques sur de longues distances. Une mémoire quantique a pour but de stocker un état quantique de la lumière, comme par exemple un bit quantique (qubit), et de le réémettre après un délai donné. Les ensembles atomiques sont de bons candidats pour construire de telles mémoires quantiques, car il est possible d'obtenir de fort couplage lumière-matière dans le cas d'un grand nombre d'atomes. De plus, la notion d'effet collectif, qui est renforcé pour de large profondeur optique, permet en principe une efficacité de stockage proche de l'unité. Ainsi, dans cette thèse, un piège magnéto-optique de césium à forte densité optique est utilisé pour l'implémentation d'un protocole de mémoire quantique basé sur la transparence induite électromagnétiquement (EIT).

Tout d'abord, le phénomène EIT est étudié à travers un critère de discrimination entre les modèles d'EIT et de séparation Autler-Townes. Nous rapportons ensuite la mise en œuvre d'une mémoire basée sur l'EIT pour des qubits photoniques encodés en moment angulaire orbital (OAM) de la lumière. Une mémoire réversible pour des modes de Laguerre-Gauss est réalisée, et nous démontrons que la mémoire optique préserve le sens de la structure hélicoïdale au niveau du photon unique. Ensuite, une tomographie quantique complète des états réémis est effectuée, donnant des fidélités au-dessus de la limite classique. Cela montre que notre mémoire optique fonctionne dans le régime quantique. Enfin, nous présentons la mise en œuvre du protocole dit DLCZ dans notre ensemble d'atomes froids, permettant la génération de photons uniques annoncés. Une détection homodyne nous permet de réaliser la tomographie quantique de l'état photonique ainsi créé.

Mots clés information quantique, mémoire quantique, piège magnéto-optique, tranparence induite électromagnétiquement, moment angulaire orbital de la lumière, tomographie quantique.

Remerciements

Ce travail de thèse a été mené au Laboratoire Kastler Brossel, au sein de l'équipe d'Optique Quantique, de septembre 2010 à décembre 2013. Je remercie donc les directeurs successifs du laboratoire, Paul Indelicato et Antoine Heidmann, pour leur accueil. Je remercie également chaleureusement tous les membres du laboratoire, permanents, post-doc, thésards, administratifs, techniciens ou ingénieurs.

Mes plus grands remerciements vont bien évidemment à mon directeur de thèse, Julien Laurat. Depuis mon master, il a guidé la débutante que j'étais dans le monde de la recherche. Durant toute ma thèse j'ai pu profiter de ses bonnes intuitions, en particulier sur la partie expérimentale, de sa disponibilité, mais également de ses visions bien définies, aussi bien au niveau du travail à mener dans l'équipe que du fonctionnement plus général de la recherche. J'ai aussi pu contempler son succès durant ces années. A mon arrivée en stage de M1, c'est Julien, jeune maître de conférence très présent en salle de manip, qui m'a appris les bases, comme coupler de la lumière dans une fibre. Quatre années et un ERC plus tard, le professeur Laurat est à la tête d'une grande équipe, et je suis très fière d'en avoir fait partie. Je remercie également ma co-encadrante de thèse Elisabeth Giacobino pour ses conseils réalistes et plein d'expériences. Je tiens aussi à remercier les autres permanents de l'équipe d'Optique Quantique, Claude Fabre, Nicolas Treps, Alberto Bramati et Quentin Glorieux, nouvellement arrivé.

Je me dois de remercier très chaleureusement tous les membres de l'équipe "mémoires quantiques" avec lesquels j'ai travaillé pendant presque 4 ans dans une très bonne ambiance. Je commence par remercier les plus anciens, Sidney, pour sa gentillesse et sa franchise, qui a été un excellent professeur de Labview, Michael, plein de bonne humeur et d'astuces très pertinentes, avec qui travailler a été un grand plaisir, et Oxana pour son expertise théorique sur les atomes froids et son ouverture d'esprit. Je remercie ensuite Lambert pour m'avoir initié sur le MOT, Adrien pour les discussions fructueuses, Sasha pour sa patience à travailler avec des expérimentateurs, Dominik pour son encadrement bienveillant et Baptiste pour son naturel. Juste avant la rédaction, j'ai eu le plaisir de partager l'expérience avec Valentina, post-doc déterminée et souriante, et Pierre, jeune thésard au caractère doux et vif à la fois. Ils ont très vite pris la relève du MOT, et je les remercie pour s'être battus pour la manip, mais aussi pour m'avoir supportée les derniers mois de ma thèse. Je leur souhaite bonne chance et plein de réussites pour la suite. Une pensée également pour Itay, Ben et Hans qui sont venus des quatre coins du monde passer chacun quelques mois de leur thèse dans notre équipe.

Je tiens à remercier Jeff Kimble pour son accueil dans son équipe durant quelques mois de stage au printemps 2010. J'ai énormément appris au contact de Kyung et Aki, que je remercie pour leur patience et leur gentillesse. Je veux aussi remercier Nicolas Sanguard, qui m'a donné un premier goût pour l'information quantique et les mémoires quantiques durant un projet bibliographique effectué en 2008.

Je remercie également chaleureusement les membres de mon jury de thèse, Maria Chamarro, Thierry Chanelière, Jürgen Eschner, Hugues de Riedmatten et Yvan Sortais, pour leur précieux temps passer à lire mon manuscrit et leurs remarques constructives. Je veux aussi remercier certains collaborateurs de notre équipe, Daniel Felinto, Dimitri Koupriyanov, Ping Koy Lam et Robin Kaiser, avec qui j'ai pu avoir quelques échanges durant ma thèse.

Un merci spécial pour quelques thésards et post-doc spéciaux du LKB : Giulia, avec son accent chantant, nos échanges musicaux (je sais que tu l'attendais), et son infinie gentillesse, Godefroy et son

oreille attentive dans les moments abruptes, Alexandros, mon partenaire de tennis avec son caractère pas si facile mais quand même attachant. Pour les discussions enrichissantes, bienveillantes ou délirantes, et pour les bières après le labo, merci à Claire, Pu, Pierre, Anthony, Romain, Panayotis, Olivier, Hanna, Kun, Virginia, Alberto, Mathieu, Emiliano, Ferruccio, Stefano, Thomas, Daria, Renné, Olivier, Roman, Jonathan, Valérian, Clément, Zhen, Valentin, Jean-François, Alexandre, Chiara, Kévin, Leonhard, Rym, Sandrine, Gabriel, Manuel, Raphaël, Théo, Raul.

Je pense aussi à la promotion DQN 2010 : Lise, Robert-Christopher, Juan, Philippe, les deux Olivier, avec qui j'ai passé une excellente dernière année d'étude à Paris 7 et avec qui j'ai continué d'échanger durant ma thèse. Merci à Sara Ducci pour son encadrement et son soutien durant cette année précédant la thèse, et à Thomas Coudreau, que j'ai eu la chance de croiser maintes fois lors de mes années universitaires, en particulier dans mes jurys de stage.

Finalement, j'ai une pensée très forte pour mes parents, Pascal, et mes amis de longue date, Célie, Mikaël, Christine, Jordan, Jérémie, Ahcène, Wesley, Nadir, Julie, avec qui j'ai passé d'excellents moments. Tous m'ont soutenue plus ou moins activement durant ma thèse, et m'ont donné l'occasion de m'échapper de la physique pour quelques heures, de rester en contact avec la "réalité". Un merci particulier à Pascal, pour son immense patience et son soutien quotidien, notamment pendant la dure période de rédaction.

Contents

Introduction

Quantum information and communications

From the eighties, the field of quantum information raised as a natural extension of quantum mechanics, taking advantage of some of the fundamental principles, and amazing properties of quantum mechanics: quantum superposition, non-cloning theorem, and quantum entanglement. The unit of information, defined as a quantum superposition $\alpha|0\rangle + \beta|1\rangle$, and well-known as the quantum bit (qubit), gives to quantum computation the powerful potential of beating computing based on classical resources. In 1981 R. Feynman first proposed to simulate complex problems of quantum mechanics with a quantum computer [Feynman, 1982], and during the nineties, several algorithms for quantum computation were developed [Deutsch and Jozsa, 1992, Shor, 1994, Grover, 1996]. Because of the special role of the measurement in quantum mechanics, an unknown quantum state can not be completely determined with only one measurement. This principle, known as the non-cloning theorem, can be seen as an obstacle for the study of quantum systems, but directly provides a way to secure systems. The example of the famous protocol proposed by Bennett and Brassard [Bennett and Brassard, 1984] illustrates its application to quantum cryptography. Finally, entanglement has been identified as one of the main resource for quantum information. In an entangled system, two particles can not be described independently, even if the two particles are physically very far away from each other. This concept has naturally found a lot of potential applications for the development of quantum communications, where photons are chosen as the quantum information carriers. Quantum communications would aim to connect the nodes of a future "quantum internet" [Kimble, 2008], including for instance quantum teleportation, or quantum key distribution.

However, the distribution of entanglement over long distances suffers from decoherence and losses in optical fibers. A typical example commonly given is the following: the direct transmission of a photon over 1000 km via fibers with 0.2 dB/km loss and with a repetition rate of 10 GHz has a very low success rate, about 10^{-10} Hz, corresponding to a photon transmitted every 300 years. The solution to this problem is the quantum repeater [Briegel et al., 1998, Sangouard et al., 2011], based on the idea of dividing the long distance into shorter segments. The creation of entanglement is realized across each segment, then entanglement swapping is performed between the end nodes of adjacent segments, in order to distribute the entanglement across the whole link. Importantly, this scheme requires quantum memories for synchronization. Indeed, when entanglement has been successfully generated within a segment, the ability to store it allows to wait until the success of entanglement creation in the adjacent segment. The necessary time to distribute entanglement becomes polynomial with the number of segments, whereas it is exponential without quantum memories. Quantum memories are indeed the required tool for achieving scalable networks. The presented PhD works enter into this context.

Quantum memories

A quantum memory is defined as a system capable of storing and retrieving quantum states on-demand. Here we focus on optical quantum memories. Thus, an optical quantum memory must be able to store non-classical states of light, such as single photons, qubit states, entanglement or, in the continuous variable regime, squeezing. Even though quantum repeater is the most commonly cited application of quantum memories, they have been identified as useful devices for a great variety of applications. Quantum computation based on probabilistic quantum gates using linear optics and single-photon sources and photo-detectors [Knill et al., 2001, Kok et al., 2007] will take advantage of the synchronization potential of quantum memories. By storing single-photons, quantum memories can indeed becomes on-demand single photons sources. Furthermore, they can be useful for quantum metrology [Giovannetti et al., 2011], where entanglement between atoms within an ensemble can improve measurement precision.

Benchmarks for quantum memories

Different criteria enable to evaluate the performances of an optical quantum memory, mainly the fidelity, the storage efficiency and the storage time. Others aspects, as the multimode capacity, the bandwidth, or the wavelength of the memory have to be considered as well. Yet, the requirements depend on the targeted application.

Fidelity The fidelity is defined as the overlap between the state to store and the retrieved state. It is one of the main criteria because it allows to talk about *quantum* memory or not. Indeed, an optical memory can be said in the quantum regime only if the fidelity is greater than the maximal fidelity achievable by a classical device. Usually used for this purpose, the prepare-and-resend strategy involves the measurement of the target state, the classical storage of the results, and the preparation of a new state based on them. Then, depending on the input state, the maximal classically achievable fidelity must be estimated and compared with the fidelity obtained experimentally. We mention here that another criterion, the T-V diagram, has been developed to evaluate the storage of Gaussian states [Hétet et al., 2008b].

Efficiency The efficiency corresponds to the probability to retrieve the optical pulse, i.e. the ratio between the energies of the stored and retrieved pulses. This definition can be called unconditional efficiency, as opposed to conditional efficiency, where the calculated probability to retrieve the optical pulse is conditioned by the fact that the pulse has been stored. This second definition is sometimes used for single photons storage, and is of course higher than the first one.

Storage time This criterion is important for long-distance communications. Indeed, for quantum repeater applications the storage time must be larger than the average time for the entanglement creation across the entire repeater, which is few seconds for a 1000 km fiber-link [Sangouard et al., 2011]. However, it is possible to reduce the required storage time to the average time of entanglement creation across an elementary segment via multiplexing [Bussieres et al., 2013]. Moreover, other applications, such as linear-optical quantum computing, implementing in small-scale devices, are less constrained.

Multimode capacity The multimode capacity enables to multiply the repetition rate of the protocols, for quantum repeaters or quantum computation applications. Atomic ensembles are then good candidates for this purpose, where different modes, spatial or temporal, can be stored within the same ensemble. The atomic frequency comb (AFC) protocol is particularly suitable for multimode storage because the multimode capacity does not depend on the optical density, while it scales with the optical density for photon-echo technique, and with the square-root of the optical density for electromagnetically induced transparency (EIT) based protocol [Nunn et al., 2008].

Bandwidth The bandwidth of the memory defines the smallest temporal width of the optical pulses that can be stored. Storing extremely sharp pulses in time can be used to increase drastically the repetition rate, which can be useful in particular for quantum computation.

Wavelength For long-distance quantum communications, the wavelength of the photons that propagate over long distances should be inside the low-loss window for fiber, which is around 1550 nm. Since almost no quantum memory operates at telecommunication wavelengths, other solutions can be implemented. It may be frequency conversion or generation of photon pairs with one photon compatible with the memory, and the other one at telecommunication wavelength.

State of the art

Several review papers well summarize the large quantity of work done in this direction. They focus on atomic ensembles [Lukin, 2003, Kimble, 2008, Lvovsky et al., 2009], trapped ions [Duan and Monroe, 2010], light-matter interaction [Hammerer et al., 2010], photon-echo memories based on solid-state systems [Tittel et al., 2010], quantum memories in the European project "QAP" [Simon et al., 2010], quantum repeaters based on atomic ensembles and linear optics [Sangouard et al., 2011], quantum memories and quantum error correction [Wootton, 2012], and finally on the large range of applications of optical quantum memories [Bussieres et al., 2013]. Here we try to give a brief overview of the different media and protocols used for the implementation of quantum memories, giving remarkable seminal demonstrations, and recent progresses.

Atomic ensembles

Atomic ensembles form the largest family of media for quantum memory implementation, with cold atomic ensembles, warm vapors, and rare-earth doped solids. One of the main requirements for atomic ensemble is a large optical density, leading to a large light-matter coupling.

- Cold atoms

  The ensembles of cold atoms, usually realized with rubidium or cesium atoms, are well-known and well-controlled systems, with very limited inhomogeneous broadening. In this medium, the EIT-based protocol and the DLCZ protocol, both based on collective excitation, are mainly implemented.

EIT-based protocol Based on eletromagnetically induced transparency (EIT), the so-called dynamic EIT protocol [Lukin, 2003] enables the reversible mapping of a quantum state of light through the application of a coupling laser, of which the intensity is dynamically varied. The storage of single photons via dynamic EIT protocol was early demonstrated in 2005 [Chanelière et al., 2005, Eisaman et al., 2005], followed by the reversible mapping of entanglement [Choi et al., 2008]. In the continuous variable regime, the storage of vacuum squeezed states was experimentally demonstrated in 2008 by different groups [Honda et al., 2008, Appel et al., 2008, Arikawa et al., 2010]. The efficiency of the reversible mapping through EIT condition has been widely investigated. For instance, the authors of [Zhang et al., 2011] reported in the classical regime a maximum efficiency of 50 % at a storage time of 100 ns, in an ensemble of cold atoms with a high optical depth of 150. This is in agreement with the work realized in warm vapors [Novikova et al., 2007], where the maximum efficiency is found around 50 %. However, a very recent study of EIT-based storage of bright pulses has reported very high efficiency, of 78 %, with a decay time around 100 µs [Chen et al., 2013]. In the quantum regime, single photons generated by an ensemble of cold atoms via DLCZ have been reversibly mapped with an efficiency of around 50 % into another cold atomic ensemble, with a memory lifetime of the order of 1 µs [Zhou et al., 2012a].

DLCZ protocol Proposed by Duan, Lukin, Cirac and Zoller [Duan et al., 2001], the DLCZ protocol constitutes an elementary segment of a quantum repeater itself. The first step of this protocol, which corresponds to the heralded generation of single photons, has been widely studied. In magneto optical traps (MOT), conditional retrieval efficiency of 50 % was achieved in free space in the J. Kimble's group [Laurat et al., 2006], and of 84 % in cavity in the V. Vuletič's group [Simon et al., 2007], both with strong single-photon character for the retrieved state. An experiment of teleportation was realized via the DLCZ procedure by the group of J.-W. Pan [Chen et al., 2008]. More recently, entanglement among four atomic ensembles within a single MOT cloud was demonstrated [Choi et al., 2010]. Long storage time, of 3.2 ms, and high efficiencies, 80 % at zero storage time and around 30 % at 3.2 ms, have been reported in [Bao et al., 2012], with a MOT in cavity. While the authors were limited to the lifetime of the expending cloud, other groups start operating optical storage in dipole traps. In the group of A. Kuzmich, they achieved storage times of 100 ms, with an efficiency of 16 % at zero storage time, and 5 % after 100 ms, with the conservation of a strong single-photon character [Radnaev et al., 2010]. The authors were also interested in the frequency conversion of the heralding photon to telecommunication wavelength. Finally, very recently, 16 s storage times have been demonstrated via EIT protocol in the classical regime by the same group, with an efficiency of 20 % [Dudin et al., 2013], the authors facing here the limitation due to the lifetime of the optical trap.

Quantum memories based on cold atoms exhibit good efficiencies, high fidelity storage, and long coherence times. The main limitations are their narrow bandwidth and their limited multimodal capacity.

- Warm atomic vapors

In warm atoms, in order to avoid inhomogeneous broadening, the protocols usually involve a Raman scheme, i.e. far off-resonance interactions.

Raman scheme Led by the group of I. Walmsley in Oxford, a special effort has been made to realize a quantum memory at the single-photon level based on warm vapors, via a far-detuned

off-resonant Raman memory scheme. Proposed in [Nunn et al., 2007], this scheme enables the storage of broadband, sub-nanosecond photons. The first demonstration involded 300 ps-long pulses of strong light stored for 12.5 ns [Reim et al., 2010]. However, in far off-resonant protocols, the coupling pulses induce strong noise, which must be suppressed to operate in the single-photon regime. In [Reim et al., 2011], the authors achieve a memory efficiency of 30 %, with a memory time of few μs, for coherent states with a photon mean number of 1.6. The unconditional noise floor produced by the strong Raman control fields being 0.25, the resulting signal-to-noise ratio was around one. Finally, the same group has recently shown the storage of polarization states of light containing $10^3 - 10^4$ photons with high process fidelity, of 97 % at 12.5 ns storage time, and of 87 % after 1.5 μs [England et al., 2012]. Further reduction of the noise is crucial in order to harness the potential of Raman scheme memory in the quantum regime.

Gradient echo memory Based on the well-known photon-echo effect, the gradient echo-memory (GEM) protocol consists in applying a controlled gradient of magnetic field along the atomic vapor cell during the writing process, which induces dephasing of the spin wave. After a user-defined time, the magnetic field is reversed, leading to the rephasing of the spin wave, which can be read out by a strong control pulse. The experimental implementation of this scheme in warm vapors was mostly developed by the group of P. K. Lam [Hétet et al., 2008a]. A coherent pulse sequencer was demonstrated using this technique, where bright pulses were stored and retrieved in an arbitrary order [Hosseini et al., 2009], opening the way towards quantum multimode storage in warm vapors. Via this protocol, the same group reported the storage of bright pulses with an efficiency of 87 %, the highest efficiency to date in any system and a memory time of the order of 10 μs [Hosseini et al., 2011b]. In [Hosseini et al., 2011a], the authors succeeded in reducing the noise induced by the strong coupling pulses to demonstrate the mapping of coherent pulses containing in average less than one photon with 98 % fidelity, thus reaching the quantum regime.

Faraday interaction Here, the non-destructive interaction between the optical polarization and the collective atomic angular momentum enables the implementation of light-matter interface [Hammerer et al., 2010]. The group of E. Polzik focused on this off-resonant interaction, followed by a measurement on light and a successive feedback onto the atoms. In 2001, they demonstrated entanglement between two atomic ensemble [Julsgaard et al., 2001], followed by the first quantum storage via this scheme [**?**]. Then, teleportation between light and matter was shown [Sherson et al., 2006], and very recently between two warm vapors [Krauter et al., 2013]. However, this scheme does not allow a real read out stage, the optical stored state being never retrieved, but estimated from measurements performed on the atomic ensemble.

- Rare-earth doped crystals

Memories based on rare-earth doped crystals take advantage of the long optical and spin coherence times of impurity ions, hosted in a crystalline structure, when cooled to cryogenic temperatures, around 4 K. Indeed, an impressive 1 minute-long storage experiment was realized very recently via EIT protocol with classical light in praseodymium-doped Y_2SiO_5, reaching the limit of population decay [Heinze et al., 2013]. With intrinsic large inhomogeneous broadening, they are specially suitable for the multimode storage of broadband photons via protocols based on photon-echo techniques. However, one of the main drawback of rare-earth doped solids is their limited optical depth.

Controlled reversible inhomogeneous broadening Similar to the gradient echo memory technique, the controlled reversible inhomogeneous broadening (CRIB) procedure first requires the creation of a narrow absorption line by optical pumping. Then, an external electric field produces a controlled inhomogeneous broadening, which is reversed after a certain time to enables the re-emission of the stored light pulse by photon-echo [Tittel et al., 2010]. CRIB was first experimentally demonstrated in europium-doped Y_2SiO_5 by the authors of [Alexander et al., 2006], using bright light pulses. The same group then showed the preservation of coherent information stored via this protocol [Alexander et al., 2007]. However, because of the limited optical depth, the efficiency of the memory process was very low, much less than 1 %. Recently, the authors of [Hedges et al., 2010] increased the effective absorption of the medium, and thus demonstrated the storage and retrieval of classical light, using praseodymium-doped Y_2SiO_5, with an efficiency of 69 %, at a storage time of 1.3 µs, with a decay time of the efficiency of 3 µs. This result corresponds to the best efficiency demonstrated so far in solid-state systems.

Atomic frequency comb protocol The atomic frequency comb (AFC) protocol, also based on photon-echo, has been proposed by the group of N. Gisin [Afzelius et al., 2009]. In this scheme, the broad optical transition of a rare-earth doped crystal is shaped into a comb structure. After the absorption of a light pulse, which covers few peaks of the comb, the collective dipole dephases, but rephases after a time corresponding to the inverse of the periodical structure of the comb. This protocol, leading to a memory with a given, and not user-defined, storage time is called the "two-level" AFC scheme. In order to retrieve on-demand the stored photons, the collective state is transferred onto a spin wave, i.e. into another ground state via an additional laser, and transferred back for re-emission. Following the first demonstration of storage at the single-photon level in solid-state medium [de Riedmatten et al., 2008], the authors of [Sabooni et al., 2010] implemented the "two-level" AFC scheme with 25 % efficiency for a 800 ns-long storage of weak coherent pulses. Embedding the crystal in an impedance-matched cavity allowed then to achieve an efficiency of 56 % after a predetermined storage time of 1 µs with bright pulses [**?**]. In 2011, two groups demonstrated the preservation of entanglement of broadband photons through their quantum storage via the "two level" AFC protocol [Clausen et al., 2011, Saglamyurek et al., 2011], the first group achieving 25 % efficiency at 25 ns storage time. Quantum memories based on rare-earth doped crystals for polarization qubits have been demonstrated [Zhou et al., 2012b, Clausen et al., 2012, Gündoğan et al., 2012]. Finally, the authors of [Rieländer et al., 2013] showed the quantum storage of heralded single photons . However, all these works rely on predetermined storage times, using the "two-level" AFC scheme. The first demonstration of the complete AFC protocol was reported in 2010, showing a 20 µs storage time and an efficiency around the percent at zero storage time in a classical regime [Afzelius et al., 2010]. More recently, the storage and on-demand retrieval of low-power light pulses, containing around 10^4 photons with an efficiency around 5 % and a memory time of 20 µs has been shown [Gündoğan et al., 2013]. In this experiment, five temporal modes have been stored with preserved coherence. The single-photon regime with a complete AFC protocol now is one of the objective [Timoney et al., 2013].

Alternatively to these two main protocols, a less complex protocol has been recently proposed. Based on the simple idea of two-pulse echo, it consists of the retrieval of the stored optical pulse after a secondary rephasing, the primary echo being suppressed. This revival of silenced echo (ROSE) protocol has been experimentally demonstrated [Damon et al., 2011], with an efficiency of 20 % at a 80 µs storage time.

Single quantum systems

Quantum memories can be also be implemented in single quantum systems, such as single atoms in high finesse cavities [Kimble, 2008]. Rencently, polarization qubits were reversibly mapped with an efficiency of 9 %, a fidelity of 93 % after a storage of 2 µs, with a 180 µs decay time [Specht et al., 2011]. The same group of G. Rempe then demonstrated an elementary quantum network based on two remote single-atom memories [Ritter et al., 2012].

Nitrogen-vacancy center (NVC) are investigated by the groups of M. Lukin in Havard, and of R. Hanson in Delft. Entanglement between a photon and a NVC was demonstrated by the authors of [Togan et al., 2010], followed by the demonstration of quantum interference between two photons emitted by NVC [Bernien et al., 2012, Sipahigil et al., 2012]. Very recently, heralded entanglement between two NVC separated by three meters has been shown [Bernien et al., 2013]. NVC are promising systems because of their long memory times, of the order of the second [Maurer et al., 2012]. Others systems, such as quantum dots, are new candidates for the implementation of quantum memories. Recently, entanglement between a photon and a quantum dot was demonstrated [De Greve et al., 2012, Gao et al., 2012].

Context in the group

The group of Quantum Optics at the Laboratoire Kastler Brossel has widely studied light-matter interactions from the quantum optics point of view. An experiment of quantum memory in warm vapors was developed and implemented, based on electromagnetically induced transparency [Dantan et al., 2006, Cviklinski et al., 2008, Ortalo et al., 2009]. EIT phenomenon was also investigated in this system, with the conclusion that it is drastically degraded because of inhomogeneous broadening, and can be recovered by depumping techniques [Mishina et al., 2011, Scherman et al., 2012]. Then, the group chose to implement a quantum memory, still based on EIT, but in cold atom ensembles. A new magneto-optical trap (MOT) was developed, mostly by Lambert Giner who started his PhD in September 2009. The timing part, crucial for experiment involving cold atoms, was realized by Sidney Burks who installed a FPGA system and built programs to gate all the elements of the experiment: laser beams, magnetic fields, and various devices. When I started my PhD in September 2010, my first task was to succeed to the "Labview master", Sidney being finishing his thesis. In October 2010 the laboratory moved, so it involved setting up again everything. From that point we finalized the preparations for the implementation of an EIT-based memory in the single-photon regime, with the participation of Michael Scherman, third-year PhD student at that time. In parallel, we investigated EIT in our ensemble of cold atoms through the test of a proposed criterion for the discrimination between EIT and Autler-Townes splitting (ATS), work mainly done by Lambert Giner and myself. This work showed us that our system was well-controlled, but had some limitations, in particular the influence of the multilevel structure and the residual Doppler broadening. Then, the group was interested in studying the multimode capacity of our memory device, through the storage of various spatial modes. Adrien Nicolas, who started his PhD in September 2011, first investigated the tools for the manipulation of Laguerre-Gaussian modes. As a first step, an EIT-based memory for twisted photons was implemented at the single-photon level, where we studied the characteristics of our memory in terms of efficiency and storage time. In a second step, we realized an original setup to perform the storage and the analysis of qubits encoded in orbital angular momentum. Our results, in the quantum regime, confirmed that our memory preserves OAM encoded photonic qubits, and is therefore a quantum memory. These works were mainly done by Adrien Nicolas, Dominik Maxein in a post-doctoral position, and myself. Finally, we have implemented the

DLCZ scheme in our ensemble of cold atoms, with the objective of performing a complete tomography of the retrieved state via homohyne detection, work that I started with Valentina Parigi, a post-doc, who continues now the experiment with a new PhD student, Pierre Vernaz-Gris, in cotutelle with the Australia's National University.

Thesis outline

The first part of this manuscript is devoted to the two main tools for the implementation of quantum memory protocols in an ensemble of cold atoms. The first chapter describes the quantum memory protocols investigated in this thesis, the EIT-based memory and the DLCZ scheme, both based on collective excitation, and the crucial parameters linked to them. In the second chapter, the ensemble of cold atoms that we developed is presented, with the experimental tools for an appropriate atomic preparation.

The second part is devoted to the experimental implementation of quantum memories in our system. It starts in chapter 3 with an investigation about the EIT phenomenon, through a test for discriminating between the EIT and the ATS models, proposed by [Anisimov et al., 2011]. In the chapter 4, we then report on the implementation of an EIT-based optical memory for photonic qubits encoded in orbital angular momentum (OAM) of light. First is implemented a reversible memory for Laguerre-Gaussian modes, and we demonstrate that the optical memory preserves the handedness of the helical structure at the single-photon level. Then, a full state tomography of OAM enoded qubits is performed, giving fidelities above the classical bound. This showed that our optical memory operates in the quantum regime. Finally, the chapter 5 presents the implementation of the DLCZ protocol in the ensemble of cold atoms. An homodyne detection setup allows us to realize the quantum tomography of the heralded single-photon state. Preliminary results are given.

Publications

These works have been published in the following journals.

- "Experimental investigation of the transition between Autler-Townes Splitting and electromagnetically-induced transparency models", L. Giner, L. Veissier, B. Sparkes, A. S. Sheremet, A. Nicolas, O. S. Mishina, M. Scherman, S. Burks, I. Shomroni, D. V. Kupriyanov, P. K. Lam, E. Giacobino, and J. Laurat, *Physical Review A* **87**, 013823 (2013).
- "A reversible optical memory for twisted photons", L. Veissier, A. Nicolas, L. Giner, D. Maxein, A.S. Sheremet, E. Giacobino and J. Laurat, *Optics Letters* **38** (5), 712-714 (2013). .
- "A quantum memory for orbital angular momentum photonic qubits", A. Nicolas, L. Veissier, L. Giner, D. Maxein, E. Giacobino and J. Laurat, *Nature Photonics* **8**, 234-238 (2014).

Part I

Theoretical and experimental keys for quantum memory implementations

Chapter 1

Collective excitation in a large ensemble of cold atoms

Contents

Developing coherent protocols that allow storage and manipulation of quantum states carried by light is crucial for quantum information science, including quantum networks and communications. Because of their long-lived coherences, atomic spin states are precisely good candidates for this purpose. As many protocols require the use of single photons, such quantum memory protocols have to work at the single-photon level, a not-so-easy to reach regime.

Intuitively the simplest approach for reversible transfer is to map single-photon states into single atoms. Thus, a single-atom coherently absorbs and emits later on-demand a single-photon. Strong interaction between single photons and atoms are required to achieve good storage and read-out efficiency, but the absorption of an individual atom is very small. An elegant solution to this problem,

the well-known cavity QED framework [Miller et al., 2005], consists in placing the atom into a high finesse resonator in order to enhance its effective cross section. The photon now travels many times in the cavity, and can interact with the atom with a larger probability. A lot of work has been done in this direction over the past few decades by different groups, leading to the recent textbook demonstration of polarization qubit storage in a single-atom quantum memory [Specht et al., 2011]. However it is still technically challenging to reach the very strong coupling regime and to control the motion of individual atoms at the same time.

On the other side, atomic ensembles containing a large number of atoms can interact strongly with light. The key feature relies on collective effects, which allow to achieve easily strong and controllable coupling between many-atom systems and photons. The use of optically thick atomic ensembles was thus motivated by the simplicity and the potential efficiency compared with single-atom settings. The last ten years have seen a tremendous activity in this direction, both theoretically and experimentally [Lukin, 2003, Lvovsky et al., 2009, Simon et al., 2010, Sangouard et al., 2011].

In atomic ensembles the coherent and reversible mapping of photonic quantum states can be achieved via the electromagnetically induced transparency (EIT) phenomenon. The atoms are driven by an auxiliary laser field that enables to control the photon group velocity, and in consequence to stop and trap them inside an atomic cloud [Fleischhauer and Lukin, 2002]. Another protocol, which was seminal for the study of protocols based on atomic ensembles and quantum repeater architectures, is the DLCZ scheme [Duan et al., 2001]. This is a measure-induced protocol. Based on Raman scattering this protocol allows for instance the generation of probabilistic but heralded entanglement between remote atomic ensembles [Chou et al., 2005, Laurat et al., 2007a]. This entanglement can be transferred from atoms to photonic modes on demand, so this scheme represents an elementary link of a quantum repeater. The building block of the DLCZ scheme can be also used as an heralded single photon source.

In this chapter we first motivate the choice of cold atoms as a medium for quantum memory implementation. Then we remind the principle of collective excitation, and in particular we focus on the two quantum memory protocols introduced above, which rely on collective enhancement, the dynamic EIT protocol and the DLCZ scheme. Finally critical parameters to achieve such quantum memory protocols in atomic ensembles are presented.

1.1 Why using cold atoms ?

The use of cold gases instead of warm vapors in order to build a quantum memory is motivated by several aspects, in particular the need to reach the single-photon level and the necessity of avoiding Doppler broadening. We discuss in the following these two different aspects.

1.1.1 Down to the single-photon level

Single-photon has become a basic resource in quantum information science, where a great variety of protocols involving single photons have been proposed. As stated before, the implementation of reliable quantum memories at the single-photon level is thus truly wanted but still experimentally challenging. In order to detect these photons single-photon counters, such as avalanche photodiode (APD), are very convenient because they are sensitive to the single-photon level, easy to use and now reaching reasonable efficiency, typically $> 50\%$ at the cesium wavelength, 852 nm, with low dark count rate. Nevertheless, strong laser pulses must illuminate the atomic ensemble to control the interaction, whether it be for the

dynamic EIT or the DLCZ protocol. Let us give a first indicating number. The bright coupling pulse contains a huge number of photons, e.g. 2.10^8 in a 0.5 µs pulse with a power of 100 µW at 852 nm. Rejection by at least 80 to 100 dB is thus required. To increase the difficulty, EIT or DLCZ quantum memory schemes were proposed in a configuration where the coupling beam co-propagating along with the interesting signal. It is therefore essential to efficiently separate the single photons from the coupling field, which mostly overlap in time, in order to collect single photons with good signal-to-noise ratio for characterization or further applications.

Going down to the single-photon level is not a trivial task in many practical implementations. The first experimental demonstrations of nonclassical correlations between photon pairs generated in atomic ensembles by the first step of the DLCZ protocol were indeed realized in collinear geometry [Kuzmich et al., 2003, Wal et al., 2003]. One of the main experimental challenges was to separate the photons from the classical pulses, and that is why classical fields were filtered in polarization and also in frequency, using optically pumped atomic cells. Values for the normalized correlation function $g_{1,2}$, which characterizes quantum correlations between the two photons, slightly above the classical limit of 2 were obtained [Kuzmich et al., 2003]. However, the authors were still strongly limited by the write and read field contamination in each detection path. The solution was then to use an off-axis configuration, namely to put an angle between the driving fields and the ones to detect for spatial filtering [André, 2005].

First experimental uses of an off-axis configuration were reported in the classical regime in 2004 by the authors of [Braje et al., 2004] and in the quantum regime in 2005 [Matsukevich et al., 2005]. In the latter the authors reached $g_{1,2} \approx 300$ with this additional spatial filtering, and high-quality heralded photons were thereafter generated and values of $g_{1,2}$ as large as 600 were obtained [Laurat et al., 2006]. Two similar experiments of EIT storage of a single photon generated by the aforementioned method give an illustration of the effect of this spatial filtering. One has been performed in warm atoms and with collinear configuration [Eisaman et al., 2005], while the other has used an ensemble of cold atoms and the off-axis configuration [Chanelière et al., 2005]. The off-axis configuration allowed to achieve 20 times better $g_{1,2}$ than the collinear one does at the single-photon creation step.

Although coherence times of few milliseconds have been demonstrated in warm atomic ensembles in the collinear configuration, using another protocol [**?**], working in off-axis configuration kills the effective coherence time in warm atomic ensembles because of motional dephasing. Indeed, whether it be EIT or DLCZ, both of these protocols lead to the formation of a spin-wave grating in the atomic ensemble with a spatial period that can be much smaller than the size of the whole sample. The interfringe depends on the difference $|\Delta\mathbf{k}|$ between the $\mathbf{k}$ vector of the two fields (either control and signal in EIT or write and field 1 in DLCZ), which form a small angle θ,

$$\Lambda = \frac{2\pi}{|\Delta\mathbf{k}|} \approx \frac{\lambda}{\sin\theta}\,. \tag{1.1}$$

Here the wavelength of both fields are supposed to be identical and equal to λ, a very good approximation in most experimental cases.

This grating is written during the writing process and has to remain until the reading process otherwise the information about the optical excitation is partially lost and the efficiency decreases. If atoms fly by a distance comparable to its spatial period within the storage time, the grating is destroyed. As a typical value, one can evaluate the average time for an atom to fly over an interfringe of the interference pattern because it limits the maximum achievable storage time. A realistic experimental example would be the following: a control and a signal fields at 852 nm propagate in an ensemble of cesium atoms with an angle of 2°. As a result the interference pattern period is 25 µm. So, it takes

only 170 ns for 330 K atoms to travel across Λ, while it takes 100 µs for 1 mK atoms and 300 µs for 100 µK atoms. In this configuration the dephasing time due to atomic motion will be more than 500 times longer in cold atomic ensembles than in warm ones.

Collisional effects also induce decoherence in warm vapors. The authors of [Manz et al., 2007] investigated the dephasing on collective state in the DLCZ scheme due to collision and concluded that buffer gas in particular configuration should help to achieve longer coherence time, in addition to beam with large diameters. This was confirmed by a study of the effect of the angle between coupling and signal beams in a rubidium vapor heated at 78°C, leading to the observation of 10 µs coherence time with an angle $\theta = 2^\circ$ [Jiang et al., 2009].

Another issue related to warm atomic ensembles is the required power for the coupling fields. First, if the laser needs to be off-resonance it must be set with a detuning comparable to the Doppler broadening, about some hundreds of MHz. To compensate this large detuning it is essential to operate at higher power of the coupling beams, and filtering becomes more difficult. In addition, enlarging the size beams in order to avoid decoherence effects contributes also to the increase of the power needed. That is why several hundreds of milliwatts in the coupling path may be sent in warm vapors and co-propagate with the single-photon level signal. Thus, filtering in this scheme is very difficult and requires especially frequency filters such as cascaded Fabry-Perot etalons. With high power pulsed lasers, a quantum memory operating at the single-photon level has been recently demonstrated in a warm atomic ensemble [Reim et al., 2011]. However, the memory time was limited to 1.5 µs, with a signal-to-noise ratio around one.

In summary, although very interesting works have been realized in warm vapors, cold gases appear as a better platform to achieve the single-photon regime and keep reasonable coherence time at the same time.

1.1.2 Avoiding Doppler broadening

Historically, the LKB quantum optics group studied the behavior of warm and cold atomic ensembles and first implemented EIT-based quantum memories in ensembles of warm atoms [Cviklinski et al., 2008, Ortalo et al., 2009]. In warm vapors, the Doppler broadening is the main component of inhomogeneous broadening. Each atom sees both control and signal fields with different frequencies depending on its velocity class. For a pure 3-level system in EIT, the resulting effect is a narrowing of the transparency window. However the presence of hyperfine structure in the excited level associated with the Doppler broadening, which is of the same order of magnitude as the separation in the excited state, destroyed almost totally the transparency effect. Studies have been done in that direction in our group and it has been demonstrated that depumping some velocity classes enables to enhance EIT in warm cesium atoms [Mishina et al., 2011, Scherman et al., 2012]. Cooling and trapping atoms in a magneto-optical trap strongly suppresses the Doppler broadening. This enables to see deep transparency window and consequently to implement EIT-based quantum memory with better performances in ensembles of cesium atoms.

Drawbacks of cold atoms Even though there are many advantages of using cold atomic ensemble, as seen before, to implement quantum memories it still remains drawbacks. Here are the main ones:

1. The vacuum chamber, the ion pump and all the other vacuum components are much bulkier than a simple ambient-temperature cell.
2. It requires at least two frequency-stabilized lasers just to cool and trap the atoms.

3. When based on magneto-optical trap, the trapping magnetic field must be switched off during the memory implementation (see chapter 2). Thus, the experiment runs in cycles, with a loading stage and an experiment stage, and this has two consequences. First the storage time is intrinsically limited by the cloud expansion. That is why a vertical configuration has been developed in [Bao et al., 2012], storage times of few milliseconds were reported. Secondly the repetition rate of the memory implementation is also limited. In fact, the time required to cool and trap the atoms usually represents the main part of the timing, specially for ultracold atoms experiments.

One way to avoid the latter drawbacks is to use dipole traps [Chuu et al., 2008, Zhao et al., 2009]. Thus, the atoms are always trapped, even during the memory implementation stage, and once the differential light shifts induced by the dipole traps across the entire lattice are compensated, long storage times can be obtained. Very recently, optical storage in such a medium during 16 s has been observed in a classical regime [Dudin et al., 2013].

In conclusion, despite of some drawbacks, cold atoms enable to realize quantum memories at the single-photon level, with both large signal-to-noise ratio and long coherence time. Moreover, Doppler broadening is limited, and this allows to increase the memory performances. In the following section, we introduce the memory protocols that we implement in an ensemble of cold atoms during this PhD work, the EIT-based memory, and the DLCZ building block. The common point between them is the generation of collective excitations, which we first discuss.

1.2 Collective excitation

Collective states are of major interest because they can lead to collective enhancement, enabling the retrieval of an excitation stored in a large atomic ensemble with an efficiency close to unity, in a well defined spatiotemporal mode. In order to achieve long storage time it is also important to operate with long-lived states, such as hyperfine sublevels of the ground state of alkali atoms.

In a large ensemble of N identical atoms optically pumped in a ground state $|g\rangle$, a collective excitation corresponds to the transfer of one atom among the N atoms to another ground state $|s\rangle$, but it is absolutely impossible to know which one is concerned (see fig. 1.1). The spin-flip is thus said delocalized over the atomic ensemble. This state is therefore a coherent superposition of all the possible terms with $N-1$ atoms in $|g\rangle$ and one atom in $|s\rangle$ and it can be written as the following spin symmetric state

$$\begin{aligned} |1\rangle &= \hat{s}^\dagger |0\rangle \\ &= \hat{s}^\dagger |g_1, g_2, ..., g_i, ..., g_N\rangle \\ &= \frac{1}{\sqrt{N}} \sum_{i=1}^{N} |g_1, g_2, ..., s_i, ..., g_N\rangle \ , \end{aligned} \tag{1.2}$$

where $\hat{s}^\dagger$ is the creation operator for one atomic excitation in $|s\rangle$. Note that in practice, the amplitudes of each term may vary, depending on the laser beam profiles or on the shape of the atomic ensemble.

Now we describe two memory protocols, the EIT-based memory and the DLCZ building block, which rely on such collective excitations.

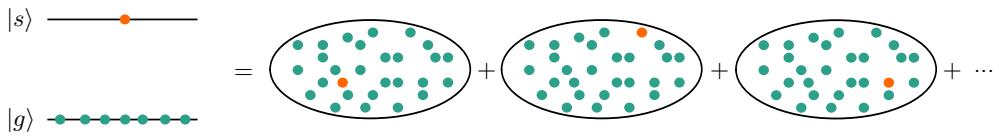

FIGURE 1.1 : Simple representation of a collective excitation. All the atoms are prepared in the ground state $|g\rangle$ and because of a unique excitation one atom among all is transferred to $|s\rangle$. Thus, the atomic ensemble is in a coherent superposition of all the possibilities.

1.2.1 The dynamic EIT protocol

Via the electromagnetically induced transparency phenomenon, an initially strongly absorptive sample can become transparent for a given signal by the mean of an additional control field [Harris, 1997]. This effect is accompanied by a reversible reduction of the signal group velocity, which enables to build an optical memory. We explain in the following how the control field opens a transparency window, and how a light pulse can be mapped into an ensemble of atoms by dynamically changing the control field intensity.

1.2.1.1 Electromagnetically-induced transparency

We consider an ensemble of N identical atoms with a Λ-type configuration as shown in figure 1.2: two ground states, $|g\rangle$ and $|s\rangle$, and one excited state. Initially all the atoms are prepared in $|g\rangle$. A control field drives the $|s\rangle \rightarrow |e\rangle$ transition with a Rabi frequency Ω while the signal field probes the $|g\rangle \rightarrow |e\rangle$ transition.

In the regime where Ω is much larger than the Rabi frequency of the signal field we first consider the two states $|s\rangle$ and $|e\rangle$ interacting with the control field which is represented here by a Fock state with n photons. In the basis $\{|s\rangle|n\rangle, |e\rangle|n-1\rangle\}$ the Hamiltonian associated with one atom is

$$H^n = \begin{pmatrix} 0 & \Omega \\ \Omega & 0 \end{pmatrix}, \tag{1.3}$$

assuming $\hbar = 1$ for simplicity, as in the rest of the manuscript. The dressed states $|s\rangle|n\rangle$ and $|e\rangle|n-1\rangle$ have the same energy that corresponds to a null coefficient on the diagonal of the Hamiltonian and they

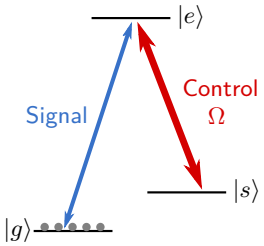

FIGURE 1.2 : Atomic Λ-configuration. Atoms are initially prepared in one of the ground state in such a way that in the absence of the control field, the signal is strongly absorbed.

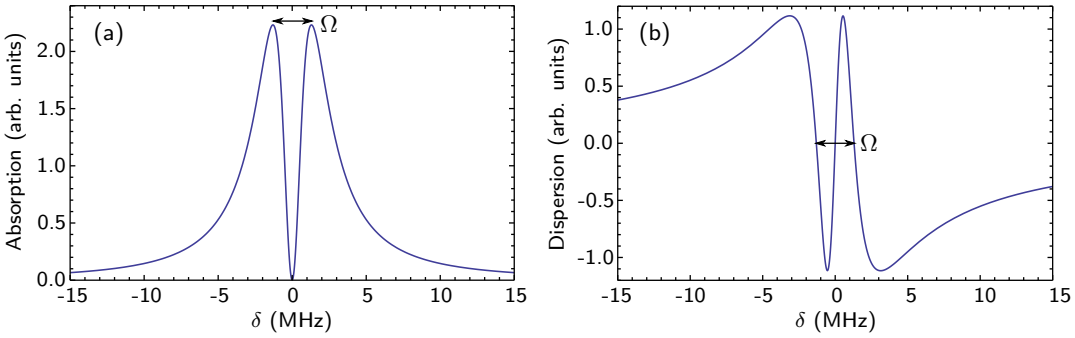

FIGURE 1.3 : EIT features displayed: signal field absorption and dispersion as a function of its detuning δ to resonance. The control field results in the appearance of a transparency window in the absorption profile and modify the dispersion with a steep slope close to resonance. The Rabi frequency Ω of the control is a crucial parameter.

are coupled to the control field related to the Rabi frequency Ω. The eigenstates of H^n,

$$\begin{aligned} |\psi_+^n\rangle &= \frac{1}{\sqrt{2}}\left(|s\rangle|n\rangle + |e\rangle|n-1\rangle\right) , \\ |\psi_-^n\rangle &= \frac{1}{\sqrt{2}}\left(|s\rangle|n\rangle - |e\rangle|n-1\rangle\right) , \end{aligned} \tag{1.4}$$

are associated with the eigenvalues $\pm\Omega$. The eigenstates of the system {atoms+field} correspond to superpositions of the dressed states $|s\rangle|n\rangle$ and $|e\rangle|n-1\rangle$. The energy gap between these two states is proportional to the Rabi frequency of the coupling field. For a large enough intensity of this coupling field a transparency window for the signal appears, with a width scaling with Ω, as shown in figure 1.3. In the same time, the dispersion of the medium becomes very large, that leads to drastically reduce the signal group velocity. In these conditions, "slow light" was observed experimentally in 1999, with an impressive reduction of the light speed down to 17 m/s in a Bose-Einstein condensate [Hau et al., 1999]. Nevertheless, the EIT phenomenon is still widely studied, e.g. in optomechanical systems [Safavi-Naeini et al., 2011].

1.2.1.2 Reversible mapping of a photonic excitation

Here we consider the two transitions $|g\rangle \rightarrow |e\rangle$ and $|s\rangle \rightarrow |e\rangle$, the control field as well as the signal field to store. The latter is assimilated to a single photon coupled to an atom with the coupling constant g and all the atoms are prepared in the state $|g\rangle$. The system can be described in the base $\{|\underline{g}\rangle|n-1\rangle|1\rangle, |\underline{e}\rangle|n-1\rangle|0\rangle, |\underline{s}\rangle|n\rangle|0\rangle\}$ with

$$\begin{aligned} |\underline{g}\rangle &= |g_1, g_2, ..., g_i, ..., g_N\rangle , \\ |\underline{e}\rangle &= \frac{1}{\sqrt{N}}\sum_{i=1}^{N}|g_1, g_2, ..., e_i, ..., g_N\rangle , \\ |\underline{s}\rangle &= \frac{1}{\sqrt{N}}\sum_{i=1}^{N}|g_1, g_2, ..., s_i, ..., g_N\rangle . \end{aligned} \tag{1.5}$$

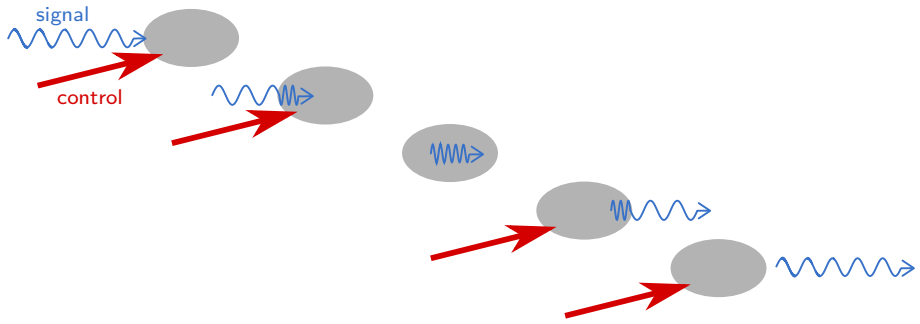

FIGURE 1.4 : Illustration of the dynamic EIT protocol. In the presence of a strong control field, the incoming pulse is spatially squeezed inside the medium due to the reduction in the group velocity. When the control laser is switched off, the compressed pulse remains trapped inside the atomic ensemble. Then, by switching on again the control laser the signal pulse is re-emitted ideally in the same spatiotemporal mode.

The states $|\underline{e}\rangle$ and $|\underline{s}\rangle$ are collective symmetric states, as the one presented above in equation 1.2. The Hamiltonian is therefore given by

$$H(t) = \begin{pmatrix} 0 & g\sqrt{N} & 0 \\ g\sqrt{N} & 0 & \Omega(t) \\ 0 & \Omega(t) & 0 \end{pmatrix}. \tag{1.6}$$

We can ignore in the following the control field photons $|n\rangle$, and only write the atomic and signal states. The two eigenstates of the Hamiltonian $H(t)$ are

$$\begin{aligned} |\psi(t)\rangle &= \frac{1}{\sqrt{g^2N + \Omega^2(t)}} \left(\Omega(t)\,|\underline{g}\rangle\,|1\rangle - g\sqrt{N}\,|\underline{s}\rangle\,|0\rangle\right), \\ |\phi(t)\rangle &= \frac{1}{\sqrt{2(g^2N + \Omega^2(t))}} \left(g\sqrt{N}\,|\underline{g}\rangle\,|1\rangle + \sqrt{g^2N + \Omega^2(t)}\,|\underline{e}\rangle\,|0\rangle + \Omega(t)\,|\underline{s}\rangle\,|0\rangle\right), \end{aligned}$$

associated respectively with the eigenvalues 0 and $\sqrt{g^2N + \Omega^2(t)}$. If $\Omega(t)$ varies slowly in time the adiabatic regime hypothesis can be applied. Thus, the dynamic of the system is given by the eigenstate of $H(t)$ which is connected to the initial condition. We consider the case where initially $\Omega \gg g\sqrt{N}$, corresponding to the first eigenstate, so the system is described by the so-called "dark-state" [Fleischhauer and Lukin, 2000]

$$|\psi(t)\rangle = \frac{\Omega(t)}{\sqrt{g^2N + \Omega^2(t)}}\,|\underline{g}\rangle\,|1\rangle - \frac{g\sqrt{N}}{\sqrt{g^2N + \Omega^2(t)}}\,|\underline{s}\rangle\,|0\rangle. \tag{1.7}$$

The transfer of the photon energy into the atomic ensemble can be made reversible by changing Ω in time, as illustrated in figure 1.4. At first, if $\Omega \gg g\sqrt{N}$, $|\psi\rangle = |\underline{g}\rangle\,|1\rangle$ so the photon propagates across the medium. Then, by switching off the control laser, $|\psi\rangle = |\underline{s}\rangle\,|0\rangle$ and the optical excitation is mapped into the collective spin state $|\underline{s}\rangle$. After a user-defined delay the control field is turned on again such as $\Omega \gg g\sqrt{N}$. The system is back in the state $|\psi\rangle = |\underline{g}\rangle\,|1\rangle$ and the photon is retrieved in a well-defined mode. Therefore, the reversible mapping of photonic quantum state into and out of an atomic ensemble is possible by dynamically varying the control power. The first demonstration of this reversible mapping was reported by the authors of [Liu et al., 2001]. Other aspects concerning spatial or temporal pulse shaping during the process are detailed in section 1.3.1.

Thus, we have seen how to take advantage of collective effects to coherently and reversibly map

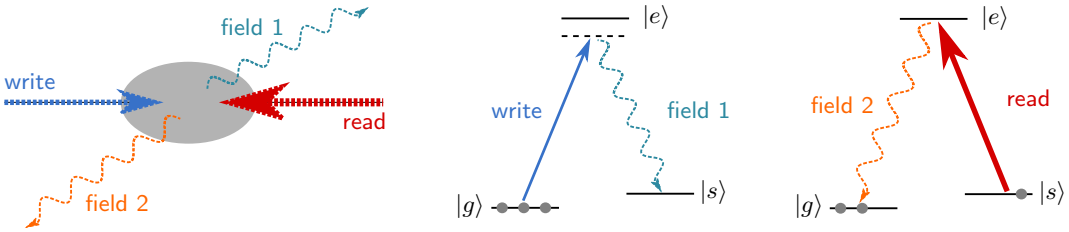

FIGURE 1.5 : DLCZ building block in an off-axis configuration, and the relevant atomic levels with the associated light fields involved in the writing and reading processes.

a photonic state into an atomic ensemble, via the dynamic EIT protocol. Still relying on collective effects, it is also possible to produce interesting quantum states of light, as photon pairs or heralded single-photon, by the implementation of the DLCZ protocol.

1.2.2 The DLCZ building block

Introduced by Duan, Lukin, Cirac and Zoller in 2001 [Duan et al., 2001], the seminal DLCZ protocol constitutes a scheme for quantum repeater implementation. The building block can be seen as the generation of photon pairs temporally separated by a user-defined delay and so is very interesting by itself for various purposes in quantum information science, and enables to work with atomic ensembles in the single-excitation regime.

As for the EIT setting, the DLCZ building block requires a large ensemble of N identical atoms with a Λ-type atomic configuration. As shown in figure 1.5, a weak write pulse detuned from the $|g\rangle \rightarrow |e\rangle$ transition induces spontaneous Raman scattering into a photonic mode called field 1 or Stokes photon, transferring one atom into the state $|s\rangle$. There is no preferred direction of emission for the field 1, the total emission probability corresponds to the sum of the emission probability for each photon, but we focus on one particular direction for both field 1 photon and atomic excitation. If the write pulse power is low enough so that two excitations are unlikely to occur, the system $\{\text{atoms} + \text{field } 1\}$ is described by the following state

$$|\psi\rangle = |0\rangle_a |0\rangle_1 + \sqrt{\chi}\,|1\rangle_a |1\rangle_1 + O(\chi)\,, \tag{1.8}$$

where $\chi = 4g^2NL/c\,(\Omega/\Delta)^2 t_w$ is the small Raman scattering probability, L the length of the medium, Ω the Rabi frequency, Δ the detuning, and t_w the duration of the write pulse [Lukin, 2003]. The index a denotes the atomic state while the index 1 is for the field 1 state. The collective state $|1\rangle_a$ is similar to the one presented above (equation 1.2), or in the EIT part (equation 1.5). It corresponds to a symmetric spin excitation in the atomic ensemble, with a phase term

$$|1\rangle_a = \frac{1}{\sqrt{N}} \sum_{i=1}^{N} e^{\mathrm{i}(\mathbf{k}_w - \mathbf{k}_1)\cdot \mathbf{r}_i} |g_1, g_2, ..., s_i, ..., g_N\rangle\,, \tag{1.9}$$

where $\mathbf{k}_w$ and $\mathbf{k}_1$ are the $\mathbf{k}$ vectors of the write field and the field 1 photon, and $\mathbf{r}_i$ is the position of the i$^{\text{th}}$ atom. Equation 1.8 indicates that the atomic spin-flip and the emission of the field 1 photon are strongly correlated. Practically, the field 1 is filtered in polarization, in frequency, and spatially in the case of an off-axis configuration. The frequency filtering is very important to guaranty the creation of a spin-flip. Consequently, in the very low excitation regime, the detection of a photon in the field 1 mode projects the ensemble into a non-classical state with a single excitation delocalized among the whole ensemble. The writing process is probabilistic, but heralded. It is an example of measured-induced protocol.

After a programmable delay a read pulse is sent on resonance with the $|s\rangle \rightarrow |e\rangle$ transition and enables to transfer the atomic collective excitation into a second photonic mode, the field 2 or anti-Stokes photon. Due to collective effect, this read out process can become very efficient, but some supplementary phases arise, leading to a phase matching condition. Indeed, the term corresponding to the emission of a field 2 photon is proportional to

$$\sum_{i=1}^{N} e^{\mathrm{i}(\mathbf{k}_w - \mathbf{k}_1)\cdot \mathbf{r}_i} e^{\mathrm{i}(\mathbf{k}_r - \mathbf{k}_2)\cdot \mathbf{r'}_i} |0\rangle_a |1\rangle_1 |1\rangle_2 \,, \tag{1.10}$$

where $\mathbf{k}_r$ and $\mathbf{k}_2$ are the $\mathbf{k}$ vector of the read field and the field 2 photon, and $\mathbf{r'}_i$ is the position of the i$^{\text{th}}$ atom at the read time. We immediately see that the condition for constructive interference depends on the atomic motion during the storage time.

- If atoms are moving, constructive interference arises only for $\mathbf{k}_1 = \mathbf{k}_w$ and $\mathbf{k}_2 = \mathbf{k}_r$, and we recognize what has been mentioned above in section 1.1.1, that the collinear geometry is strongly recommended with warm atomic ensembles.
- If there is no atomic motion, constructive interference occurs whenever the phase-matching condition

  $$\mathbf{k}_1 + \mathbf{k}_2 = \mathbf{k}_w + \mathbf{k}_r \tag{1.11}$$

  is fulfilled. In consequence the probability amplitude for the field 2 emission in the $\mathbf{k}_w + \mathbf{k}_r - \mathbf{k}_1$ direction is large.

For very large atomic ensembles the emission in the direction that satisfies the aforementioned conditions can completely dominate all the others and leads to a high efficiency collection of the field 2 photon thanks to many-atom interference effect, namely collective enhancement. In the ideal case the final state of the system {field 1 + field 2} is

$$|\phi\rangle = |0\rangle_1 |0\rangle_2 + \sqrt{\chi} |1\rangle_1 |1\rangle_2 + O(\chi)\,. \tag{1.12}$$

Photon numbers for fields 1 and 2 are correlated. In fact the two modes are entangled, as it is for two-mode squeezed states in parametric down conversion or four-wave mixing processes. This DLCZ building block based on Raman scattering is thus a source of photon pairs with a delay, and can also be used as a heralded single photon source [Chou et al., 2004, Laurat et al., 2006].

Entangling atomic ensembles The DLCZ scheme enables the generation of entanglement between two remote atomic ensembles [Chou et al., 2005, Laurat et al., 2007a]. In a synchronous manner two write pulses illuminate two atomic clouds, denoted left (L) and right (R) and separated by a long distance. The scattered photons in field 1 are collected and interfere in an indistinguishable manner on a 50/50 beam splitter, outputs of which are detected by two single-photon counters (see figure 1.6). The detection of one and only one field 1 photon heralds a unique spin excitation in one of the two ensembles, but knowing in which one is impossible from a fundamental point of view. The two atomic ensembles are thus projected in a maximally entangled state

$$|\Psi\rangle^{\pm}_{\mathrm{LR}} = \frac{1}{\sqrt{2}} \left(|1\rangle_{\mathrm{L}} |0\rangle_{\mathrm{R}} \pm |0\rangle_{\mathrm{L}} |1\rangle_{\mathrm{R}} \right) , \tag{1.13}$$

where the $\pm$ sign depends on the output where a photon is detected. Finally, the heralded entanglement between the two atomic ensembles can be transferred to photonic entanglement by applying two read pulses simultaneously. Thus, the two field 2 paths are entangled. More details about the entanglement swapping and about quantum repeaters in general can be found in [Sangouard et al., 2011, Laurat et al., 2007b].

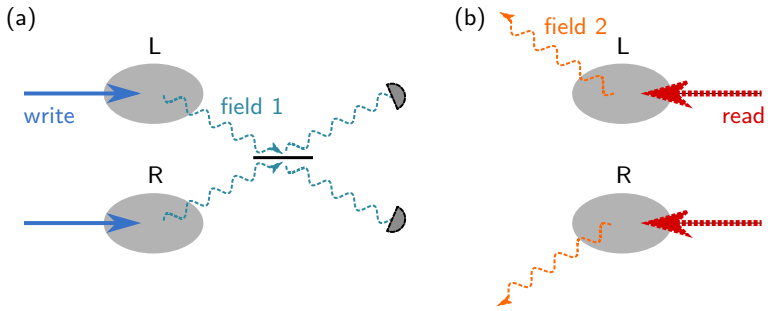

FIGURE 1.6 : Entanglement in the DLCZ scheme involving (a) the measured-induced creation of entanglement between two remote atomic ensembles via the indistinguishable detection of a single-photon on a detector, and (b) its subsequent mapping into single-photon entanglement.

1.3 Critical parameters

In the EIT-based storage or the DLCZ building block implementation, the retrieval efficiency must be in principle very close to unity thanks to the collective enhancement, on which these protocols are based. However, in practice, one of the most limiting factors is the achievable optical depth of the atomic ensemble. Moreover, some other processes must be considered, as they induce decoherence of the stored collective excitation. It can be dephasing due to atomic motion or to inhomogeneous broadening, caused for instance by residual magnetic fields. In this section, we first highlight the crucial role of the optical depth to achieve good efficiencies. Then, we list the different sources of decoherence in order to identify the main one in the case of cold atoms from a magneto-optical trap, as we implemented. Finally, we detail the consequences on the collective spin state described in the previous section.

1.3.1 Optical depth

1.3.1.1 Definition and general considerations

The optical depth, or optical thickness, measures the absorption of a medium. It represents the fraction of a light beam which is scattered or absorbed along its path. If I_0 is the initial light intensity and I the intensity after the medium, the optical depth d_0 is defined by the following relation

$$I = I_0 e^{-d_0} \,. \tag{1.14}$$

This dimensionless quantity results from three terms

$$d_0 = \sigma n L \,, \tag{1.15}$$

where σ is the effective cross section which is proportional to λ^2, n is the atomic density of the medium, and L is the length of the sample. Therefore the optical depth depends on the number of atoms interacting with the light on the beam path.

In order to recognize the signature of the optical depth in the protocols, we express the optical depth as a function of the factor $g^2 N$ [Gorshkov et al., 2007b]

$$d_0 = \frac{2\, g^2 N L}{c\, \gamma_{ge}} \,. \tag{1.16}$$

Here, g is the coupling constant between the electromagnetic field and one atom, N the number of atoms, and γ_{ge} the relaxation rate of the $|g\rangle \rightarrow |e\rangle$ coherence, equal to half of the linewidth Γ of the excited level.

Optically thick media are required to observe collective effects, which are not visible with individual systems. That is one of the common points between EIT-based storage and DLCZ building block. However, the need for high optical density in both quantum memory protocols can be discussed in slightly different ways, as we do in the following.

1.3.1.2 Optical depth in the DLCZ building block

In the DLCZ building block, the atomic ensemble is prepared in a collective state. When the read pulse is applied, the excited atom comes back to the initial state and emits a second photon in a well-defined spatiotemporal mode. However, in competition with this collective enhancement some spontaneous emission may occur.

The theoretical demonstration of collective enhancement has been treated in the case of an atomic ensemble surrounded by a low-finesse cavity (see supplementary information of [Duan et al., 2001]). The collective effect is here in competition with spontaneous emission. On one side, the coherent interaction scales with the effective interaction rate $\kappa' = 4\,g^2 N|\Omega|^2/(\Delta^2\kappa)$, with κ the cavity decay rate, Ω the Rabi frequency and Δ the detuning of the classical write field. On the other side, the dephasing rate of spontaneous photon scattering is given by $\gamma' = \Gamma\,\Omega^2/\Delta^2$. Thus, a signal-to-noise ratio can be defined as $R = \kappa'/\gamma'$. In the limit where the finesse of the cavity is equal to one, which corresponds to the free-space case, $\kappa = c/L$, with L the length of the atomic ensemble. The signal-to-noise ratio is thus given by

$$R = \frac{4\,g^2 N L}{c\,\Gamma} = d_0\,, \tag{1.17}$$

and scales directly with the optical depth. If d_0 is large, the signal-to-noise ratio will be enhanced without the need of a cavity. More refined model has been developed later [Duan et al., 2002], and influence of the optical depth on the DLCZ process efficiency has been demonstrated experimentally [Braje et al., 2004, Simon et al., 2007].

Therefore, the optical depth plays a crucial role in the observation of collective effects in the DLCZ protocol. We now see the case of EIT-based memory.

1.3.1.3 Optical depth in an EIT medium

When the pulse to store propagates through the medium under EIT condition its group velocity v_g is reduced in comparison with the speed of light in vacuum c,

$$v_g = \frac{c}{1 + g^2 N/|\Omega|^2}\,, \tag{1.18}$$

where Ω is the Rabi frequency of the control field. The pulse is spatially compressed by a factor c/v_g, that enables to contain the entire pulse inside the sample in the ideal case. There are two conditions for trapping a light pulse inside the medium without losses.

First, the bandwidth $1/\Delta t$ of the signal pulse should be smaller than the width $\Delta\nu$ of the transparency

window: $1/\Delta t < \Delta\nu$. The transmission of the medium close to resonance is given by [Lukin, 2003]

$$T(\delta) \approx e^{-\frac{\delta^2}{\Delta\nu^2}} \quad \text{with} \quad \Delta\nu = \sqrt{\frac{c}{\gamma_{ge} L}\frac{|\Omega|^4}{g^2 N}} = \frac{2\sqrt{2}}{\sqrt{d_0}}\frac{|\Omega|^2}{\Gamma}\,. \tag{1.19}$$

Second, the delay τ induced by the medium should be much larger than the duration Δt of the pulse, i.e. $\tau \gg \Delta t$, where the temporal delay induced by a medium of length L can be written as

$$\tau = \frac{L}{v_g} - \frac{L}{c} = \frac{L}{c}\frac{g^2 N}{|\Omega|^2} = \frac{d_0}{4}\frac{\Gamma}{|\Omega|^2}\,. \tag{1.20}$$

We emphasize here that the two requirements - a large bandwidth and a large delay - are antagonistic. Indeed, by increasing the Rabi frequency of the control field, $\Delta\nu$ increases but τ decreases. In other terms, when the control power is increased, the transparency window becomes wider and is able to contain a signal pulse with a large spectrum. But at the same time, the slope of the dispersion curve at resonance decreases, the delay gets therefore smaller, and the signal pulse can not be spatially contained inside the atomic cloud. Experimentally, a trade-off needs to be found in order to minimize the losses (see section 4.1.2). By combining the two conditions, we find that

$$\tau\,\Delta\nu \gg 1\,. \tag{1.21}$$

This "delay-bandwidth" product is in fact independent of Ω and can be also expressed as

$$\tau\,\Delta\nu = \sqrt{\frac{d_0}{2}}\,. \tag{1.22}$$

Therefore, the two conditions, on both the preservation of the pulse spectrum and the complete pulse compression inside the ensemble, are satisfied together for a very large optical depth.

The role of optical depth, both in the EIT or DLCZ configuration, is illustrated on figure 1.7. The left

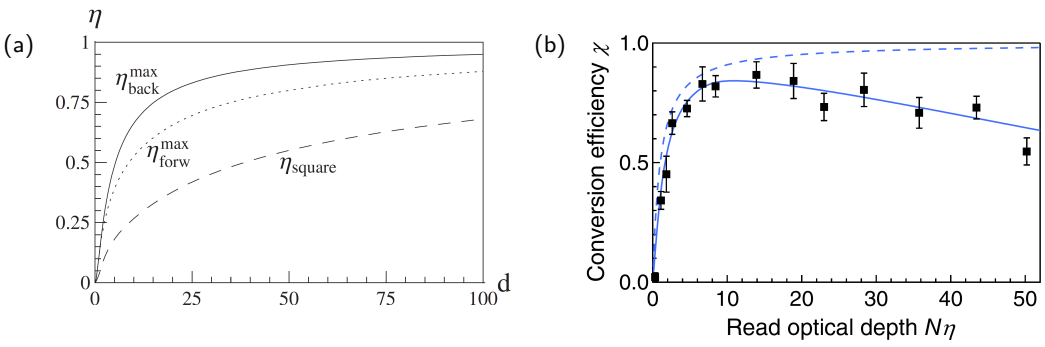

FIGURE 1.7 : Exemple of the importance of optical depth in the literature. (a) Theoretical efficiency η as a function of the optical depth d for an EIT memory based on a three-level atomic system, courtesy of [Gorshkov et al., 2007b]. The solid and dotted lines are the maximum efficiencies η^{max} for backward and forward retrieval, while the dashed line represents the efficiency of backward retrival without optimization of the signal or control pulse shape. (b) Conversion efficiency of the collective excitation into photonic state, in the DLCZ building block, as a function of the read optical depth, courtesy of [Simon et al., 2007]. The dashed line corresponds to prediction for a three-level system, while the experimental black dots are better fitted by a model taking into account dephasing due to additional hyperfine levels.

panel gives the theoretical storing and retrieving efficiency of a three-level EIT memory as a function of the optical depth, extracted from [Gorshkov et al., 2007a]. We clearly see that for large values of d_0 the efficiency tend to 1. The right panel depicts the case of the DLCZ building block, with the conversion efficiency of the collective spin state into a photonic excitation, namely the probability to emit a photon in field 2 given the detection of a photon in field 1, as a function of the optical depth, extracted from [Simon et al., 2007]. The same behavior is observed for small optical depth, until $d_0 \approx 10$. However, for higher values, the experimental efficiency decreases, because of dephasing due to additional hyperfine levels in this case. The drop of efficiency at very large optical depth has been then observed in several experimental cases [Phillips et al., 2008]. Generally, this phenomenon originates from defects of the atomic medium, such as residual absorption, which are enhanced when the optical depth increases, and at some point can dominate the collective effect. In consequence, atomic ensembles with large and tunable optical depth are wanted, but an investigation of the efficiency depending on the optical depth must be performed, in order to optimize the efficiency of the quantum memory.

1.3.2 Decoherence of collective excitation and timescales

The phenomenon of decoherence corresponds to the loss of the collective excitation after a given time. Thus, the information about the optical state which has been stored as a collective state is lost, and can not be mapped out of the atomic ensemble. Decoherence is always inevitable, but if its characteristic time is much longer than the storage time, the memory performances are not damaged.

As we have seen previously, the collective state is a coherent superposition of all the possible terms with $N-1$ atoms in the initial ground state $|g\rangle$, and one atom in the other ground state $|s\rangle$. Due to interaction with the environment, a phase term can appear in the expression of the collective spin state

$$|\psi(t)\rangle = \frac{1}{\sqrt{N}} \sum_{i=1}^{N} e^{i\phi_i(t)} |g_1, g_2, ..., s_i, ..., g_N\rangle \ , \tag{1.23}$$

where $\phi_i(t)$ depends on time, and can be different for each atom. It can indeed depend on the position or on the velocity of the atom i. Starting from this generic expression, we now discuss the different dephasing processes.

In an ensemble of cold atoms, different sources of decoherence can be identified: the atomic motion, the light shifts induced by strong trapping lasers, and the inhomogeneous broadening due to residual magnetic field.

1.3.2.1 Motional dephasing

We consider here the off-axis configuration, with a difference between the control and signal (or write and field 1) wavevectors $\Delta\mathbf{k} = \mathbf{k}_c - \mathbf{k}_s$ $(= \mathbf{k}_w - \mathbf{k}_1)$. Thus, if the atoms are not at rest, the dephasing term becomes

$$\phi_i(t) = \Delta\mathbf{k} \cdot (\mathbf{r}_i + \mathbf{v}_i(t)t) \ , \tag{1.24}$$

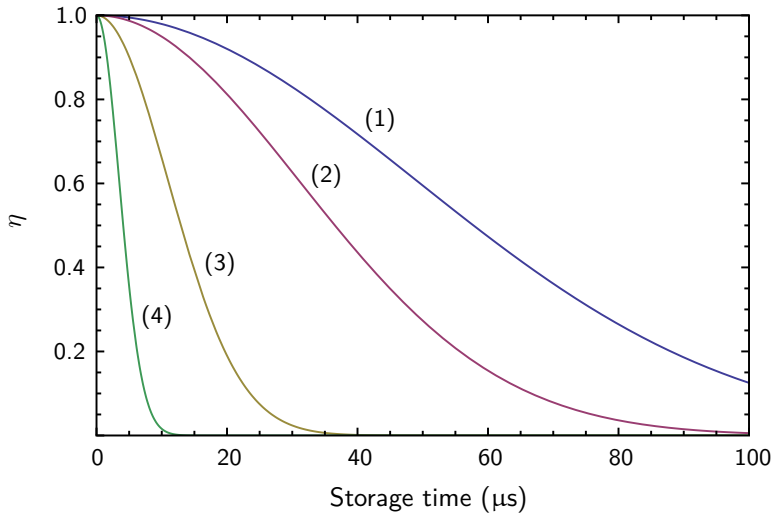

FIGURE 1.8 : Retrieval efficiency η of the collective excitation as a function of the storage time for (1) 50 μK, (2) 125 μK, (3) 1 mK, and (4) 10 mK. The angle is $\theta = 2°$, and we consider cesium atoms.

where $\mathbf{r}_i$ is the position of the atom i at $t = 0$, and $\mathbf{v}_i(t)$ its velocity. Thus, we can estimate the retrieval efficiency η as

$$\eta(t) \sim |\langle\psi(t=0)|\psi(t)\rangle|^2 = \left|\frac{1}{N}\sum_i^N e^{i\Delta\mathbf{k}\cdot\mathbf{v}_i(t)t}\right|^2 \quad (1.25)$$

$$= \left|\int f(\mathbf{v}) e^{i\Delta\mathbf{k}\cdot\mathbf{v}t} d\mathbf{v}\right|^2 \quad (1.26)$$

$$\sim e^{-t^2/\tau^2}\,. \quad (1.27)$$

The Maxwell-Boltzmann distribution $f(\mathbf{v}) \sim \exp[-mv^2/(2k_BT)]$ has a standard deviation $v_s = \sqrt{k_BT/m}$, with T the temperature of the atoms and m their mass. Morevover, as seen earlier, $|\Delta\mathbf{k}| = 2\pi\sin\theta/\lambda$. The decay constant is therefore given by

$$\tau = \frac{1}{|\Delta\mathbf{k}|\, v_s} = \frac{\lambda}{2\pi\sin\theta}\sqrt{\frac{m}{k_BT}}\,. \quad (1.28)$$

Figure 1.8 displays the evolution of $\eta(t)$ for some values of the temperature with an angle $\theta = 2°$. Thus, considering cesium atoms at a low temperature $T = 50$ μK, the decay constant τ is 70 μs (curve (1)). For atoms at the limit Doppler temperature $T_D = 125$ μK, we find $\tau = 44$ μs (curve (2)). For warmer atoms at $T = 1$ mK, which is our experimental case, the dephasing time decreases to 15 μs (curve (3)), while for a high temperature of 10 mK, it is about 5 μs (curve (4)). We clearly see that the temperature can be a limiting factor in our case, and in consequence the temperature of the cloud must be identified, in particular at large optical depth. Furthermore, to obtain storage time of the order of the millisecond, or even longer, sub-Doppler cooling or in-axis configuration must be considered.

1.3.2.2 Differential light shift

In the case of magneto-optical trap, no problem with light shift usually occurs. However, it is a common cause of decoherence in dipole trap, in particular used for optical lattices, where strong lasers are applied on the atoms, even during the memory implementation. The light shift corresponds to the

shift in frequency of an atomic state $|F, m_F\rangle$ due to a laser with strong intensity $|E(\mathbf{r})|^2$, and given by [Grimm et al., 2000]

$$U_{F,m_F} = |E(\mathbf{r})|^2 \sum_{F',m'_F} \frac{|\langle J, F, m_F|\mathbf{d}|J', F', m'_F\rangle|^2}{4\hbar\Delta_{F',m'_F}}, \tag{1.29}$$

where $\Delta_{F',m'_F} = \omega_L - \omega_{F,m_F\to F',m'_F}$ is the detuning of the laser to the atomic transition $|F, m_F\rangle \to |F', m'_F\rangle$. Thus, we can write the frequency difference between two sublevels, $|g, m_g\rangle$ and $|s, m_s\rangle$, of the ground states as:

$$\Delta\omega(\mathbf{r}) = \frac{U_{g,m_g} - U_{s,m_s}}{\hbar}. \tag{1.30}$$

Finally, the resulting dephasing is:

$$\phi_i(t) = \Delta\omega(\mathbf{r}_i)t. \tag{1.31}$$

Here we can see that if the laser intensity is not uniform on the atomic ensemble, $\omega(\mathbf{r}_i) \neq \omega(\mathbf{r}_j)$, the collective state is dephased after some time. Moreover, the phase shift depends on the m_F state of the atom in both ground states. Thus, dephasing will appear if several values of the total angular momentum projection, m_g and m_s, are involved in the memory process.

1.3.2.3 Residual magnetic field

In an ensemble of cold atoms obtained by magneto-optical trap, an important source of decoherence is the inhomogeneous broadening caused by the residual magnetic field. Indeed, the trapping magnetic field is usually switched off during the memory implementation, but residual magnetic field persists, due to the earth, or to the surrounding environment. Experimentally, additional coils enables to cancel this field to a finite value.

The presence of a magnetic field induces the splitting of a F hyperfine level into $2F+1$ sublevels by the Zeeman effect. The displacement of the m_F sublevel induced by a magnetic field B_z along the z direction is $Z_F m_F B$, where $Z_F = \mu_B g_F$ is the Zeeman coefficient, including the Bohr's magneton μ_B and the Landé factor g_F of the hyperfine level F. For alkali atoms, the Zeeman coefficient is actually opposite for the two ground states, so we note $Z = Z_g = -Z_s$.

As a consequence of the Zeeman effect, each single-atom excitation $|s_i\rangle$ from equation 1.23 should be developed as a superposition of spin flips which depend on the initial Zeeman state $|g, m_g\rangle$ and on the final one $|s, m_s\rangle$ [Felinto et al., 2005, Choi, 2011]. Thus,

$$|s_i(t)\rangle = \sum_{m_g,m_s} \alpha_{m_g,m_s} e^{i\phi_{m_g,m_s}(\mathbf{r}_i,t)} |s, m_s\rangle, \tag{1.32}$$

where α_{m_g,m_s} is a function of the population in the initial $|g, m_g\rangle$ state, and of the dipole matrix element for the $|g, m_g\rangle \to |s, m_s\rangle$ transition. Finally, the dephasing can be written as:

$$\phi_{m_g,m_s}(\mathbf{r}_i, t) = Z(m_g + m_s)B_z(\mathbf{r}_i)\, t. \tag{1.33}$$

Actually, the two sublevels m_g and m_s are not independent but are related via the polarization q of the different fields involved. We note $q = \pm 1$ for $\sigma^{\pm}$-polarization and $q = 0$ for π-polarization field. In the DLCZ protocol, the relation is $m_s = m_g + q_w - q_1$, where q_w and q_1 are the polarizations of respectively the write field and the field 1 . The case of the EIT protocol is exactly similar, the write being replaced by the control field and the field 1 by the signal field.

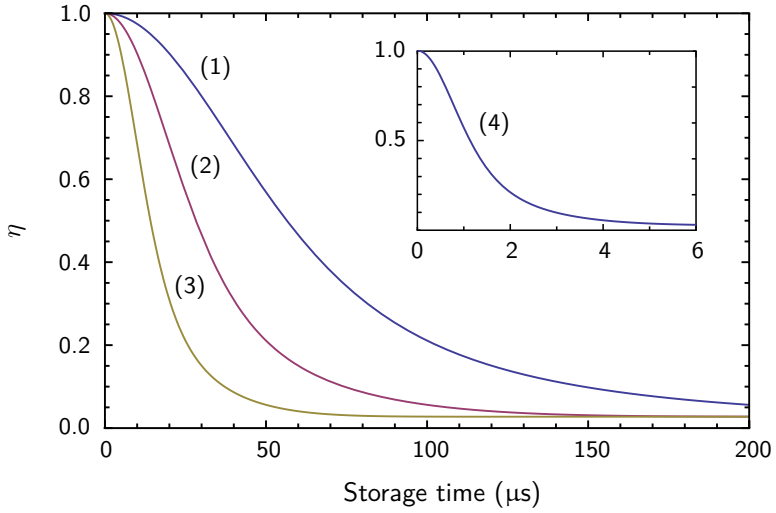

FIGURE 1.9 : Retrieval efficiency η of the collective excitation as a function of the storage time, for magnetic field gradient B_1 of (1) 50 mG/cm, (2) 100 mG/cm, (3) 200 mG/cm and (4) 2.5 G/cm. We consider $L = 2$ mm, and the dipole matrix elements corresponding to our experimental case.

To obtain typical values, we now assume the presence of a gradient of magnetic field along the z axis, $B_z(z) = B_1 z$, and a Gaussian atomic distribution, $n(z) = e^{-4z^2/L^2}$. The retrieval efficiency η is thus given by:

$$\eta(t) \sim |\langle\psi(t=0)|\psi(t)\rangle|^2 = \left|\frac{1}{N}\sum_{m_g,q_w,q_1}\alpha_{m_g,q_w,q_1}\int n(z)e^{iW(2m_g+q_w-q_1)B_1tz}dz\right|^2 \quad (1.34)$$

$$\sim \left|\sum_{m_g,q_w,q_1}\alpha_{m_g,q_w,q_1}e^{-t^2/\tau^2}\right|^2, \quad (1.35)$$

with $\tau = 2\sqrt{2}/(Z(2m_g + q_w - q_1)B_1L)$. The retrieval efficiency is calculated assuming that the ground state sublevels m_g are equally populated. We consider the dipole matrix elements of the cesium D_2 line, with $|g\rangle = |6^2S_{1/2}, F = 4\rangle$, $|s\rangle = |6^2S_{1/2}, F = 3\rangle$, $|e\rangle = |6^2P_{3/2}, F = 4\rangle$, which corresponds to our experimental case, and a length of the medium $L = 2$ mm. Figure 1.9 represents the calculated efficiency as a function of the storage time, for different values of the magnetic field. First, for a residual magnetic field of 2.5 G/cm, which is of the order of the residual magnetic field without compensation, the dephasing time is about 1 μs (curve (4) in inset). In order to increase the coherence time, the magnetic field can be canceled (see section 2.2), down to 10 mG approximately. Curves (1), (2), and (3) display the retrieval efficiency for residual gradient of magnetic field, after compensation, of respectively 50, 100 and 200 mG/cm. Under these assumptions, long storage times, up to 90 μs for 50 mG/cm, may be achievable thanks to the compensation of the magnetic field. However, we only consider here a gradient of magnetic field, whereas higher order components can be involved, and the atomic distribution is assumed quadratic, whereas it may be in practice flat in the center of the atomic cloud.

We have just seen that the characteristic time of the dephasing due to magnetic field can be increased to around 90 μs. However, the dephasing time constant due to motional dephasing for atoms at the Doppler limit temperature (125 μK) is 44 μs. In consequence, after compensation of the residual magnetic field, the main factor of decoherence may be in our case the atomic motion, as we are operating in an off-axis configuration.

Optical pumping Another method to avoid the inhomogeneous broadening due to residual magnetic field is to pump the atoms in a state insensitive to magnetic field, namely $m_g = 0$, and to involve only the $m_s = 0$ sublevel during the memory protocol. Therefore, the efficiency is in principle equal to unity whatever the storage is, and in practice it is limited by other factors, as the atomic motion. This method can also be useful in EIT protocol to avoid the possible residual absorption by the extreme sublevels $m_F = \pm(2F + 1)$.

Conclusion

What we have seen:

- Ensembles of cold atoms are very good candidates to implement quantum memory protocols at the single-photon level, a critical tool for quantum information science.
- One can take advantage of the many-atom interaction, which leads to collective enhancement. The dynamic EIT protocol and the DLCZ building block rely on collective effects and require a large number of atoms, namely high optical depth.
- In order to obtain long coherence time, dephasing effect must be avoided: motional dephasing and residual inhomogeneous broadening are the main contributions.

In consequence:

- We want to operate on an ensemble of cold atoms with high optical depth and in an off-axis configuration.
- The magnetic field has to be canceled down to the mG level in order to avoid any inhomogeneous broadening, and the angle of the off-axis configuration has to be small ($< 2°$).

Chapter 2

Tools for the atomic ensemble preparation

Contents

In the first chapter, we discussed how to implement a quantum memory in a large ensemble of cold atoms. The optical depth and the control of dephasing processes, due in particular to residual magnetic field, are critical parameters. Thus, in the past few years, we have developed a magneto-optical trap (MOT) for cesium atoms. Technical tools are described in this chapter for the preparation of the atomic ensemble. A special focus is given on the determination of the optical depth, the cancellation of magnetic fields and the preparation of atoms in a magnetic field-insensitive state.

N.B.: In the following, we describe processes that involve the atomic levels of the cesium D_2 line. The ground states $\left|6^2S_{1/2}, F = 3\right\rangle$ and $\left|6^2S_{1/2}, F = 4\right\rangle$ are denoted respectively $|F = 3\rangle$ and $|F = 4\rangle$, while the excited states $\left|6^2P_{3/2}, F = i\right\rangle$ are designated by $|F' = i\rangle$. Further details about cesium properties can be found in [Steck, 1998].

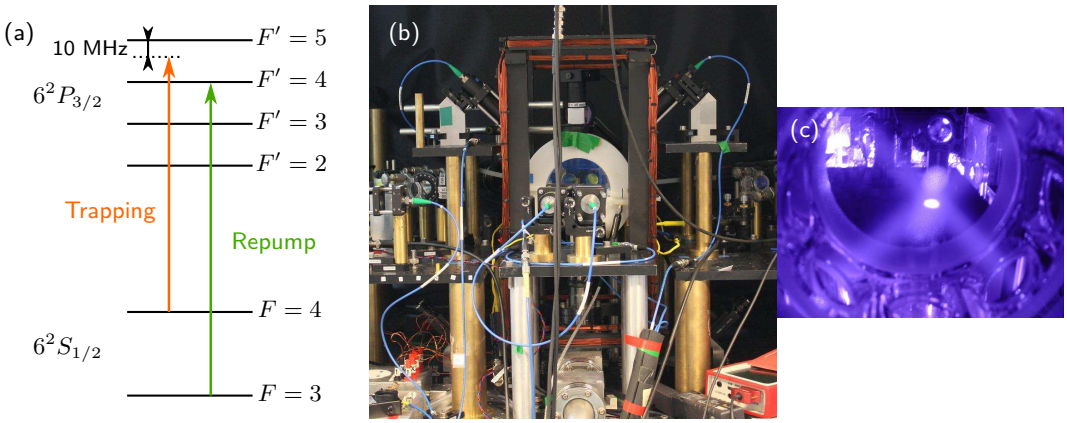

FIGURE 2.1 : Magneto-optical trap (MOT). (a) Cesium D_2 line with required lasers. The trapping field is 10 MHz-detuned from the $|F = 4\rangle \rightarrow |F' = 5\rangle$ transition, and the repump laser is on resonance with the $|F = 3\rangle \rightarrow |F' = 4\rangle$ transition. (b) Picture of the MOT setup with the three MOT collimators (the fourth one is for optical pumping), the glass chamber, and the trapping coils in white material. The square coils are for magnetic field compensation. (c) Picture of the atomic cloud trapped in the magneto-optical trap.

2.1 Large cloud of cold cesium atoms

2.1.1 Magneto-optical trap

A magneto-optical trap (MOT) is based on two steps: laser cooling thanks to the Doppler effect and then magneto-optical trapping based on the Zeeman effect. Atoms can be cooled by this technique down to the Doppler temperature which is for cesium atoms $T_D = 125$ µK, but the temperature of our dense atomic cloud is estimated around 1 mK (see section 3.4.2). The trapping laser drives the $|F = 4\rangle \rightarrow |F' = 5\rangle$ cycling transition of the D_2 line with a 10 MHz detuning and the repump laser couples the other ground state $|F = 3\rangle$ to the excited state $|F' = 4\rangle$ (figure 2.1(a)). Figure 2.1(b) shows a picture of our MOT setup which is made up of:

- 6 counter-propagative circularly-polarized one inch diameter beams, which are realized in practice by 3 pairs of collimators and reflecting mirrors,
- a pair of coils in the anti-Helmholtz configuration to obtain a quadrupole magnetic field with a gradient of around 20 G/cm in the coils axis direction,
- a glass chamber which limits the eddy currents, facilitates the switching of the trapping magnetic field, and gives many optical accesses with anti-reflection coated on both sides to limit optical losses (Precision Glassblowing),
- the vacuum apparatus, including the ion pump (Starcell Vacion Plus 40 L/s), which produces a vacuum below 10^{-9} Torr,
- cesium sources provided by dispensers placed just below the glass chamber, in the glass metal transition.

The trapping and repump beams come from very stable interference-filter external-cavity diode lasers, which have been developed in a collaboration through the IFRAF consortium [Baillard et al., 2006, Scherman, 2012]. They generate 3 × 25 mW by the help of a master oscillator power amplifier (Toptica, BoosTA) for the trapping beams, and 2 × 2.5 mW for the repump beams. These diodes are located on a distant table, and the light is transferred to the MOT table by polarization-maintaining optical fibers

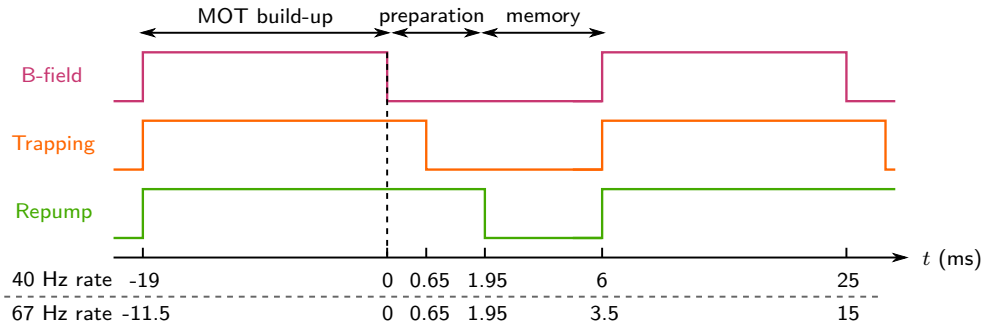

FIGURE 2.2 : Experimental cycling timing in three steps: the MOT loading, then the preparation of the atomic ensemble and finally the memory implementation. Duration of each stage depends on the repetition rate, which is either 40 Hz or 67 Hz.

(OZ Optics, PMJ-3S3S-850-5/125-3-5-1). More details about the MOT is given in [Giner, 2013]. This set up enable us to observe a cloud of cold atoms with a diameter around 2 mm, as in figure 2.1(c).

2.1.2 Timing

The trapping magnetic field must be off during the memory implementation, otherwise the coherence time is very short. Thus, the experiment runs in cycle with a repetition rate of 40 Hz. Each cycle consists in a MOT build-up step of 19 ms, followed by a preparation step of 2 ms, which is an intermediate step where the fields are successively switched off (figure 2.2). It also can be used to prepare the atoms in one specific state by optical pumping. Finally a memory step lasts 4 ms, where many cycles of storage and retrieval are realized. In a second experiment, we use an improved rate of 67 Hz, also depicted in figure 2.2. In order to accelerate the measurements, which needs a good statistic and so a large number of repetitions of the experiment, we reduce the cycle duration from 25 ms to 15 ms, without loss of the optical depth.

About FPGA and Labview programming The key feature of field-programmable gate array (FPGA) is its extremely precise clock, as opposed to computers. FPGA has thus become an element of prime importance in cold atom experiments and provides all the trigger signals to pulse light beams but also magnetic fields and various electronic devices. Dealing with FPGA and Labview environment involves manipulating two VIs (virtual instrument), the `Host.vi` and the `FPGA.vi`. The `Host.vi` runs on the computer, communicates with the FPGA but also manages the acquisition cards and analyses the data in our experiment. The `FPGA.vi` runs on the FPGA and generates the trigger signals for each element of the experiment. Both programs in our experiment were initially developed by Sidney Burks who gives a very clear overview of the concepts involved in FPGA programming in his thesis [Burks, 2010]. During my PhD, I first adapted the part dedicated to the realization of absorption spectra, which are used for the cancellation of the residual magnetic field or for the study of electromagnetically induced transparency (appendix B). Furthermore, I developed another part dedicated to the acquisition and the analysis of the single-photon detector outputs for the memory implementation (appendix C).

The trapping coil current is dynamically controlled by an electronic circuit developed in the LKB [Giner, 2013]. It enables to switch off the current with a characteristic time of about 100 µs. In our experiment, the switching off of the magnetic field defined the time $t = 0$, and is the reference for

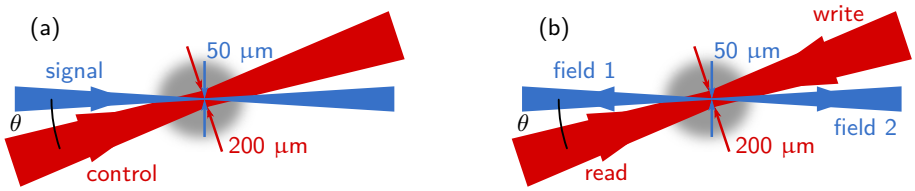

FIGURE 2.3 : Off-axis configuration for (a) EIT-based memory, involving two fields, or (b) DLCZ building block implementation, involving four fields. The angle θ is around 2°.

the other signals. All the trigger signals are generated and controlled by a field-programmable gate array (FPGA) via Labview (see boxed paragraph). The light beams are pulse-shaped by acousto-optic modulators. The trapping lasers remain on for 650 µs in order to prevent the atoms to escape from the cloud, while the repump laser is switched off few µs before the memory starts.

Thus, we now dispose of a cloud of cold atoms from a pulsed MOT. Several optical paths must be built in the atomic ensemble in order to realize a quantum memory.

2.1.3 Optical paths for memory implementation

During the memory step, EIT-based memory or DLCZ building block will be implemented. These protocols require the interaction between electromagnetic fields and the atomic ensemble. Different optical paths crossing the atomic ensemble have therefore been set up for each protocol, but many similarities exist, as we will see now.

Whatever the protocol, the best way to operate at the single-photon level is in an off-axis configuration (see section 1.1.1). Figure 2.3 shows the off-axis configuration for both protocols. The blue path, where the signal or the field 1 and 2 propagates, is focused into the atomic ensemble thanks to $f' = 500$ mm achromatic doublets, and has a waist of 50 µm. The red path, where the control or the write and read lasers propagate, is focused into the atomic ensemble by $f' = 800$ mm lenses, and has a waist of 200 µm, which allows to cover all the interaction region defined by the crossing of the blue path in the atomic ensemble, in spite of the angle θ (see figure 2.4(a)). The choice of the θ value, typically 2 or 3°, results from a trade-off. On one side, we want of course to optimize the retrieval efficiency, which decreases with the angle θ, principally because of dephasing due to the atomic motion. On the other side, the extinction of the coupling beams (control or write and read) on the signal path should be high enough to enable a good signal to noise-ratio for the detection of the signal, or field 1 and 2.

Control extinction The polarizations are orthogonal between the two paths, either linear or circular. Glan cubes are placed in the coupling path, before and after the atomic ensemble, in order to enable a first polarization filtering. Losses on the signal path induced by the Glan cube are about 10 %. The filtering of the coupling beam is also realized spatially thanks to the angle θ. For the memory experiment, the signal fields are coupled into single-mode fibers, and measured via single-photon counters. We characterize the extinction of the coupling beam as the ratio of the number of photons, converted into a power, detected on the single-photon counters, over the power of the coupling beam that is sent into the atomic ensemble. In our case, an extinction ratio of at least -100 dB is required to obtain a good signal-to-noise ratio. We make predictions for the value of extinction ratio we can obtain with an angle θ. The control intensity is averaged over the equivalent of the signal beam area (4 w_0). Figure 2.4(b) shows the transverse distance between the two modes, 15 cm away from the atomic cloud, where the extinction ratio is ideally extremely high (-1400 dB). However, in practice, several factors reduce

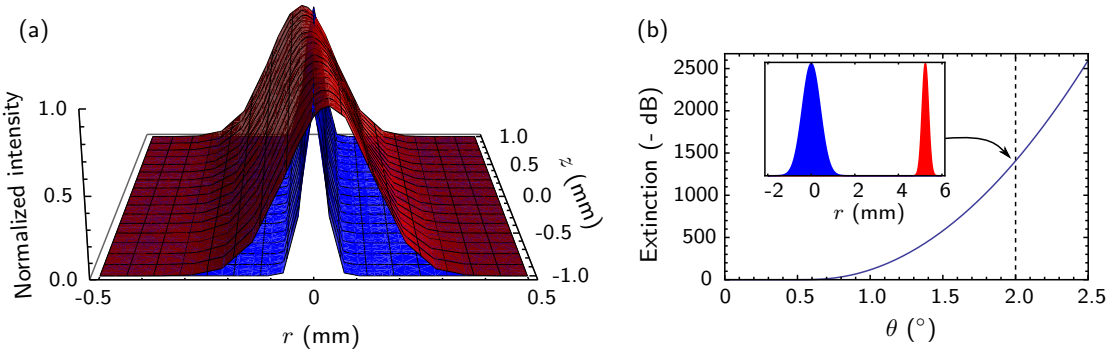

FIGURE 2.4 : Overlap between the two paths. (a) The normalized intensity is represented as a function of the transverse length r and the longitudinal length z within the atomic ensemble for an angle $\theta = 2^\circ$ between the two paths. The blue curve corresponds to the signal (field 1 and 2) path, while the red curve is for the control (write and read) path. (b) Predictions for the extinction of the coupling beam 15 cm away from the MOT, as a function of the angle θ. The dashed line represents our experimental case ($\theta = 2^\circ$), for which the transverse profiles of the two beams are displayed in inset. In practice, the extinction ratio drastically decreases because of imperfections of the spatial mode and scattering.

drastically this spatial extinction. It can be imperfections of the spatial mode of the coupling beam or scattering induced by our glass chamber and by the optics after the chamber. Experimentally, we realized a total extinction ratio of typically -110 dB, but which can reach -115 dB.

The pair of pulses sent into the atomic ensemble, control/signal or write/read, is generated by a Ti:Sapphire laser (Spectra Physics, Matisse) and an extended cavity laser diode, locked together in phase and in frequency at the hyperfine frequency $\omega_{hf} \simeq 9.2$ GHz (see section 1.2 for interaction schemes). The phase lock between the two lasers is described in appendix A.

Optimizing the overlap The control beam being only four times larger than the signal beam, its position must be precisely adjusted. This is realized by operating a transparency measurement with the signal field on resonance. More specifically, in the EIT configuration, a signal pulse is sent through the atomic ensemble. Thanks to the presence of a strong control field, the signal pulse is transmitted, partially in our case because of residual absorption. By reducing the control power, and so the Rabi frequency of the control, the transparency decreases, and becomes very sensitive to the control beam position. Then, by varying the control beam position in the atomic medium, we can find precisely the best overlap between the signal field, the atomic ensemble, and the control field. This optimization has be to done before every memory operation, and can be used also before running the experiment in the DLCZ configuration.

2.1.4 Measuring the optical depth

The optical depth is an essential parameter for collective effects. Indeed, large values of optical depth are required to observe efficient quantum memories based on collective enhancement, even though some effects may lead to decrease the efficiency for very high optical depth. We now explain how we determine the optical depth of our atomic ensemble.

From the definition given in section 1.3.1, the optical depth of an atomic ensemble is given by $d_0 = -\ln(I/I_0)$, with I_0 and I the probe intensities measured respectively before and after the atomic

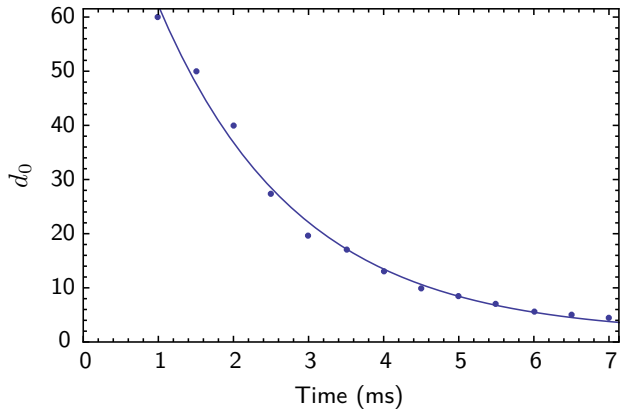

FIGURE 2.5 : Optical depth of the atomic cloud on the $|F = 4\rangle \rightarrow |F' = 5\rangle$ transition as a function of time. The trapping magnetic field is switched off at $t = 0$. The experimental points are fitted by a decreasing exponential with a decay constant of 1.9 ms.

ensemble. In practice it is even simpler to measure the intensity of the probe beam after the chamber without and with the MOT. Because we want to access to the optical depth seen by the signal, or fields 1 and 2, depending on the chosen memory protocol, the probe beam propagates in the atomic ensemble in the same path, with a waist $w_0 = 50$ µm.

To measure correctly d_0 the probe beam intensity I_0 must be very low compared to the saturation intensity, $I_{sat} = 2.7$ mW/cm^2. The corresponding power is approximately 200 nW, so we choose a very low power, around 10 nW, to avoid any pumping effect. Due to the noise level of the photodiode, the probe beam is seen on resonance as "completely absorbed" by the atomic ensemble. In consequence, the probe is set off-resonance with a detuning $\Delta = -$ 10 MHz from the $|F = 4\rangle \rightarrow |F' = 5\rangle$ transition. Thus, the cross section σ is modified from the on-resonance case (cross section σ_0) by a factor

$$\frac{\sigma_0}{\sigma} = 1 + 4\left(\frac{\Delta}{\Gamma}\right)^2 + \frac{I_0}{I_{sat}}\,, \tag{2.1}$$

where the I_0/I_{sat} term can be neglected. In our case we thus have $\sigma_0/\sigma \simeq 15.7$. Finally, by measuring I_0 and I of the probe beam detuned by $\Delta = -$ 10 MHz and propagating on the signal path with an intensity smaller than the saturation intensity, we calculate the optical depth at resonance by the following expression

$$d_0 = -\frac{\sigma_0}{\sigma}\ln\left(\frac{I}{I_0}\right) = -\left[1 + 4\left(\frac{\Delta}{\Gamma}\right)^2\right]\ln\left(\frac{I}{I_0}\right)\,. \tag{2.2}$$

Experimentally, 100 µs-long probe pulses are sent into the atomic ensemble. Figure 2.5 shows the evolution of the optical depth in time. At $t = 2$ms, which is a good compromise with the magnetic field cancellation (section 2.2) to start the memory sequence, the maximum of optical depth observed in our atomic ensemble is larger than 40, but the optical depth can be set at lower values. The optimization is done by changing the MOT beams alignment, in particular by moving the reflecting mirrors instead of the collimators, which is a less diverging method. The optical depth decreases as function of the time exponentially with a decay constant of approximately 2 ms. Thus, the memory implementation usually ends at 3 ms.

It is important to point out that we measure the optical depth for the $|F = 4\rangle \rightarrow |F' = 5\rangle$ transition. During the EIT-based memory implementation, the signal field is on the $|F = 4\rangle \rightarrow |F' = 4\rangle$ transition, so the effective optical depth for this field has to be corrected by the ratio between the two relative

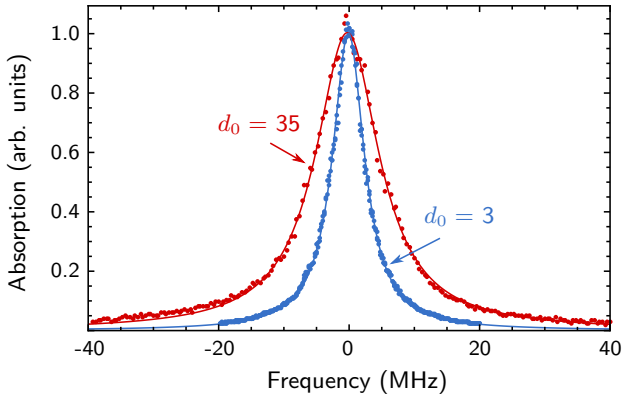

FIGURE 2.6 : Absorption profiles for two different values of the optical depth, fitted by a Lorentzian distribution with a width γ. The blue curve corresponds to an optical depth of 3, and its fitting gives $\gamma = 5.9$ MHz. The red curve corresponds to an optical depth of 35, and its fitting gives $\gamma = 11.8$ MHz. The linewidth of the excited state is $\Gamma = 5.2$ MHz.

hyperfine transition strength factors $S_{44}/S_{45} \simeq 0.48$.

Broadening due to high optical depth In order to test the appearance of broadening in our system at high optical depth, we acquire absorption profiles for different optical depth values. For cesium atoms, the linewidth of the excited level $6^2P_{3/2}$ is given by a Lorentzian function with a full width at half maximum $\Gamma = 2\pi\times$ 5.2 MHz. Figure 2.6 shows absorption profiles for a small and a large optical depth. The experimental data are fitted by a Lorentzian distribution. For a low optical depth, $d_0 = 3$, the fit gives $\gamma = 5.9$ MHz, which is slightly larger than Γ. At a large optical depth of $d_0 = 35$, the Lorentzian width has here doubled, and is now $\gamma = 11.8$ MHz. This means that homogeneous broadening occurs in our system, specially at high optical depth. A typical cause of homogeneous broadening is atomic collisions. This is still under investigation in our setup.

2.2 Cancellation of the magnetic field

Canceling the spurious magnetic field that remains when the trapping field is off is crucial in order to increase the coherence time (see section 1.3.2.3). The residual magnetic field, of the order of 0.5 G, is due to the earth magnetic field or to the environment around the chamber, the optical table for instance. Microwave spectroscopy, as described in this section, is a sensitive method to probe the magnetic field at the center of the vacuum chamber. Thus, by varying the current of the compensation coils, it is possible to control and cancel the magnetic field, and finally reach residual values about 7 mG.

2.2.1 Probing the residual magnetic field by microwave spectroscopy

Principle The principle of the microwave spectroscopy method is similar to the one described in [Ringot et al., 2001]. The main difference is that the authors used off-resonance lasers to induce stimulated Raman transitions, while in our case we operate with microwave field. A microwave pump pulse at a frequency ω around the hyperfine frequency $\omega_{hf} \simeq 9.2$ GHz drives the atoms from the initial $|F = 4\rangle$ state to $|F = 3\rangle$, depending on the detuning $\delta = \omega - \omega_{hf}$ of the microwave pump, which is scanned (see fig. 2.7). Indeed, if the microwave frequency corresponds to a transition between two

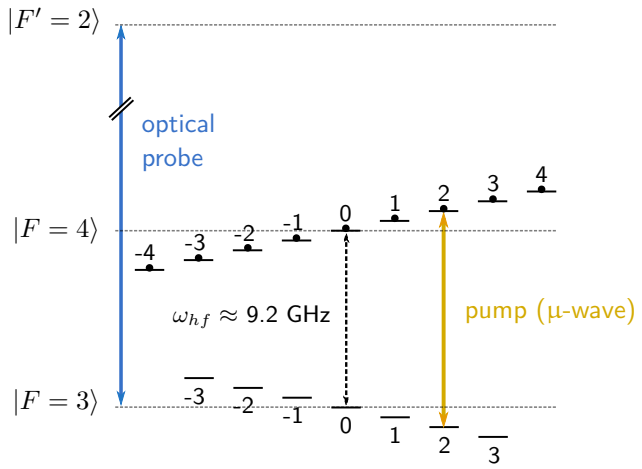

FIGURE 2.7 : Principle of the microwave spectroscopy method. In presence of magnetic field the two ground states are split in opposite direction. A microwave pump pulse drives atoms initially in $F = 4$ to $F = 3$, and an optical probe pulse then probes the $|F = 3\rangle$ state.

Zeeman sublevels $|F = 4, m_F\rangle$ and $|F = 3, m_F\rangle$, atoms are driven to $|F = 3\rangle$, otherwise the atoms stay in $|F = 4\rangle$. Then, an optical pulse in resonance with the $|F = 3\rangle \rightarrow |F' = 2\rangle$ transition probes the presence of atoms in $|F = 3\rangle$ for each value of δ.

Experimental implementation The timing of the microwave spectroscopy is given on figure 2.8. The duration of the microwave pulse is optimized so as to drive the largest number of atoms in $|F = 3\rangle$, namely to make half a Rabi oscillation. With our basic antenna and the synthesizer level set at the maximum, 27 dBm, it takes 200 μs to produce a π-pulse. Then, the 15 μs-long and linearly polarized probe pulse is sent into the atomic ensemble by the signal path and its intensity I is recorded. After the first probe pulse, a repump pulse is sent to transfer all the atoms back into $|F = 4\rangle$, and a second probe pulse is applied. This additional step enables to measure the initial intensity I_0 of the probe beam independently of fluctuations of laser power or polarization. All the steps occur once in a MOT cycle and provide a measurement for one microwave pump detuning δ. Then, the microwave frequency is scanned by steps and its value changes at the end of each MOT cycle, or after few cycles if we want to average each point over few measurements. Finally, the reconstructed spectrum corresponds to the probe pulse absorption $A = -\ln(I_0/I)$ as a function of the microwave detuning δ. Thus, we need several MOT cycles to record a whole spectrum. Details about the frequency scan and about the acquistion and the analysis of the probe pulse are given in appendix B.

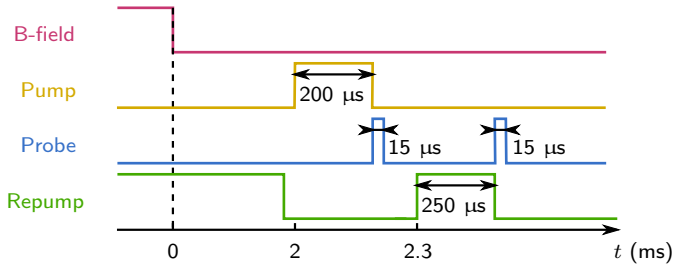

FIGURE 2.8 : Timing of the microwave spectroscopy sequence. After a 200 μs-long microwave pump pulse, a 15 μs-long probe pulse measures the atomic ensemble absorption. An additional probe pulse is sent after a repump stage in order to get a reference for the probe intensity.

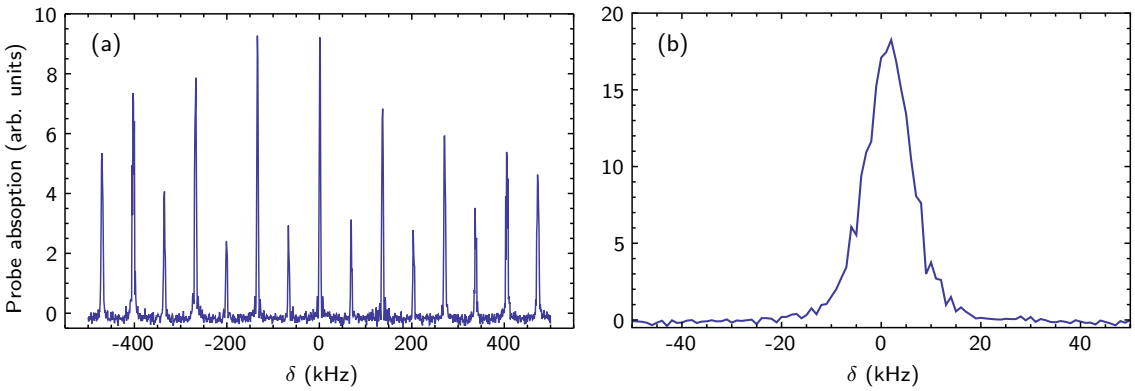

FIGURE 2.9 : Microwave spectroscopy measurement. The absorption of the probe pulse is represented as a function of the microwave pump detuning δ (a) when applying a DC magnetic field to split the different levels, or (b) after optimization of the compensation coil currents in order to cancel the spurious magnetic field. Typical widths around 20 kHz are routinely obtained.

Results Figure 2.9(a) shows a spectrum in the presence of magnetic field with 15 peaks: 7 peaks, the higher ones, come from π-transitions, while the 8 remaining ones are from σ-transitions. The predominance of π or σ transitions depends on the relative orientation between the external magnetic field $\mathbf{B}$ and the microwave field. The distance between two adjacent peaks is given by ZB, so the width of the whole spectrum is $14ZB$, with Z the Zeeman coefficient (section 1.3.2.3).

2.2.2 Magnetic field compensation

In order to compensate the residual magnetic field three pairs of small coils are available around the chamber (see figure 2.1). The current of each coil can be set independently. Thus, DC magnetic fields and gradients are modified in order to minimize the width of the spectrum. A typical spectrum after cancellation of magnetic field is displayed on figure 2.9(b). The width has been reduced down to less than 20 kHz, a value which corresponds to a residual magnetic field of 4 mG. In practice, fluctuations of the residual magnetic field in time prevent to preserve a good compensation. By averaging over few minutes, the width of the averaged spectrum is around 35 kHz. Effective residual magnetic field can therefore be estimated around 7 mG. Under the hypothesis considered in chapter 1 (section 1.3.2.3), the corresponding decay time is longer than 100 µs.

Let us note that the cancellation is realized at $t = 2$ ms after the trapping field is switched off. In fact, a trade-off between the optical depth and the magnetic field cancellation must be found. Indeed, operating as soon as possible after the MOT extinction enables to have the highest optical depth, but the magnetic field should be well canceled for a duration equivalent to the duration of the memory experiment, which lasts about 1 ms. In our experimental case too many magnetic field fluctuations remain until $t = 2$ ms, and in consequence a good cancellation over 1 ms can be obtained only if starting at $t = 2$ ms.

2.3 Optical pumping in $m_F = 0$

Optical pumping, or also called spin polarization, aims to prepare all the atoms into a unique Zeeman sublevel, in our case $|F = 4, m_F = 0\rangle$ because of its insensitivity to magnetic field, which may result in

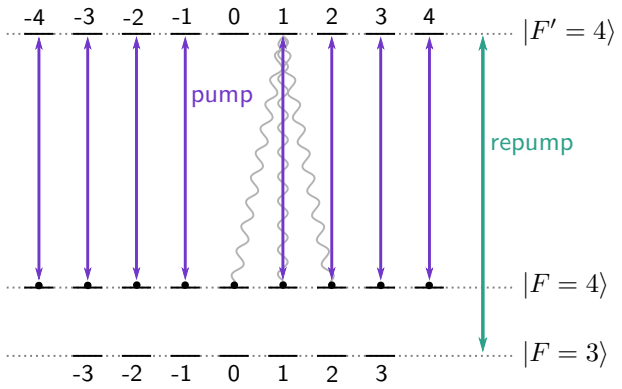

FIGURE 2.10 : Principle of optical pumping into $m_F = 0$. A π-polarized pump field is applied in order to transfer all the atoms into $|F = 4, m_F = 0\rangle$, which is a dark-state due to the nullity of the $|F, m_F = 0\rangle \rightarrow |F' = F, m'_F = 0\rangle$ coefficient. If atoms fall in $|F = 3\rangle$ the repump field bring them back into the pumping cycle. The number of levels is however an issue as many cycles are required, leading to a heating of the atoms.

longer coherence times. In addition, an atomic ensemble with all the atoms in a single Zeeman sublevel represents a system which is closer to a theoretical 3-level system. Then, residual absorption by atoms on the maximally stretched Zeeman states, which is an issue during the implementation of the EIT-based protocol with certain configurations of polarization, can be reduced.

2.3.1 Principle

The optical pumping in $m_F = 0$ is based on the fact that for cesium atoms the Clebsh-Gordan coefficient of the $|F, m_F = 0\rangle \rightarrow |F' = F, m'_F = 0\rangle$ transition vanishes. Thus, by applying a π-polarized pump on the $|F = 4\rangle \rightarrow |F' = 4\rangle$ transition, the $|F = 4, m_F = 0\rangle$ state becomes a dark-state (figure 2.10). Starting with atoms distributed over all the Zeeman sublevels, excitation by the pump laser leads to spontaneous decay into any sublevels of the two ground states. A repump laser coupling the $|F = 3\rangle$ and $|F' = 4\rangle$ states is thus required to bring back into the pumping cycle the atoms which fall in $|F = 3\rangle$. Then, as soon as atoms are trapped in the dark-state they do not experience anymore spontaneous emission due to fluorescence cycles and remain in this state. Consequently atoms accumulate in $|F = 4, m_F = 0\rangle$.

2.3.2 Experimental implementation

One problem with cesium atoms is the relatively large number of Zeeman sublevels, 9 in the $|F = 4\rangle$ state, so optical pumping can be achieved only after a large number of cycles. Consequently a number of atoms are potentially pushed away from the MOT before being pumped into the magnetic field-insensible state $|F = 4, m_F = 0\rangle$. To mitigate this problem, two pump beams counter-propagate through the atomic ensemble. This method is much more efficient than just retro-reflecting the pump laser, specially because the optical depth in our system is high. In this way we can set the pump laser on resonance with an intensity of 0.12 mW/cm^2 in each side without losing too much atoms. The optical depth decreases from 30 to approximately 20. In addition, a π-polarized repump leads to decrease the mean number of cycles that an atom needs to reach the central Zeeman level, in comparison with a non- or circularly-polarized repump [Tremblay and Jacques, 1990]. That is because for a circularly-polarized light, Clebsh-Gordan coefficients of the transitions that guide the atoms on the extreme Zeeman sublevels

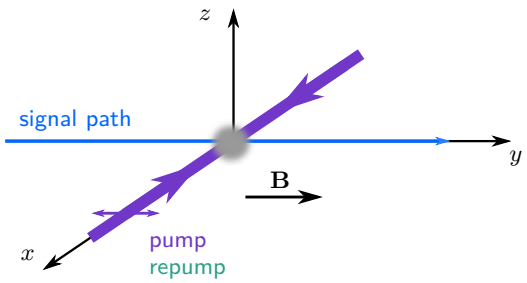

FIGURE 2.11 : Setup for optical pumping. The directive magnetic field $\mathbf{B}$ defining the quantization axis is applied along the y-axis signal path. The π-polarized pump and repump beams are sent from the front and back side of the chamber, i.e. along the x-axis.

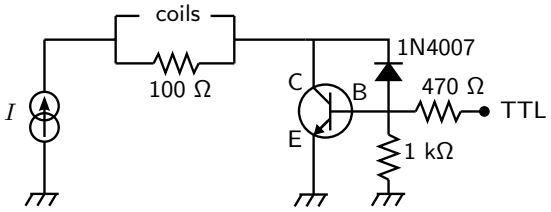

FIGURE 2.12 : Electronic circuit for the dynamic control of current in the coils that generate the additional magnetic field for optical pumping.

are stronger than the ones of transitions which bring the atoms to the center.

In order to properly define the quantization axis a magnetic field is applied during the pumping process and generates a Zeeman splitting of few hundreds of kHz. As shown in figure 2.11, the linear polarization of the pump and repump beams have to be set parallel to this quantization axis, which is aligned with the signal path. Thus, the pump and repump fields are sent along the x-axis by similar collimators as the MOT beam ones (one inch beam). Because the additional magnetic field must be switched off during the memory sequence, an additional pair of small coils, with a radius of 3.5 cm and made up of 40 turns, have been added close to the vacuum chamber, so they are separated by 10 cm. A simple circuit (figure 2.12) enables to cut the small coil current according to a trigger signal from the FPGA. The circuit is optimized to minimize the fall time of the current down to 100 µs at the expense of the rise time which is equal to 500 µs.

Figure 2.13 presents the timing of a typical optical pumping sequence. First of all the trigger signal for the directive magnetic field is switched on in advance at $t = 1$ ms to take into account the 500 µs rise time of the small coils current. Then at $t = 1.2$ ms, the MOT repump is turned off in order to

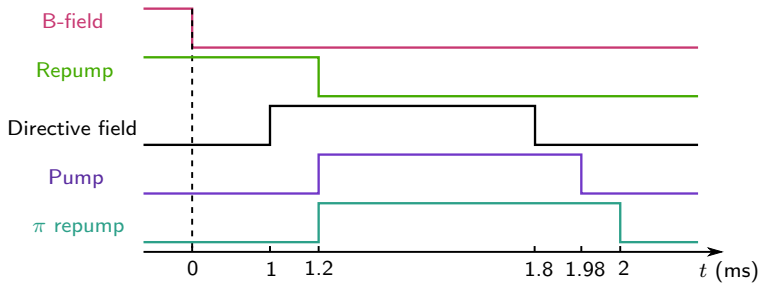

FIGURE 2.13 : Timing of the optical pumping sequence. Pump and repump beams are applied during 800 µs before the memory sequence, while a directive magnetic field defines the quantization axis. For clarity, the scale of the time axis in not respected.

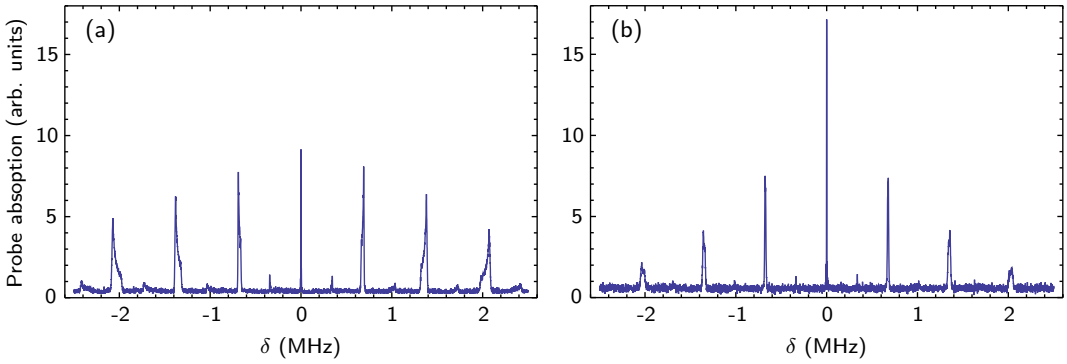

FIGURE 2.14 : Microwave spectroscopy measurements (a) without optical pumping and (b) with optical pumping to $m_F = 0$. The pump power is 2 $\times$ 2.5 mW while the power of the π-polarized repump is 2 $\times$ 0.5 mW. The optical depth of the atomic ensemble is 35 before the process.

enable the pumping process that operates with the pump and π repump lasers on. The pump pulse duration is 780 µs and the π repump pulse is switched off 19 µs after the pump pulse to bring back all the atoms into the $|F = 4\rangle$ state. The directive field trigger signal falls 200 µs before $t = 2$ ms to prevent any residual magnetic fields during the memory sequence, which starts at $t = 2$ ms.

2.3.3 Results and discussion

After the optical pumping process, we operate a spectroscopy sequence with the directive magnetic field on in order to measure the pumping effect. Figure 2.14 shows the effect of the optical pumping. The central peak corresponding to the population in the $m_F = 0$ sublevel doubles in height while the extreme peaks associated with the $m_F = \pm 3$ level decrease by a factor larger than two. Let us precise that the population in one Zeeman sublevel is proportional to the height of the corresponding peak, but coefficients are different for each sublevel because of the different dipole matrix elements. In addition, if in the spectroscopy sequence the microwave pump induced both σ- and π- transitions, 1, 2 or 3 resonances should be taken into account in order to deduce the population in one Zeeman state, thanks to the Clebsh-Gordan coefficients corresponding to the associated transitions. For this reason we only compare before and after the optical pumping process.

The achieved optical pumping is clearly not very efficient in our experiment, despite our estimations. We tried different pump detunings, durations and powers and we clearly see a saturation phenomenon before obtaining a very good spin polarization. Indeed, many atoms are lost, certainly pushed from the atomic cloud, without reaching the central Zeeman sublevel. One possible explanation is the temperature of the atomic ensemble, which may be too high before the pumping process. For instance, in [Chabé et al., 2007] the authors succeed in pumping 75 % of the atoms into the $m_F = 0$ sublevel with an atomic cloud at 3 µK, while our atomic ensemble is warmer than this by at least a factor 1000. Therefore the optical pumping as it is now does not help to win on the memory efficiency or on the coherence time. However the setup is in place and ready to use for further tries with colder atoms, as planned in the very near future.

Conclusion

What we have seen:

- We dispose of an atomic ensemble consisting in cesium atoms trapped in a pulsed magneto-optical trap in a glass chamber with a relatively large optical depth of 40 on the $|F = 4\rangle \rightarrow |F' = 5\rangle$ transition.
- The microwave spectroscopy enables us to cancel the residual magnetic field down to 7 mG which corresponds to a dephasing time of several tens of microseconds.
- Optical pumping into the magnetic field-insensitive state $m_F = 0$ has been set up. However, the observed results, although showing clearly a pumping effect, are not satisfying, as certainly limited by the temperature of the atomic cloud.

In consequence:

- The system is well prepared in order to observe collective effects and to implement quantum memory protocols, based either on EIT or the DLCZ paradigm.
- Further cooling the atoms is a crucial step for the very near future, and should enable to optically pump the atoms more efficiently and additionally to increase the coherence time by drastically decreasing the motional dephasing.

Part II

Experimental implementations of quantum memory protocols

Chapter 3

Experimental investigation of the transition between the Autler-Townes splitting and the electromagnetically induced transparency models

Contents

The work described in this chapter was motivated by the implementation of EIT-based memories and constituted a first experiment performed in our system. It aims at first studying EIT features in our implementation.

Coherent effects have been widely studied in the past two decades, leading to the modification of optical properties of atomic media [Fleischhauer et al., 2005]. These coherent effects can be for instance coherent population trapping [Alzetta et al., 1976, Arimondo, 1996], or electromagnetically induced

transparency [Harris et al., 1990, Boller et al., 1991, Marangos, 1998]. Enabling strong reduction of the signal group velocity, [Hau et al., 1999], EIT is particularly important for the implementation of quantum memories [Lvovsky et al., 2009]. More recently, coherent driving effects has been investigated in various systems, such as quantum dots [Xu et al., 2008], superconducting artificial atoms [Kelly et al., 2010] or nanoscale optomechanics [Safavi-Naeini et al., 2011].

In a Λ-type atomic configuration, two very different processes can explain the transparency of an initially absorbing medium for a probe field in the presence of a control field. The first one is a quantum Fano interference between two paths in a three-level system [Fano, 1961], occuring at low control intensity, and giving rise to EIT [Harris, 1997]. The second process is the appearance of two dressed-states in the excited level due to intense control field, corresponding to the Autler-Townes splitting (ATS) [Autler and Townes, 1955, Cohen-Tannoudji and Reynaud, 1977, Cohen-Tannoudji et al., 1992]. Discerning whether a transparency feature in an absorption profile is the signature of EIT or ATS is crucial and is a long-standing issue [Anisimov and Kocharovskaya, 2008, Abi-Salloum, 2010, Li et al., 2012]. Indeed, only EIT allows applications of coherent processes, essential for optically controlled light slowing, or optical storage, as mentioned before.

In this context, a recent theoretical study by Anisimov, Dowling and Sanders [Anisimov et al., 2011] introduced a method to discriminate between these two phenomena. Our work consists in verifying the reliability of the proposed criterion. In a well-controlled ensemble of cold atoms, where inhomogeneous broadening, in particular due to magnetic field environment, is avoided, we first perform a detailed study of absorption profiles of a weak signal field, in the presence of a control field. This study demonstrates in a quantitative way the transition for the ATS to EIT models when the control field power is decreased. This transition also reveals a strong sensitivity to the medium properties, such as the multilevel structure or the residual inhomogeneous broadening. This work has been published in Physical Review A 87, 013823, *Experimental investigation of the transition between Autler-Townes splitting and electromagnetically-induced-transparency models*, in collaboration with the group of P.-K. Lam at the Australia's National University.

3.1 From the EIT to the ATS models

3.1.1 Atomic susceptibility for a three-level system

Let us consider a three-level system in a Λ-configuration (see fig. 3.1), with two ground states $|g\rangle$ and $|s\rangle$ and an excited state $|e\rangle$. All the atoms are initially prepared in $|g\rangle$. An on-resonance control field drives the transition $|s\rangle \rightarrow |e\rangle$ with a Rabi frequency Ω, while the signal field probes the transition $|g\rangle \rightarrow |e\rangle$ with a detuning δ. The natural linewidth is $\Gamma = 2\pi\times$ 5.2 MHz while the dephasing rate between the two ground states is denoted γ_{gs}. The value of this dephasing rate is given by experimental factors, such as the linewidth of the lasers or the phase lock precision between the two lasers. By denoting d_0 the optical depth of the medium and $\gamma_{ge} = \Gamma/2$ the optical relaxation rate of the $|g\rangle \rightarrow |e\rangle$ coherence, the atomic susceptibility $\chi(\delta)$ in the first order in the probe electric field is therefore given by [Anisimov and Kocharovskaya, 2008]

$$\chi(\delta) = -d_0\gamma_{ge}\frac{\delta + i\gamma_{gs}}{\delta^2 - |\Omega|^2/4 - \gamma_{ge}\gamma_{gs} + i\delta(\gamma_{ge} + \gamma_{gs})}\,. \tag{3.1}$$

The atomic susceptibility corresponds to the atomic response, and gives access to the absorption by evaluating its imaginary part, and to the dispersion by evaluating its real part Figure 3.2 displays the

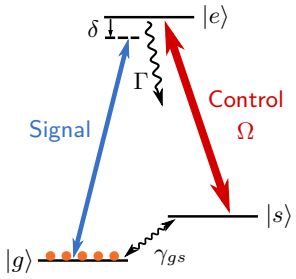

FIGURE 3.1 : Atomic three-level system in a Λ-type configuration. The natural linewidth of the excited state $|e\rangle$ is Γ while the dephasing rate between the two ground states $|g\rangle$ and $|s\rangle$ is denoted γ_{gs}.

absorption and dispersion spectrum for two different values of the Rabi frequency of the control. For small Rabi frequency, the absorption profile exhibits a narrow transparency window (panel (a)), induced by the quantum Fano interference effect. In addition, around $\delta = 0$ the dispersion spectrum (panel (b)) presents a very steep slope, which enables to strongly reduce the group velocity of the signal field. When the Rabi frequency of the control field is large compared with the natural linewidth, two dressed states in the excited level appear (panel (c)), while the dispersion profile shows a quite flat slope close to the origin (panel (d)), and so no drastic reduction of the signal velocity can be observed in this regime.

The susceptibility given in equation 3.1 has two complex poles and depending on the range of Ω, different simplifications can be done [Anisimov and Kocharovskaya, 2008]. Simplified or approximated expression for the absorption as a function of the signal detuning δ can be found in each regime [Anisimov et al., 2011]. These expressions are called, for small Ω, the EIT model, and for large Ω, the ATS model, as detailed in the following.

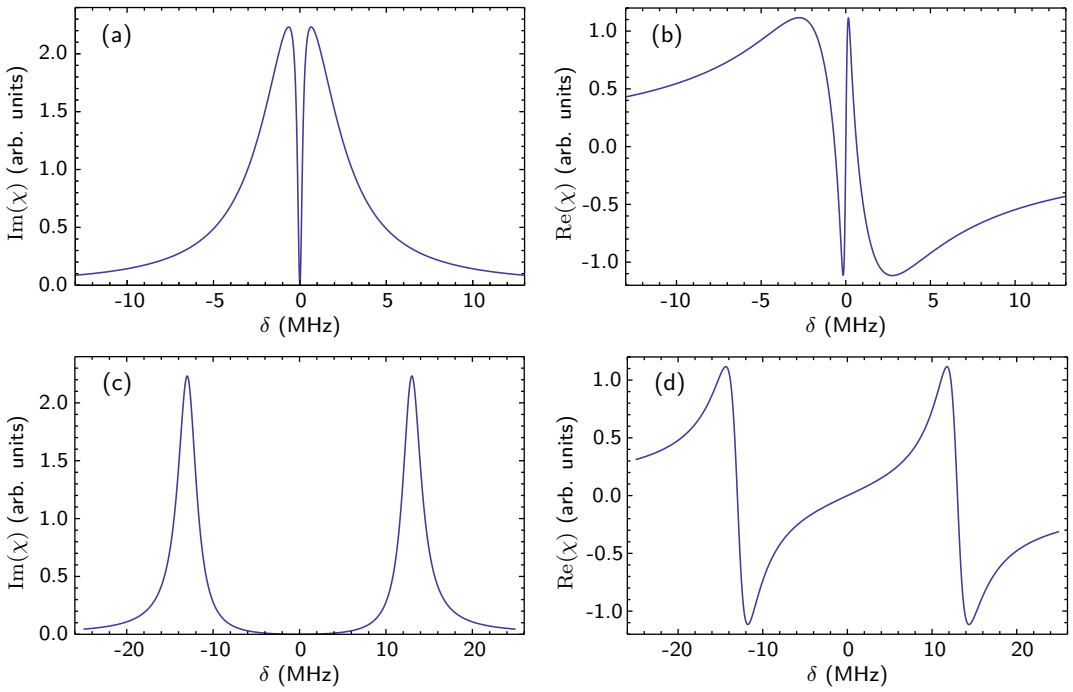

FIGURE 3.2 : Atomic susceptibility features in a three-level atomic system. Imaginary and real parts of the atomic susceptibility (a)-(b) for a small Rabi frequency of the control, $\Omega = 0.25\,\Gamma$, and (c)-(d) for a large Rabi frequency, $\Omega = 5\,\Gamma$. The dephasing rate is $\gamma_{gs} = 10^{-4}\,\Gamma$.

3.1.2 Electromagnetically induced transparency model

For small Rabi frequency of the control, $\Omega \leq \Omega_{EIT} = \gamma_{ge} - \gamma_{gs}$, the two poles of $\chi(\delta)$ become imaginary, and the absorption can be expressed as the difference of two Lorentzian functions,

$$A_{\mathrm{EIT}}(\delta) = \frac{C_+}{1+\delta^2/(\gamma_+^2/4)} - \frac{C_-}{1+\delta^2/(\gamma_-^2/4)}\,, \tag{3.2}$$

with different heights C_+ and C_-, and different widths γ_+ and γ_-. Indeed, as it is shown in figure 3.2(a), the absorption profile at low driving field is composed of a positive Lorentzian function, which corresponds to the linewidth of the excited level, and a negative one, which corresponds to the narrow transparency window.

3.1.3 Autler-Townes splitting model

When, the Rabi frequency of the control field is large, no simple and exact expression can be written anymore for the absorption. However, for $\Omega \gg \Gamma$, the absorption of the signal field can be approximated by a sum of two well-separated Lorentzians functions,

$$A_{\mathrm{ATS}}(\delta) = C\left[\frac{1}{1+(\delta+\delta_0)^2/(\gamma^2/4)} + \frac{1}{1+(\delta-\delta_0)^2/(\gamma^2/4)}\right], \tag{3.3}$$

detuned from the origin by $\pm\delta_0$ and with the same width γ. Indeed, when the Rabi frequency of the control field is large compared with the natural linewidth, two dressed states in the excited level appear, as it has been shown on figure 3.2(c). However, it is important to point out that the full transparency at zero detuning in the absorption profile for high Ω is a signature of the EIT interference effect. Because of this full transparency, the expression of A_{ATS} does not match perfectly the absorption profile for Rabi frequency not very large compared to Γ.

Robustness to decoherence A main difference between the ATS and EIT phenomena is their *robustness* against decoherence, namely the dephasing rate γ_{gs} between the two ground states. Figure 3.3 presents the absorption spectra in each regime but with a large dephasing rate, $\gamma_{gs} = 0.25\,\Gamma$. ATS is robust to decoherence and the two dressed-states in the excited level remain even when γ_{gs} is large. But we clearly see that EIT is very sensitive to decoherence and that the transparency dip disappears completely when γ_{gs} becomes close to Γ. This feature confirms again that the observation of

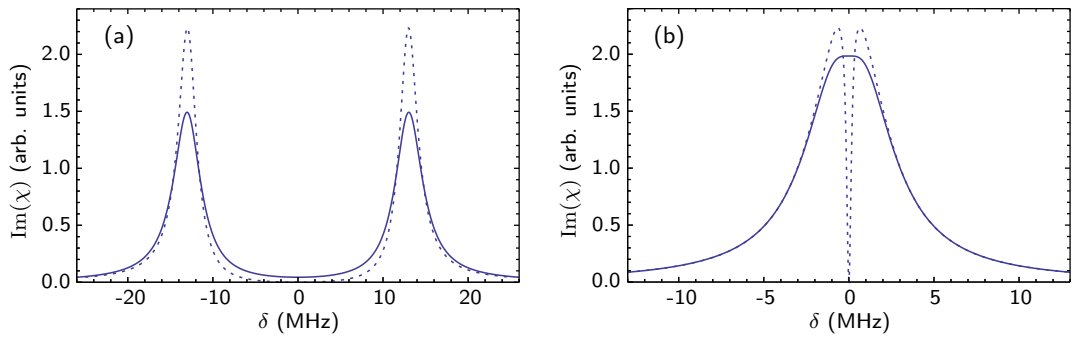

FIGURE 3.3 : Absorption spectra for (a) $\Omega = 5\,\Gamma$ and (b) $\Omega = 0.25\,\Gamma$ with a large dephasing rate $\gamma_{gs} = 0.25\,\Gamma$. Dashed lines correspond to a small dephasing rate, $\gamma_{gs} = 10^{-4}\,\Gamma$.

transparency in the presence of a control field is not necessary the signature of EIT, and a quantitative test is very welcome [Anisimov et al., 2011].

The test proposed in [Anisimov et al., 2011] aims at determining which of these two generic models is the most likely for given experimental data. Our well-controlled system is well-suited for testing such criterion.

3.2 Experiment

In the former section, the EIT and ATS models have been introduced. Now, we want to record absorption profiles for a signal field interacting with our ensemble of cold atoms, in the presence of a control field with various Rabi frequencies. The aim is then to compare the absorption profiles with the two models. Here we detail the experimental setup to obtain these profiles.

The experimental setup is illustrated in figure 3.4. The atomic ensemble is obtained from cold cesium atoms in a magneto-optical trap (MOT). The three-level system involves the two ground states, $|g\rangle = |F = 3\rangle$ and $|s\rangle = |F = 4\rangle$, and one excited state $|e\rangle = |F' = 4\rangle$. The atomic ensemble is prepared in the $|F = 3\rangle$ ground state. The control field is on resonance with the $|F = 4\rangle \rightarrow |F' = 4\rangle$ transition while the signal field is scanned around the $|F = 3\rangle \rightarrow |F' = 4\rangle$ transition with a detuning δ (see inset). Both fields propagate in the atomic cloud with a small angle, and the signal is detected after the MOT.

Inverted scheme As shown in chapter 2, every elements of the experiment have been initially designed to operate with all the atoms in $|F = 4\rangle$, the control field driving the $|F = 3\rangle \rightarrow |F' = 4\rangle$ transition and the signal field probing the $|F = 4\rangle \rightarrow |F' = 4\rangle$. However the phase-lock between the two lasers allows to scan only the frequency of the $|F = 3\rangle \rightarrow |F' = 4\rangle$ laser. For this reason, we invert the scheme for this specific study.

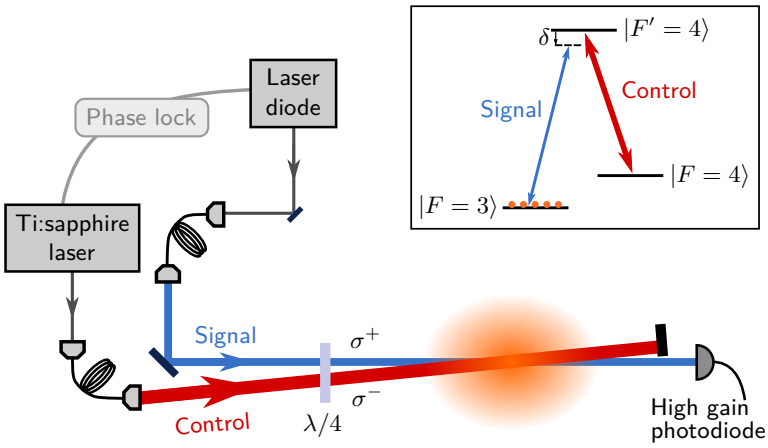

FIGURE 3.4 : Experimental setup. A weak signal beam and a control beam travel through a cloud of cold cesium atoms. Atoms are initially in the ground state $|F = 3\rangle$. The signal field is close to the $|F = 3\rangle \rightarrow |F' = 4\rangle$ transition with a two-photon detuning δ, while the control field drives the $|F = 4\rangle \rightarrow |F' = 4\rangle$ transition on resonance.

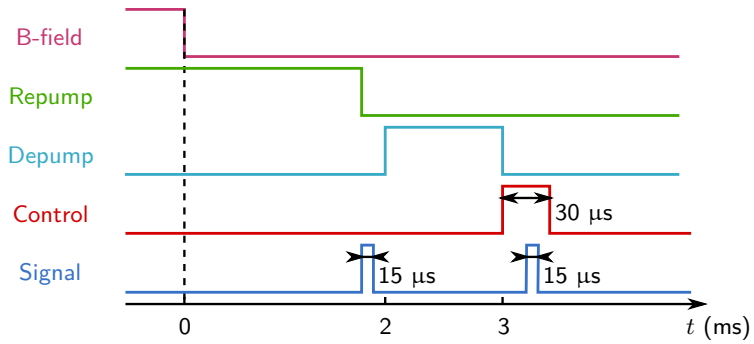

FIGURE 3.5 : Temporal sequence for the absorption profile acquisition. At $t = 2$ ms, a depump pulse transfers the atoms to the $|F = 3\rangle$ state, and the measurement takes place 1 ms later. While the 30 µs-long control pulse is applied, a 15 µs-long signal pulse probes the medium. A reference signal pulse is sent before $t = 2$ ms when the atoms are still in $|F = 4\rangle$ in order to measure the initial intensity of the signal pulse.

3.2.1 Preparation of the atomic medium and timing

In this study, the atomic ensemble is prepared in a slightly different manner than presented in chapter 2 in order to initially set all the atoms in the ground state $|F = 3\rangle$. First the MOT is loaded and ends up with atoms in $|F = 4\rangle$ (see section 2.1). Then, 2 ms after the trapping field extinction a σ^--polarized depump laser coupling the $|F = 4\rangle$ to the $|F' = 4\rangle$ excited state brings the atoms into $|F = 3\rangle$ (see timing on fig. 3.5). The depump pulse is 1 ms-long, has a power of 900 µW and propagates through the atomic cloud along the control path. Because of the polarization of this depump beam, the atoms do not equally populate all the Zeeman sublevels. For instance the extreme sublevel $|F = 3, m_F = +3\rangle$ is empty (section 3.4.1). In addition, we verify that no atoms remain in the other ground state $|F = 4\rangle$ by sending an on-resonance light, which is not absorbed within our experimental precision.

The optical depth in $|F = 3\rangle$ is chosen around 3, sufficiently small in order to not absorb completely the on-resonance signal. Thus, the high-gain photodiode can still detect the signal pulse and any shape distortion of the absorption profiles is avoided. The residual magnetic field is canceled 3 ms after the trapping field extinction via the microwave spectroscopy (section 2.2).

3.2.2 Signal and control fields

Generated by a Ti:Sapphire laser, the control beam is σ^--polarized. The signal beam comes from an extended-cavity grating stabilized laser diode locked in phase and in frequency with the Ti:Sapphire laser (appendix A). The signal beam is σ^--polarized and has a power of 30 nW. The angle between the two paths is 2°. The dephasing rate γ_{gs} between the two ground states is estimated to be $10^{-2}\,\Gamma$ in our experiment. It is limited by the laser linewidths as well as the locking between the two lasers. Moreover, simulations of absorption profiles with $\gamma_{gs} = 10^{-2}\,\Gamma$ are in agreement with our experimental data.

The control pulse is applied 3 ms after the extinction of the trapping magnetic field with a duration of 30 µs (figure 3.5). During this time a 15 µs-long signal pulse with a given detuning δ is sent through the atomic ensemble. At t =2 ms, when only the $|F = 4\rangle$ state is populated, a first signal pulse enables us to get a reference I_0 of the signal intensity. Finally the absorption profile corresponding to the signal pulse absorption $A = -\ln(I_0/I)$ as a function of the detuning δ from resonance (see appendix B for details) is obtained.

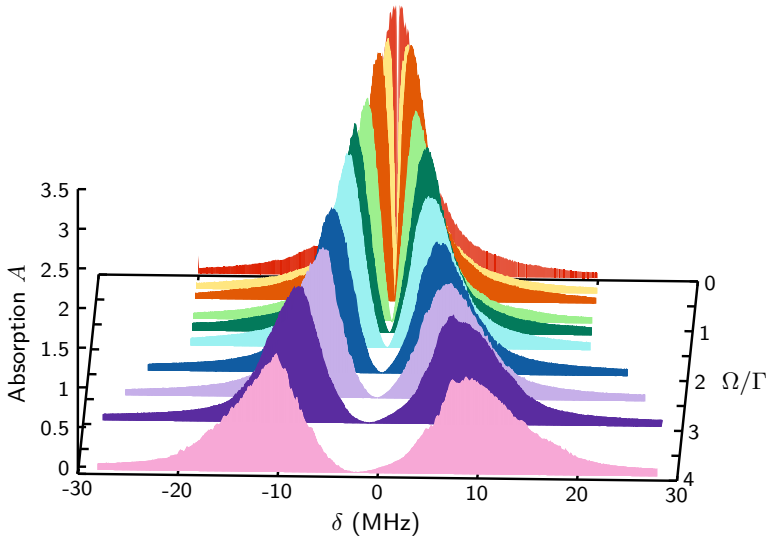

FIGURE 3.6 : Absorption spectra for values of the Rabi frequency of the control between 0.1 to 4 Γ. They correspond to the absorption of the signal field as a function of its detuning δ.

3.2.3 Absorption spectra

Absorption profiles are given in figure 3.6 for various values of the Rabi frequency Ω of the control field. By changing the control power from 100 nW to 200 µW, Ω ranges from 0.1 to 4 Γ. For low driving fields (at the back) spectra exhibit a narrow transparency window, which gets wider as the control power increases, until the appearance of two well-separated resonances corresponding to two dressed-states in the excited level for large driving field (at the front). One can already notice that the two resonances are asymmetric, with different heights, widths and detunings. Moreover, the shape of the peaks strongly differs from the theoretical Lorentzian shape for large Ω. These effects are due to the manifold structure of the cesium D_2 line, as seen later in this chapter.

3.2.4 Rabi frequency of the control

The absorption profiles are plotted for different values of the control Rabi frequency Ω. Here we detail how we define this Rabi frequency. Basically, the definition of the Rabi frequency for the control field is

$$\Omega = \frac{|d_{se}|E_c}{\hbar}\,, \tag{3.4}$$

where d_{se} is the electric dipole moment between $|s\rangle$ and $|e\rangle$, E_c is the amplitude the control field, i.e. twice the positive frequency part. The intensity I_c of the control field connects E_c and the power P via the transverse section S of the beam, the vacuum permittivity ϵ_0 and the speed of light c in vacuum,

$$I_c = \frac{1}{2}\epsilon_0 c E_c^2 = \frac{P}{S}\,. \tag{3.5}$$

Thus, the Rabi frequency of the control can be written as a function of our experimental parameters, in particular the power P,

$$\Omega = \frac{\sqrt{2}}{\hbar\sqrt{\epsilon_0 c}}|d_{se}|\sqrt{\frac{P}{S}}\,. \tag{3.6}$$

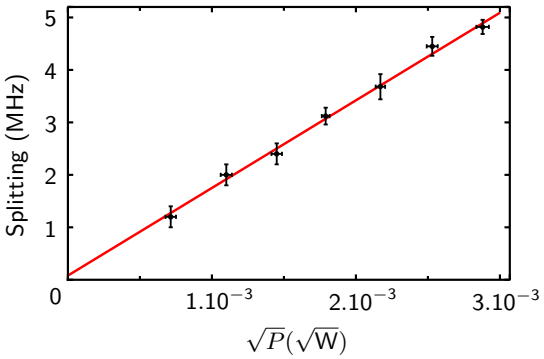

FIGURE 3.7 : Experimental splitting as a function of $\sqrt{P}$, where P is the control power, fitted by a linear function with a slope of 1670 $\pm$ 100 MHz/$\sqrt{\mathrm{W}}$.

Because the system is not a real three-level system, the calculation of the electric dipole moment d_{se} must take into account all the possible transitions given the control polarization and also the population in each Zeeman sublevel. Furthermore, the effective section S of the beam is not simply πw_0^2 where w_0 is the control beam waist, but depends on the interaction region defined by the atoms, the signal and the control beams, which is not predictable with a good precision. As a consequence calculating Ω via the equation 3.6 does not allow to obtain values of the Rabi frequency of the control with reasonable error bars for this study.

Thus, we operate an experimental calibration of Ω as a function of the power. The two maxima of the absorption profiles are separated by Ω, even in a multiple level system, for $\Omega < \Gamma$. We plot the splitting measured on the absorption spectra as a function of the square root of the power, which is a linear function, as shown in equation 3.6. Figure 3.7 shows the corresponding curve together with the linear fitting, leading to $\Omega = \alpha\sqrt{P}$ with $\alpha = 1670 \pm 100$ MHz/$\sqrt{\mathrm{W}}$.

3.3 Fitting of the absorption profiles

We follow the method proposed by [Anisimov et al., 2011] and fit the absorption profiles by the two models, A_{ATS} and A_{EIT}. However, the models must be adapted to the experimentally observed behavior by introducing additional parameters. Because of the asymmetry mentioned above for large Rabi frequency of the control, three parameters are added in the ATS model to fit the different heights, C_1 and C_2, the different detunings δ_1 and δ_2, and the different widths γ_1 and γ_2. Moreover, we introduce a shift ϵ between the positive and negative Lorentzian terms in the EIT model because of a possible slight offset in the frequency locking point of the Ti:Sapphire laser. Therefore, the two models used to fit the experimental spectra are given by

$$A_{\mathrm{EIT}} = \frac{C_+}{1+(\delta-\epsilon)^2/(\gamma_+^2/4)} - \frac{C_-}{1+\delta^2/(\gamma_-^2/4)}\,, \tag{3.7}$$

$$A_{\mathrm{ATS}} = \frac{C_1}{1+(\delta+\delta_1)^2/(\gamma_1^2/4)} + \frac{C_2}{1+(\delta-\delta_2)^2/(\gamma_2^2/4)}\,. \tag{3.8}$$

Figure 3.8 shows the absorption profiles and the model fits for two values of the control Rabi frequency Ω. Experimental data are presented together with the best fits of functions $A_{\mathrm{EIT}}(C_+, C_-, \epsilon, \gamma_+, \gamma_-)$ (red lines) and $A_{\mathrm{ATS}}(C_1, C_2, \delta_1, \delta_2, \gamma_1, \gamma_2)$ (green lines). Parameters C_+, C_-, C_1, C_2 representing the amplitudes of the absorption curves are in dimensionless units, while the parameters $\epsilon, \gamma_+, \gamma_-$ and

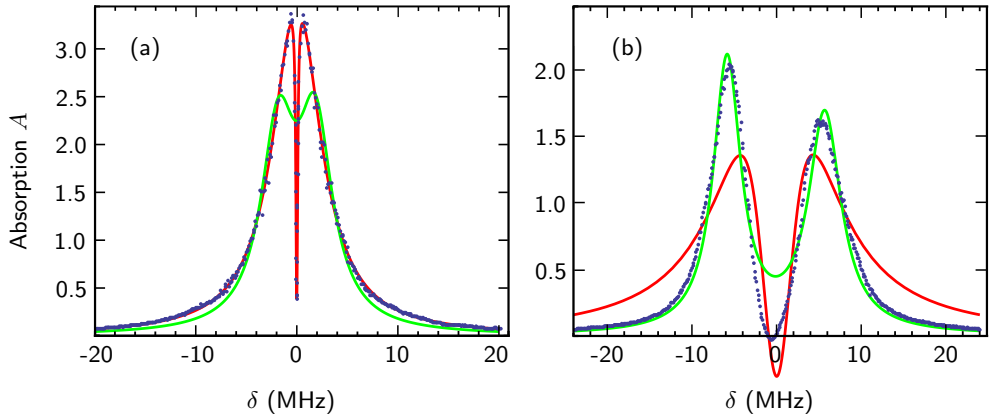

FIGURE 3.8 : Experimental absorption spectra (blue dots) fitted by the EIT model (red solid lines) and the ATS model (green solid lines) for (a) $\Omega = 0.2\,\Gamma$ and (b) $\Omega = 2.3\,\Gamma$.

$\delta_1, \delta_2, \gamma_1, \gamma_2$ representing detunings and widths are in MHz. In the case of a small Rabi frequency $\Omega = 0.2\,\Gamma$, the EIT model $A_{\rm EIT}(3.52, 3.14, 1.45 \times 10^{-2}, 5.71, 0.239)$ fits the experimental data much better than the ATS one, $A_{\rm ATS}(2.01, 2.04, 1.84, 1.84, 4.14, 4.08)$. On the contrary, for a large Rabi frequency $\Omega = 2.3\,\Gamma$, $A_{\rm ATS}(2.05, 1.64, 5.86, 5.67, 3.94, 4.68)$ fits the data better than $A_{\rm EIT}(1.59 \times 10^5, 1.59 \times 10^5, 1.45 \times 10^{-7}, 8.17, 8.17)$. Thus, as expected, the EIT model fits better for low driving fields while the ATS model fits better for high driving fields.

3.3.1 Akaike weights

In order to quantitatively compare the quality of the fits as in [Anisimov et al., 2011], we apply the Akaike information criteria, which is based on the Akaike information

$$I_j = 2k_j - 2\ln \mathcal{L}_j \tag{3.9}$$

where k_j is the number of parameters of the model $j = {\rm EIT}$ or ATS and $\mathcal{L}_j$ is the maximized likelihood function. The smallest value of I_j indicates the best model [Burnham and Anderson, 2002]. We calculate the Akaike information $I_{\rm EIT}$ and $I_{\rm ATS}$ via the *NonLinearModelFit* function of Mathematica. Then, we estimate the Akaike weights as

$$w_{\rm EIT} = \frac{e^{-I_{\rm EIT}/2}}{e^{-I_{\rm EIT}/2} + e^{-I_{\rm ATS}/2}}\,, \tag{3.10}$$

$$w_{\rm ATS} = \frac{e^{-I_{\rm ATS}/2}}{e^{-I_{\rm EIT}/2} + e^{-I_{\rm ATS}/2}}\,. \tag{3.11}$$

The Akaike weights give a relative measurement of the likelihood of the models, normalized to unity. Figure 3.9 presents the Akaike weights (red and green triangles) as a function of the normalized Rabi frequency Ω/Γ. They exhibit a binary behavior, $w_{\rm EIT}$ being very close to 1 and $w_{\rm ATS}$ to 0 when $\Omega \leq 1.15\,\Gamma$ and the opposite for higher Ω. Thus, an abrupt transition is observed around $\Omega = 1.2\,\Gamma$ between the EIT and ATS models. This means that for Rabi frequency of the control smaller than $1.2\,\Gamma$, the EIT model is the best model, and on the contrary the ATS model is better when $\Omega > 1.2\,\Gamma$.

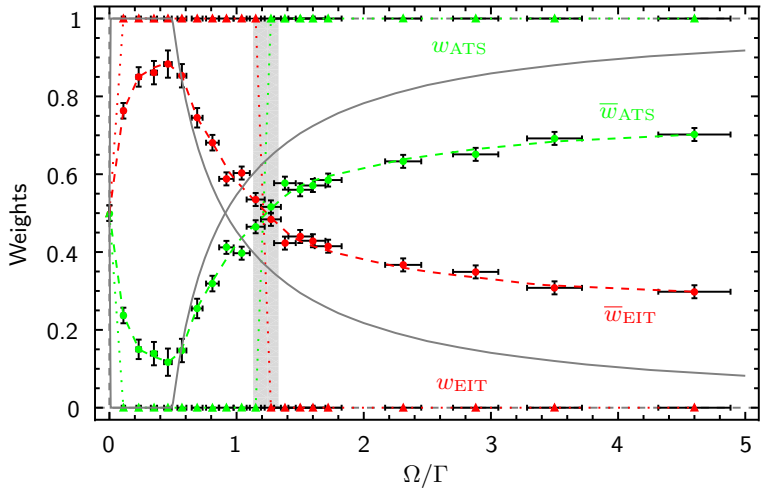

FIGURE 3.9 : Experimental Akaike weights as a function of the Rabi frequency Ω/Γ for ATS model (green triangles) and for EIT model (red triangles) and experimental per-point weights for ATS model (green dots) and for EIT model (red dots). The grey area indicates the EIT/ATS model transition. Error bars include the uncertainty on the coefficient α and on the measured power. The solid lines give the theoretical per-point weights for a pure three-level system.

3.3.2 Per-point Akaike weights

In order to access to a more sensitive criteria we calculate the so-called per-point weights, defined as:

$$\overline{w}_{\mathrm{EIT}} = \frac{e^{-I_{\mathrm{EIT}}/2N}}{e^{-I_{\mathrm{EIT}}/2N} + e^{-I_{\mathrm{ATS}}/2N}}, \tag{3.12}$$

$$\overline{w}_{\mathrm{ATS}} = \frac{e^{-I_{\mathrm{ATS}}/2N}}{e^{-I_{\mathrm{EIT}}/2N} + e^{-I_{\mathrm{ATS}}/2N}}, \tag{3.13}$$

where N is the number of experimental points in the absorption profile. The division of the Akaike information by N corresponds to a contrast reduction of the relative weights. Thus, they give more details about the relative likelihood of the models.

Per-point Akaike weights are displayed in figure 3.9 for EIT model (red dots) and ATS model (green dots). The maximum value of $\overline{w}_{\mathrm{EIT}}$ is 0.9 while the asymptotic value of $\overline{w}_{\mathrm{ATS}}$ at large Ω is 0.7. As a consequence, we conclude that EIT model is more likely for small Ω than ATS model for large Ω. Moreover, the crossing point between the two models is the same as the one given by the first calculated Akaike weights, $\Omega = 1.23 \pm 0.1\,\Gamma$. The region defined by the transition point and its error bar is represented by the gray area.

Theoretical simulations are performed from the exact expression of the susceptibility given in equation 3.1. On fig. 3.9 the gray lines correspond to per-point Akaike weights in the case of a pure three-level system. The experimental per-point weights are in qualitative agreement with the three-level system simulation but three different features can be noticed:

1. The behavior of $\overline{w}_{\mathrm{EIT}}$ differs for low driving field, in particular the experimental maximum value is smaller than the theoretical one, which is 1.
2. The crossing between the two models occurs theoretically at $\Omega/\Gamma = 0.9$, a lower value than the one obtained experimentally.
3. The theoretical asymptotic value of $\overline{w}_{\mathrm{ATS}}$, 0.92, is larger that the one found in the experiment.

Thus, as expected, our system is not well described by a simple three-level system. Further theoretical

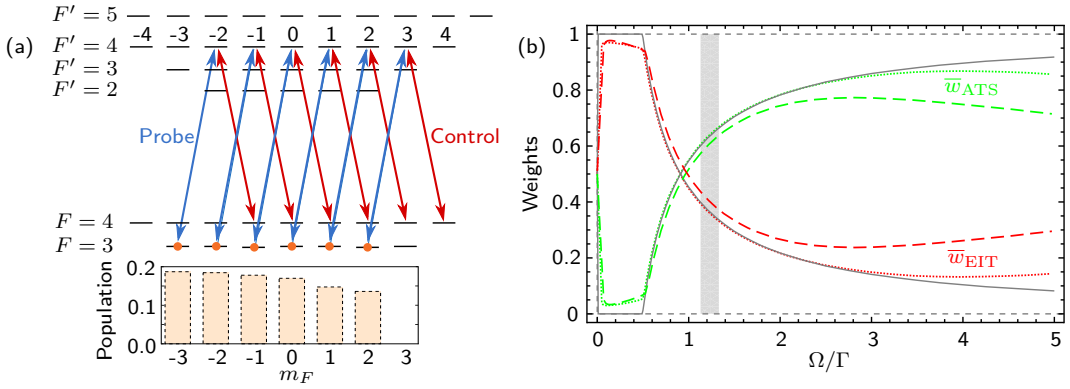

FIGURE 3.10 : Theoretical simulations with multilevel structure. (a) Level scheme for the cesium D_2 line and the six-level transitions involving Zeeman sublevels; inset: population distribution. (b) Per-point weights for a three-level system (gray lines), for a sytem involving hyperfine structure (dotted lines) and for a system involving Zeeman sublevels (dashed lines).

investigations have been conducted in order to explain the observed experimental behavior.

3.4 Theoretical simulations

The complete hyperfine and Zeeman structures are taken into account, as well as the residual Doppler broadening. This part is mainly the work of our collaborators in Saint Petersburg, Alexandra Sheremet and Dmitriy Kupriyanov. A summary is given in the following.

3.4.1 Multilevel structure

The full hyperfine structure of the excited state $6^2P_{3/2}$ is first considered, based on a previous theoretical model developed in the group for the study of EIT in warm vapors at room temperature [Mishina et al., 2011, Scherman et al., 2012]. This structure explains the asymmetry between the two resonances but do not strongly influence the shape of the per-point weights curves. On figure 3.10(b) the dotted lines represents the per-point Akaike weights for the six-level system. The new per-point weights slightly differ from the ones calculated in the three-level system case for very small and very large Rabi frequency of the control Ω, but the transition point remains close to $\Omega/\Gamma = 0.9$.

Then, we take into account the Zeeman structure, which consists in several sublevels in each hyperfine state (see fig. 3.10(a)). The atomic distribution in each Zeeman sublevel is determined by simulating the optical pumping due to the depump field applied before the absorption measurement. The resulting population distribution is shown in the inset of fig 3.10(a). Because control and signal fields propagate with opposite circular polarization, the system is simplified to six independent subsystems in a Λ-configuration with different Rabi frequency. Consequently, the atomic susceptibility is calculated as the sum of the susceptibilities for each subsystem.

Theoretical per-point weights taking into account both the hyperfine and Zeeman structures are displayed with dashed lines on fig. 3.10(b). We note that the Rabi frequency of the control field is estimated in the same way as in the experimental case, i.e. from the distance between the two maxima of the absorption profiles. The crossing between the weights for EIT and ATS models occurs at $\Omega = 0.98\,\Gamma$, i.e. relatively close to the value in the three-level case. Thus, the transition point varies only slightly by

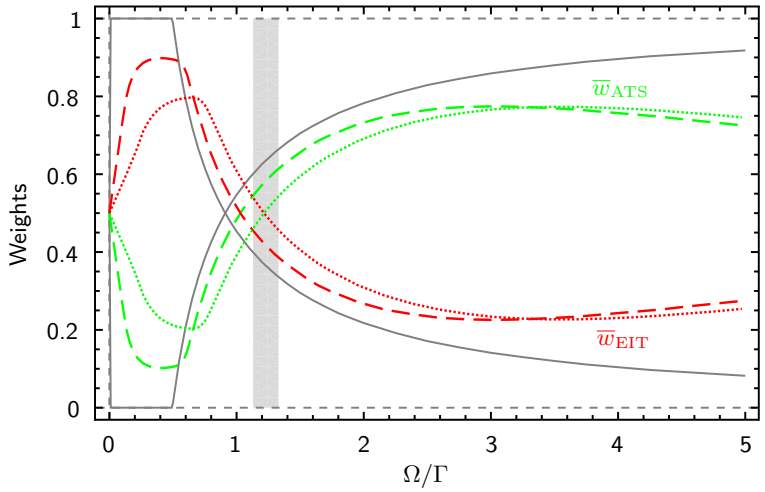

FIGURE 3.11 : Theoretical simulations with Doppler broadening. Per-point weights for a three-level system (gray lines), for a sytem involving Zeeman structure and residual Doppler broadening of $\Gamma_D/2\pi =$ 0.6 MHz (dashed lines) and 1.3 MHz (dotted lines).

considering the Zeeman structure, and is still not in agreement with the experimental value. However, significant changes of per-points weights values at large Ω are observed, with an asymptotic value around 0.7 for $\overline{w}_{\mathrm{ATS}}$, and this new behavior corresponds to the one observed experimentally. The latter is due to the fact that the six independent subsystems have different Rabi frequencies and this feature leads to the distortion of the Lorentzian resonances for strong control field.

3.4.2 Doppler broadening

Finally, inhomogeneous broadening due to residual Doppler broadening is included. The value of the residual Doppler broadening Γ_D is estimated by fitting an experimental absorption profile without control field by the convolution of a Lorentzian function of width Γ and a Gaussian function of width Γ_D. We find $\Gamma_D/2\pi =$ 0.6 MHz, corresponding to a temperature of 800 µK. Figure 3.11 presents the simulated $\overline{w}_{\mathrm{EIT}}$ and $\overline{w}_{\mathrm{ATS}}$ for $\Gamma_D/2\pi =$ 0.6 MHz (dashed lines). They exhibit a crossing point at $\Omega = 1.05\,\Gamma$, in much better agreement with the experiment. Moreover the shape of the per-points weight curves is similar to the shape of the experimental curves, and in particular the reduction of $\overline{w}_{\mathrm{EIT}}$ for small Ω is also observed.

The slightly larger value of the experimental transition point is very likely to be due to heating and additional broadening caused by the control laser. The Doppler broadening is increased up to $\Gamma_D/2\pi =$ 1.3 MHz (dotted lines), the crossing occurs at $\Omega = 1.23\,\Gamma$.

Therefore, including in the model both the Zeeman structure of the atomic system and the finite temperature of the atoms enables us to explain the observed experimental behavior when the criterion is applied.

Conclusion

What we have seen:

- We tested and analyzed in details the transition between the ATS and EIT models in a well-controlled system.
- The criterion proposed in [Anisimov et al., 2011] has been calculated and gives a consistent conclusion for discerning between the two regions.
- The manifold structure and residual inhomogeneous broadening must be considered to explain our experimental behavior, which clearly differs from the simple three-level model.

In consequence:

- The discrimination criterion is suitable in an experimental case.
- Furthermore, the witness is very sensitive to the specific medium properties, and potentially provides a practical characterization tool for complex systems.

Chapter 4

Quantum memory for orbital angular momentum of light

Contents

Thanks to its unique properties, orbital angular momentum (OAM) of light [Allen et al., 2003] provides a large range of applications [Torres and Torner, 2011], and is in particular of major interest for quantum information applications. Indeed, in opposite to other optical degrees of freedom such as polarization, the unbounded orbital angular momentum of light offers the potential of high-dimensional Hilbert space for information encoding and processing. Thus, photons having helical wavefronts are good information carriers in order to increase the capacity of quantum information encoding and processing.

From the first demonstration of entanglement of twisted photons [Mair et al., 2001], several quantum communication implementations based on OAM of light have indeed been developed, such as quantum cryptography [Gröblacher et al., 2006], coin tossing [Molina-Terriza et al., 2005], or bit commitment [Langford et al., 2004]. Very recently, extremely high-dimensional entanglement have been demonstrated,

up to 12-dimensional systems [Dada et al., 2011], or with modes having up to $\pm$ 300 units of OAM [Fickler et al., 2012].

In order to extend these works to quantum networks, it is essential to develop light-matter interface involving OAM of light. Great advances have been realized with the demonstration of entanglement between an ensemble of cold atoms and photons carrying OAM via to the DLCZ scheme [Inoue et al., 2006, Inoue et al., 2009]. Moreover, storage of bright light in Laguerre-Gaussian modes [Pugatch et al., 2007, Moretti et al., 2009], and very recently in the single-photon regime [Veissier et al., 2013, Ding et al., 2013] have been shown. However, no evidence of coherence in the mapping process has been reported, which will prove the quantum character of the storage of OAM encoded qubit.

Laguerre-Gaussian modes form a set of optical modes having a twisted structure, and thus describe modes of light carrying OAM. They are noted LG_p^l, where l is the azimuthal index corresponding to the OAM of light in $\hbar$ units and p is the radial index. We particularly focus here on the so-called doughnut modes, $\mathrm{LG}_0^{\pm 1}$, which present a vanishing intensity in the center and an OAM equal to $\pm\hbar$. Using the LG^{+1} and LG^{-1} modes, one can encode a qubit on OAM of light, as a coherent superposition of these two modes, that is in fact a Hermite-Gaussian mode of the first order (appendix D).

Thus, the goal is to store and retrieve an OAM encoded qubit via the dynamic EIT protocol in an ensemble of cold atoms, and is achieved in two steps. First a memory for photons carrying OAM in the single photon regime is built, demonstrating the preservation of the handedness of the wavefront in the single-photon regime. This work is published in Optics Letters 38 (5), 712-714, *Reversible optical memory for twisted photons*. Second the reversible storage of OAM encoded qubits is demonstrated in the quantum regime. This second step requires to perform a full state tomography of the retrieval qubit states, and to compare the obtained fidelities to the classical bound. This result is published on arXiv, *A quantum memory for orbital angular momentum photonic qubits*, still under review at Nature Photonics.

4.1 Optical memory for twisted photons in the single-photon regime

The first experiment consists in developing an optical EIT-based memory for Laguerre-Gaussian modes imprinted on very weak pulses of light. We show that our memory preserves the handedness of the helical phase structure at the single-photon level.

4.1.1 Experimental setup

The optical layout for the storage of twisted photons at the single-photon level is presented on figure 4.1. From left to right, it is composed of first the Laguerre-Gaussian mode generation via spatial light modulator (SLM), then the memory setup, and finally the detection of the retrieved modes via holographic masks and photon counting. We now see in details these three parts.

4.1.1.1 Mode generation

Laguerre-Gaussian (LG) modes are generated by a spatial light modulator (SLM, Hamamatsu LCOS-SLM X10468-02), based on liquid crystals, with a resolution of 792 $\times$ 600 pixels. The collimated signal beam

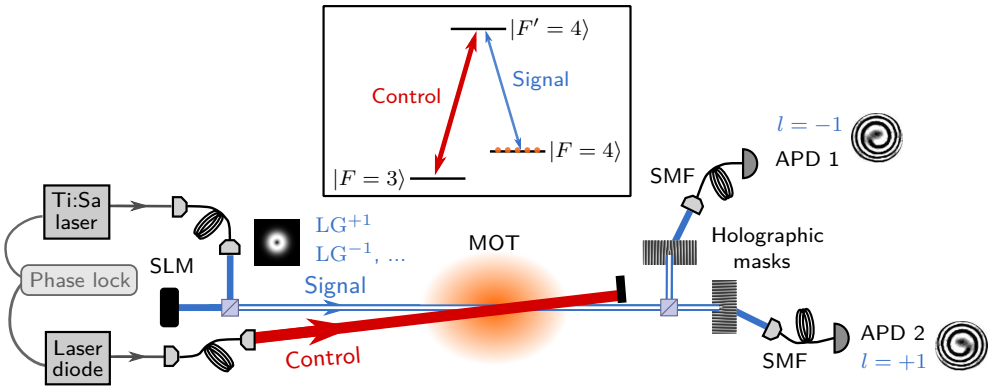

FIGURE 4.1 : Optical layout for the storage and analysis of Laguerre-Gaussian modes in the single-photon regime. A signal pulse consisting of a very weak coherent state is orbitally shaped by reflection on a spatial light modulator (SLM) and then mapped into an ensemble of cold cesium atoms via the dynamic EIT protocol (relevant energy diagram in inset). After a user-defined delay, the collective atomic excitation is readout. The retrieved light is analysed via splitting on a 50/50 beam-splitter and an OAM mode projection on each path. This projection results from an OAM addition (for the $l = -1$ path) or subtraction (for the $l = +1$ path) through diffraction by blazed fork holograms and a subsequent coupling into single-mode fibers (SMF). The coupled light is finally detected by avalanche photodiodes (APD).

in a TEM_{00} mode is reflected on the SLM, on which is applied the appropriate phase profile of the mode we want to create. To generated LG modes, we apply the rotating phase profiles, shown in figure 4.2. Because of the phase jump at the center of the signal beam, the intensity vanishes around the beam axis. The weak signal pulse is thus in the corresponding LG mode and carries one unity of OAM. It is then focused into the atomic ensemble for storage.

The SLM is easy to use and versatile. Indeed, any mode can in principle be generated, just by changing the phase profile on the SLM software. Figure 4.2 shows the various phases applied on the SLM and their corresponding intensity profiles to the phase front for the modes we are interested in. For instance, Hermite-Gaussian modes of the first order can be created by applying a π phase jump pattern. A flat phase can also be set in order to let the signal beam in the fundamental gaussian mode for alignment purpose for instance. However, the mode generation by phase modulation only, as implemented here, is not perfect and higher order modes, in particular $\mathrm{LG}_{p>0}$, are created at the same time. The solution we tried, such as operating diffraction and amplitude modulation via the SLM, have not been successful, whereas the lack of space does not allow us to filter the unwanted modes.

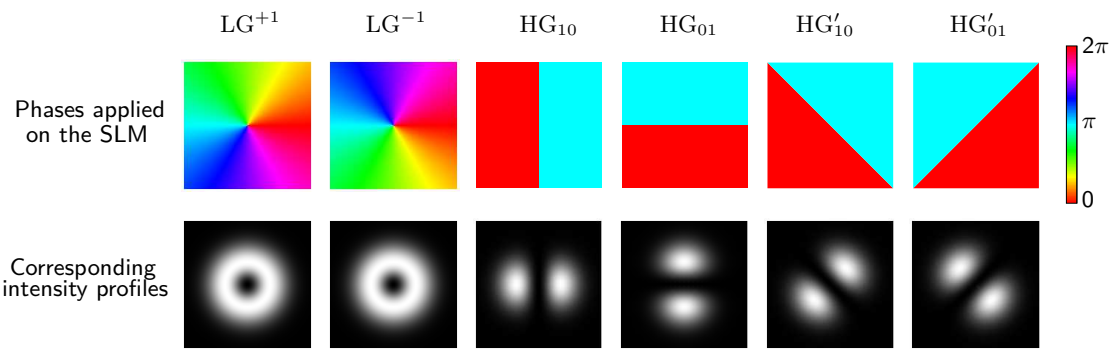

FIGURE 4.2 : Phase profiles applied on the SLM, and their corresponding intensity profiles, for the two Laguerre-Gaussian modes $\mathrm{LG}^{\pm 1}$, and for the Hermite-Gaussian modes of the first order horizontal (HG_{10}), vertical (HG_{01}), diagonal (HG'_{10}) and antidiagonal (HG'_{01}).

4.1.1.2 Implementation of the reversible mapping

The ensemble of cold atoms is prepared in the $|F = 4\rangle$ ground state as described in section 2.1, with an optical depth of 15 for the signal field. The weak signal field, with a typical mean photon number per pulse of 0.6, comes from a Ti:Sapphire laser and is on resonance with the $|F = 4\rangle \rightarrow |F' = 4\rangle$ transition (inset of figure 4.1). The control field, which drives the EIT-based storage, couples the other ground state $|F = 3\rangle$ to the excited state $|F' = 4\rangle$. The control beam has a power of 15 µW and is generated by a laser diode, locked in phase and in frequency with the Ti:Sapphire laser (appendix A). Both fields have linear, but orthogonal, polarization and propagate with a 2° angle .

The signal pulse is shaped into a half-Gaussian temporal profile with a $1/e$ width equal to 300 ns (see boxed paragraph). Initially on, the control field is cut in 50 ns, after the signal pulse compression inside the medium. The storage lasts here 1 µs and the control field is switched on and allows the retrieval of the signal pulse. Many repetitions of this memory sequence occur in a MOT cycle, 100 during 1 ms, for a global repetition rate of 4 kHz of the memory cycles.

Shaping the signal pulse Optimal storage does not involve square pulse as basically produced by acousto-optic modulators (AOM) because highest frequency component does not fit into the transparency window and some are even not absorbed by the medium. Furthermore, the dynamic EIT protocol involves signal pulse compression along the atomic ensemble, and due to the finite length of the medium, some pulse shapes optimize the storage and retrieval efficiency. The optimal shape can be found by implementing an iterative method, proposed in [Novikova et al., 2007], which consists in sending the input pulse with the output time-reversal shape. After some steps, the input pulse shape looks like the output time-reversal one, converging approximately to a half-Gaussian shape. This shape also minimizes the leakage of the signal pulse during the writing process. The temporal shaping is realized in our experiment by mixing the RF signal that drives the AOM, before its amplification, with a Gaussian envelop from an arbitrary signal generator (Agilent 33250A). The temporal width of the Gaussian, as well as the maximum and the offset of the amplitude are easily set on the signal generator. Then, the Gaussian-shaped RF signal is gated by a trigger signal in order to cut the residual RF signal outside of the pulse. This is also how we produce the half-Gaussian shape, with a controllable cutting time. All these parameters are adjusted to optimize the memory efficiency.

4.1.1.3 Detection at the single-photon level

An easy way to characterize the spatial properties of Laguerre-Gaussian modes is to use imaging techniques, as it has been used in many experiments involving bright beams. The intensity profile can be observed by simply detecting the beam with a CCD camera, while the phase profile can be observed by making the LG mode interfere with a TEM_{00} mode It can results in spiral patterns and the direction of rotation indicates the sign of l. These spiral patterns are depicted on figure 4.1, but only as illustration of the detection process. However, such imaging methods cannot be used at the single-photon level.

Several techniques have thus been developed for single-photon OAM detection [Berkhout et al., 2010, Leach et al., 2002, Mair et al., 2001, Vaziri et al., 2002, Lavery et al., 2012]. Here we choose to work with a combination of a computer-generated hologram and a single-mode fiber to implement a mode discriminator [Mair et al., 2001, Vaziri et al., 2002]. Blazed fork phase holograms diffract the light into the first order with good efficiency (> 80 %), and depending on the fork pattern orientation, adds or

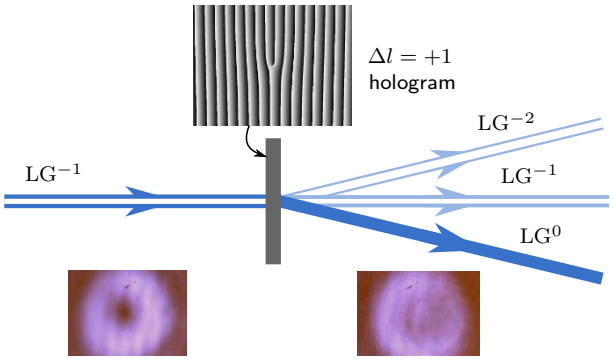

FIGURE 4.3 : Operation of a $\Delta l = +1$ blazed fork phase hologram. An incident LG^{-1} mode is diffracted through the holographic mask and becomes a fundamental Gaussian mode by addition of an OAM unit. Others residual modes can be observed. The same hologram can operate as a $\Delta l = -1$ hologram if the fork pattern is reversed.

subtracts one OAM of light. Figure 4.3 shows the operation of such a $\Delta l = +1$ hologram. A LG^{-1} mode is transformed into the fundamental Gaussian TEM_{00} mode by addition of one OAM unit, and can be coupled to a single-mode fiber. The single-mode fiber filters out the residual modes that are generated, and allows the mode discrimination. Indeed, by sending the opposite LG^{+1} mode which becomes a LG^{+2} mode after the hologram, the light intensity at the fiber output vanishes. What is detected after the $l = -1$ path results thus from a LG^{-1} mode with a probability close to unity.

The detection part is actually made up of two paths, the signal beam being split on a 50/50 beam-splitter after going out from the atomic ensemble (figure 4.1). On the $l = +1$ path, the holographic mask subtracts one OAM of light ($\Delta l = -1$), and an incident LG^{+1} mode is coupled into the single-mode fiber. On the $l = -1$ path, the $\Delta l = +1$ hologram enables to detect LG^{-1} mode. Finally, photon counters (Perkin-Elmer SPCM-AQR-14-FC) detect the signal field at the fiber output on each path. Both LG^{+1} and LG^{-1} components of an incident light pulse are therefore measured at the same time.

Alignment of the mode discriminators is done with bright beams. First, the incident light must be perfectly centered on the fork pattern in order to well-transform a LG mode into a Gaussian one. This alignment consists in superimposing the two opposite optical vortices, observed by a CCD camera after the hologram, in order to reconstruct a Gaussian mode (see images on figure 4.3). Then, we characterize each mode discriminators by measuring the coupling efficiency for a set of input modes and we compare them with the coupling efficiency of the mode we want to select, which is around 77 %. Typical values are showed in table 4.1. High distinction ratios are obtained, i.e. 17 and 23 dB for Gaussian and opposite LG modes respectively. The normalized coupling efficiencies for the HG modes should be in principle all equal to 50 %, but we observe losses and unbalancing. Unbalancing occurs between the different Hermite-Gaussian modes into a mode discriminator, but also for a given HG mode into the two mode selectors. This is due to the finite precision of the alignment we perform, and to imperfections in the mode generation done only by phase modulation. Thus, higher radial modes $\mathrm{LG}_{\mathrm{p}>0}$ are present and contribute more in the HG mode creation than in the LG mode one.

LG^{-1}	LG^{0}	LG^{+1}	HG_{10}	HG_{01}	HG'_{10}	HG'_{01}
5.10^{-3}	$1.6.10^{-2}$	1	0.38	0.42	0.32	0.46

TABLE 4.1 : Characterization of the mode sorting path $l = +1$ consisting of a hologram and a single-mode fiber. Typical values for coupling into the single-mode fiber as a function of the input mode, normalized by the LG^{+1} coupling (here equal to 76 %).

Thanks to this experimental setup, we can send LG modes and their superpositions into the atomic ensemble, perform the EIT-based memory, and analyze the retrieved modes. In the following, the results are presented.

4.1.2 Experimental results

Signal pulses in different OAM states are stored inside the ensemble of cold atoms, and observed on the two detection paths $l = +1$ and $l = -1$ simultaneously. Detected events on each APD are collected in order to produce histograms, corresponding to the number of events as a function of time (see appendix C for more details on the data acquisition). Figure 4.4 displays as a table the histograms. The photonic information is mapped into collective excitations when the control field is turned off. After a delay of 1 µs, the control field is switched on and the atomic excitation is transferred back into light pulse. The switching time as well as the power of the control field are adjusted in order to optimize the retrieval (see boxed paragraph).

The first two lines give the results respectively for an impinging LG^{+1} and LG^{-1} mode. Memory

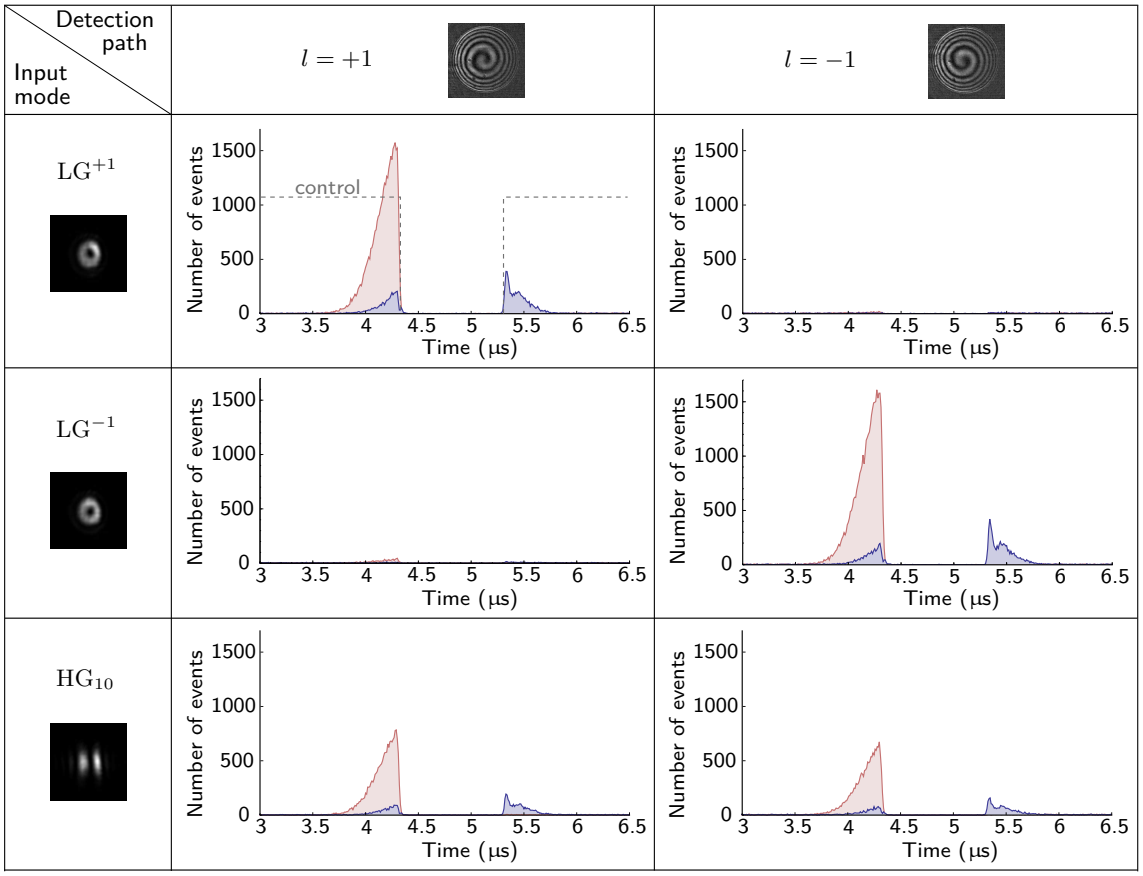

FIGURE 4.4 : Storage and retrieval of LG^{+1}, LG^{-1}, and HG_{10} modes at the single-photon level. For the two simultaneous detection paths, the number of counts is represented as a function of time. Red areas represent the incoming signal pulses recorded without atoms and blue areas correspond to memory measurements. The events around the incoming pulses show the leakage of the signal while the later events correspond to the readout. The dotted line in the first plot shows the timing of the control pulse. Each curve results from $5{\times}10^5$ repetitions of the experiment.

measurements (blue areas) exhibit a first peak corresponding to the leakage of the signal pulse during the writing process, and a second peak, which is the retrieved pulse. The main feature of this memory experiment is the fact that no event is observed on the detection path with l opposite to the one of the stored state, within our distinction ratio. However, on the detection path with same l, a significant quantity of light is detected in the reading process. By dividing this quantity to the number of events contained in the pulse reference (red areas), we access to the memory efficiency, $\eta = 16 \pm 2$ %. Therefore, the reversible mapping described here, which operates at the single-photon level, preserves the OAM of light. Furthermore, similar efficiency has been measured during the storage of a TEM_{00} mode, the best being $\eta = 24 \pm 3$ %. Thus, it seems possible to achieve similar efficiency with LG modes than for the fundamental Gaussian mode.

Optimizing the control field After optimizing the position of the control beam, as described in chapter 1 (section 2.1.3), two parameters of the control field are adjusted to optimize the memory efficiency.

1. Power. As detailed in chapter 1 (section 1.3.1.3), a trade-off needs to be found between the delay and the transparency. A control field with low power induces a large dispersion of the medium, namely a large delay for the signal pulse enables to compress the signal pulse entirely inside the atomic cloud. However, the width, and the depth if other effects have to be taken into account, of the transparency window are small, therefore the signal pulse experiences a lot of absorption, i.e. losses. On the contrary, a high driving field leads to a wider and deeper transparency window, so the signal is poorly absorbed. Yet, the reduction of the group velocity is not large enough to enable the total compression of the signal pulse inside the ensemble, and a considerable leakage is observed before the switching off of the control field. For a pulse duration of 300 ns, we find an optimum value for the control power around 20 μW. From the observed delay, in this case 200 ns, we estimate the Rabi frequency of the control around 1.15 Γ, the length of the atomic ensemble being 2 mm and the optical depth 15. The group velocity of the signal is approximately 3.3 $\times 10^{-5}\, c$, therefore the spatial length of the pulse drops from 90 m to 3 mm. However, the compressed pulse is still longer than the atomic ensemble, and a leakage is observed (8 % in average here). The EIT bandwidth is about $2\pi\times$ 2.2 MHz $\approx 1/460$ ns.

2. Switching time. In principle, the control pulse should be cut when the whole signal pulse is contained inside the medium. Because of the finite length of the atomic ensemble, the switching must occur after as much light as possible has entered the medium, but before too much signal leaks out. Thus, by changing the cutoff time of the control, the energy contained in the leakage clearly varies, and depending on the optical depth of the atomic ensemble and the control power, an optimum can be found. For instance, after increasing the control power, the control must be switched off earlier, in order to reduce the leakage. Here, we cut off the control few tens of ns before the signal pulse, and due to the acousto-optic modulator, the control is cut within 50 ns. However, no additional shaping of the control field is needed if the signal pulse is already shaped [Novikova et al., 2007].

As shown in the last line of figure 4.4, we also store and retrieve a HG_{10} mode. This state is an equally weighted superposition of LG^{+1} and LG^{-1} states, so it is expected to detect half of the events on each APD. This is indeed what we observed on the last row of figure 4.4, considering the unbalancing between the two paths (section 4.1.1.3), equal here to 9% for the HG_{10} mode. Furthermore, the storage efficiency η is the same for each LG component than for individual storage presented just above, within

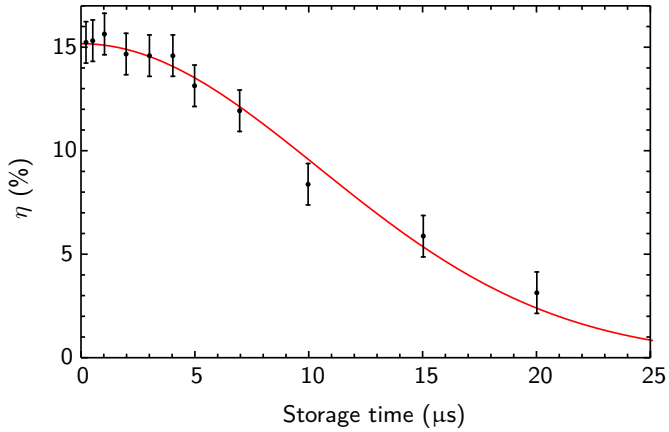

FIGURE 4.5 : Retrieval efficiency as a function of the storage time for a LG^{-1} mode, detected in the $l = -1$ path. Experimental points are fitted by a Gaussian function, with a $1/e$ time constant of 15 μs.

our experimental precision.

Storage time We also study the retrieval efficiency as a function of the storage time, as shown in figure 4.5. The experimental points are fitted by a Gaussian distribution e^{-t^2/τ^2} with a time constant τ of 15 μs. This behavior corresponds to a dephasing due to motional dephasing, as introduced in chapter 1 (section 1.3.2), for a temperature of the atoms of 1 mK and an angle of $\theta = 2°$. Further cooling of the atoms and optical pumping to clock state would improve the memory time around 100 μs, as limited by the loss of atoms from the excitation region. To achieve larger values, as required for practical quantum networking applications, other trapping techniques have to be implemented, enabling optical storage in the second range as demonstrated for instance in light-shift compensated optical lattices [Dudin et al., 2013].

In conclusion, an EIT-based memory for light carrying OAM at the single-photon level has been demonstrated. The OAM degree of freedom of very weak coherent light pulse is preserved upon the storage and retrieval processes. Moreover, OAM superposition has been stored and measurements, which give access to the diagonal elements of the density matrix, have been realized. This opens the way towards the reversible mapping of qubit encoded in OAM of light, which requires additional coherence measurements to prove that it indeed operates in the quantum regime. We now explain how we measure the coherence of an OAM encoded qubit, and reconstruct the full density matrix.

4.2 Quantum memory for OAM encoded qubit

The second step of our experimental developments has been to perform the complete state tomography of a qubit encoded in the OAM degree of freedom, after storage inside our memory device via dynamic EIT. This requires a more sophisticated detection part, and we choose to operate with an interferometry technique in order to measure the coherences of the qubit. Here we still imprint OAM of light on attenuated coherent pulses at the single-photon level. However, this can be taken into account in the computation of quantum memory benchmarks [Specht et al., 2011, Gündoğan et al., 2012], which provide a classical bound for the fidelity of the retrieved qubit. We thus demonstrate the quantum character of our memory device.

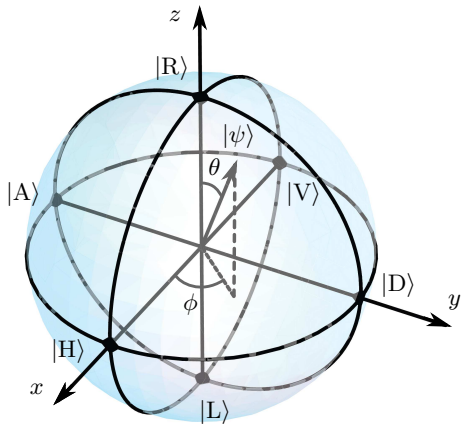

FIGURE 4.6 : Bloch sphere with the $|\mathrm{R}\rangle$ and $|\mathrm{L}\rangle$ states corresponding to Laguerre-Gaussian modes on the poles, and the general qubit state $|\psi\rangle$, defining by the angles θ and ϕ. On the equator the $|\mathrm{H}\rangle$, $|\mathrm{D}\rangle$, $|\mathrm{V}\rangle$ and $|\mathrm{A}\rangle$ states, correspond to Hermite-Gaussian modes.

As said before, spatial modes carrying OAM of light can be used to encode quantum information. In this physical implementation, a qubit can be described in the basis $\{|\mathrm{R}\rangle, |\mathrm{L}\rangle\}$, where the state $|\mathrm{R}\rangle$ ($|\mathrm{L}\rangle$) represents a photon in the right (left)-handed Laguerre-Gaussian mode. Therefore, the qubit state can be written as a coherent superposition of the two modes,

$$|\psi\rangle = \alpha\,|\mathrm{R}\rangle + \beta\,|\mathrm{L}\rangle\ , \tag{4.1}$$

with $\alpha, \beta \in \mathbb{C}$, and $|\alpha|^2 + |\beta|^2 = 1$. This two-level quantum state can be represented on a Bloch sphere, as shown in figure 4.6, where the $|\mathrm{R}\rangle$ and $|\mathrm{L}\rangle$ states are located on the poles. The vector corresponding to the state $|\psi\rangle$ forms an angle θ with the z-axis, defined by $|\mathrm{R}\rangle$ and $|\mathrm{L}\rangle$, and an angle ϕ with the x-axis in the xy-plane. Thus, we can express the qubit state as

$$|\psi\rangle = \cos\left(\frac{\theta}{2}\right)|\mathrm{R}\rangle + \sin\left(\frac{\theta}{2}\right)e^{i\phi}\,|\mathrm{L}\rangle\ . \tag{4.2}$$

Equally weighted superpositions, with $|\alpha| = |\beta| = 1/\sqrt{2}$, correspond to Hermite-Gaussian modes of the first order (appendix D). In particular, we introduce the states

$$\begin{aligned} |\mathrm{H}\rangle &= \frac{|\mathrm{R}\rangle + |\mathrm{L}\rangle}{\sqrt{2}} \quad , \quad |\mathrm{D}\rangle = \frac{|\mathrm{R}\rangle + i\,|\mathrm{L}\rangle}{\sqrt{2}}\ , \\ |\mathrm{V}\rangle &= \frac{|\mathrm{R}\rangle - |\mathrm{L}\rangle}{\sqrt{2}} \quad , \quad |\mathrm{A}\rangle = \frac{|\mathrm{R}\rangle - i\,|\mathrm{L}\rangle}{\sqrt{2}}\ . \end{aligned} \tag{4.3}$$

corresponding respectively to horizontal, diagonal, vertical and antidiagonal Hermite-Gaussian modes. These four states, with $\theta = \pi/2$, are located on the equator of the Bloch sphere. In fact, the qubit state $|\psi\rangle$ can be expressed in the basis $\{|\mathrm{H}\rangle, |\mathrm{V}\rangle\}$, or $\{|\mathrm{D}\rangle, |\mathrm{A}\rangle\}$

$$|\psi\rangle = \frac{\alpha+\beta}{\sqrt{2}}\,|\mathrm{H}\rangle + \frac{\alpha-\beta}{\sqrt{2}}\,|\mathrm{V}\rangle = \frac{\alpha-i\beta}{\sqrt{2}}\,|\mathrm{D}\rangle + \frac{\alpha+i\beta}{\sqrt{2}}\,|\mathrm{A}\rangle\ . \tag{4.4}$$

In analogy with polarization qubit [James et al., 2001], the density matrix can be expressed as a

function of the Stokes parameters S_i as:

$$\hat{\rho} = \frac{1}{2}\left(\hat{1} + \sum_{i=1}^{3} S_i \hat{\sigma}_i\right) , \tag{4.5}$$

where $\hat{1}$ is the identity matrix and $\hat{\sigma}_i$ are the Pauli spin operators. In order to determine the parameters S_i, three linearly independent measurements must be performed on the qubit. In our case, the three spatial basis $\{|\mathrm{R}\rangle, |\mathrm{L}\rangle\}$, $\{|\mathrm{H}\rangle, |\mathrm{V}\rangle\}$ and $\{|\mathrm{D}\rangle, |\mathrm{A}\rangle\}$ are used to this end. Then, the reconstruction of the density matrices can be performed, as it has been done in various physical systems for polarization qubit [Choi et al., 2008, Specht et al., 2011, Gündoğan et al., 2012, Clausen et al., 2012]. In order to characterize our memory device, we propose to store a set of qubit states, reconstruct the density matrices of the retrieved states, and finally compare the obtained fidelities with the classical bound.

4.2.1 Measuring the qubit coherence

The qubit density matrix, and in particular the coherence terms, is measured via an interferometry technique, which is based on the former experimental setup. After explaining the technique, we show how we access the interferometer phase, and how interference fringes are then obtained.

4.2.1.1 Interferometry technique

The detection setup is displayed on figure 4.7. The two detection paths consisting in holograms and single-mode fibers are combined thanks to a fiber beam splitter (Evanescent Optics, 954P polarization-maintaining 50/50 non-polarizing fiber couplers) in order to form a Mach-Zehnder interferometer. Thus, when the qubit is sent into the interferometer, both its $|\mathrm{R}\rangle$ and $|\mathrm{L}\rangle$ components interfere, constructively or destructively depending on the phase shift $\Delta\varphi$ between the two arms and on the qubit phase ϕ.

We described here the transformation of the qubit state by the interferometer. Only for this paragraph, we note the photons in Laguerre-Gaussian state as $|l\rangle$, where l is the OAM of the photon. Thus, $|\mathrm{R}\rangle = |+1\rangle$, $|\mathrm{L}\rangle = |-1\rangle$, $|0\rangle$ is the fundamental TEM_{00} mode, and $|\pm 2\rangle$ are Laguerre-Gaussian modes of the second order. The input qubit, initially in the state $|\psi\rangle = \alpha\,|+1\rangle + \beta\,|-1\rangle$, is first split into two equal parts by a first 50/50 non-polarizing beam splitter (BS1). Then, each path is diffracted on an hologram, which changes the OAM number. On the R path, a unit of OAM is subtracted, $|l\rangle \overset{\mathrm{Holo\,R}}{\rightarrow} |l-1\rangle$, while on the L path, a unit of OAM is added $|l\rangle \overset{\mathrm{Holo\,L}}{\rightarrow} |l+1\rangle$. After that, the output states are sent into single-mode fibers, where ideally only the fundamental Gaussian state $|0\rangle$ can be coupled. Neglecting losses and unbalancing of beam splitters, the qubit state transformation can be written as follows in the R and L paths

$$\begin{aligned} &\alpha\,|+1\rangle + \beta\,|-1\rangle \overset{\mathrm{Holo\,R}}{\rightarrow} \alpha\,|0\rangle + \beta\,|-2\rangle \overset{\mathrm{Fiber}}{\rightarrow} \alpha\,|0\rangle , \\ &\alpha\,|+1\rangle + \beta\,|-1\rangle \overset{\mathrm{Holo\,L}}{\rightarrow} \alpha\,|+2\rangle + \beta\,|0\rangle \overset{\mathrm{Fiber}}{\rightarrow} \beta\,|0\rangle . \end{aligned} \tag{4.6}$$

Finally, the two paths are recombined on the second beam splitter BS2, and the two output states are given by

$$\begin{aligned} |a\rangle &\propto \left(\alpha + e^{i\Delta\varphi}\beta\right)|0\rangle , \\ |b\rangle &\propto \left(\alpha - e^{i\Delta\varphi}\beta\right)|0\rangle , \end{aligned} \tag{4.7}$$

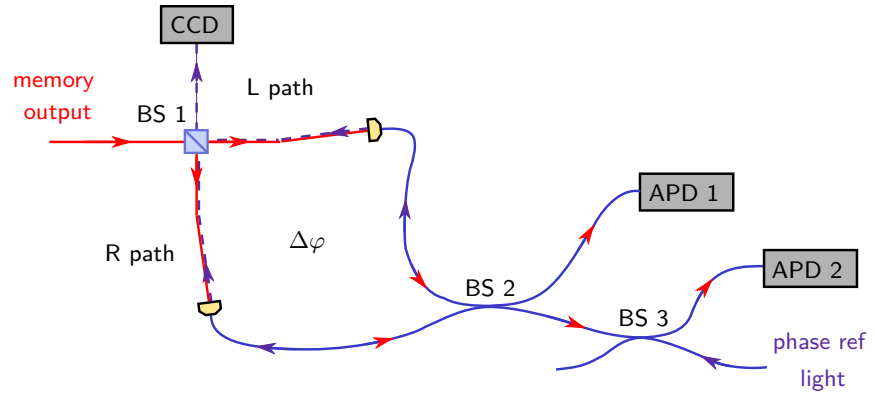

FIGURE 4.7 : Experimental setup for quantum state analysis of OAM qubits. The photons (memory output) enter into a two-path interferometer, defined between beam splitters BS 1 and BS 2, and each path includes a mode projector based on a blazed-fork computer-generated hologram and a single-mode fiber. The two paths are arranged in a way to project the photons respectively into the $|\mathrm{L}\rangle$ mode (L path) and the $|\mathrm{R}\rangle$ mode (R path). Events are detected at the output of a fiber beam-splitter by single-photon counting modules (APD 1 and APD 2). The relative phase $\Delta\varphi$ between the two paths is experimentally determined in a cyclic fashion by sending a phase-reference beam backward (phase ref light) and analyzing its spatial structure at the input of the interferometer via a CCD camera.

where $\Delta\varphi$ is the phase difference between the R and L paths, accumulated between BS1 and BS2. The probabilities to detect events on the single-photon detectors at the outputs are therefore

$$\begin{aligned} P_a &\propto \left|\alpha + \beta\, e^{i\Delta\varphi}\right|^2 , \\ P_b &\propto \left|\alpha + \beta\, e^{i(\pi+\Delta\varphi)}\right|^2 . \end{aligned} \tag{4.8}$$

If the qubit state is an equally weighted superposition the probabilities becomes

$$\begin{aligned} P_a &\propto \cos^2\left(\frac{\phi+\Delta\varphi}{2}\right) , \\ P_b &\propto \sin^2\left(\frac{\phi+\Delta\varphi}{2}\right) . \end{aligned} \tag{4.9}$$

By scanning the phase $\Delta\varphi$ of the interferometer, fringes can therefore be observed with offsets corresponding to the qubit phase ϕ. Furthermore, by selecting measurement for given phase $\Delta\varphi$, one can project the qubit on any HG states. However, the phase of the interferometer must be first determined, as we now explain.

4.2.1.2 Accessing the interferometer phase

A bright light pulse is sent backward into the interferometer in a cyclic fashion in order to measure the phase of the interferometer $\Delta\varphi$ (figure 4.7). For this purpose, the second output of BS 2 is separated in two paths by a second fiber beam splitter, BS 3, the APD 2 being connected to one path, while the other path is used to bring the phase reference light. This light is sent during the MOT loading and the atomic preparation stages, so during 12 ms over 15 ms, which is the MOT cycle duration for this experiment. Moreover, the power is very small, around 1 nW, and the beam is cut by an ensemble of two AOMs, in order to avoid any scattering from this light into the detection paths. The phase reference light has the same frequency and polarization as the photonic qubit, so it experiences the same phase shift $\Delta\varphi$ in the interferometer.

After passing through the holograms, both components of the phase reference light become LG modes, $|\mathrm{R}\rangle$ or $|\mathrm{L}\rangle$. After recombination on BS 1, the resulting beam is thus in a coherent superposition of LG states, with a relative phase $\Delta\varphi$. The last channel of the beam splitter is used to image on a CCD camera the resulting HG mode whose axis of symmetry forms an angle $\Delta\varphi/2$ with the horizontal axis. Pictures are recorded every 125 ms, thus averaged over few MOT cycles, and time-stamped by the computer. The same computer time-stamps also the events detected by the single-photon counters, enabling therefore to associate them to a $\Delta\varphi$ value afterwards.

We access to the value of the interferometer phase by analyzing images from the CCD camera via a Python script (see supplementary information of [Nicolas et al., 2013]). First the center is determined by summing all the images and fitting the resulting doughnut shape image by a ring. Then, images are cut into n slices, where n determines the number of phase bins and must be dividable by 4. The average intensity over each slice is calculated and the two diagonally opposite slices that minimize the intensity define the symmetry axis. We choose $n = 60$, which corresponds to a discretization of 6° for $\Delta\varphi$.

4.2.1.3 Observing the interference fringes

The phase $\Delta\varphi$ of the interferometer is scanned via a mirror mounted on a piezoelectric stack in the R path. The scanning frequency is set in such a way that the interferometer phase varies by 2π in approximately 10 s, which is large compared to the image recording time of 125 ms. After the image analysis, events detected on the APDs are associated to a $\Delta\varphi$ value, and fringes can be reconstructed.

Figure 4.8(a) shows experimental fringes for the four HG states, recorded before storage on APD 1, which corresponds to the probability P_b from equation 4.9. Data recorded on APD 2 are not displayed here but exhibit fringes proportional to P_a. Experimental points are fitted by the function $P_b^{\mathrm{exp}} = A + B\sin^2(\frac{\pi}{360}(\Delta\varphi + \phi))$, with offsets $(\phi_{\mathrm{H}}, \phi_{\mathrm{D}}, \phi_{\mathrm{V}}, \phi_{\mathrm{A}}) = (-10.1°, 81.5°, 173.8°, 262.1°)$, that must be compared with the ideal offsets, $\left(\phi_{\mathrm{H}}^{th}, \phi_{\mathrm{D}}^{th}, \phi_{\mathrm{V}}^{th}, \phi_{\mathrm{A}}^{th}\right) = (0°, 90°, 180°, 270°)$. Thus, we observed a small global phase shift of the interferometer, of -8.2° in average for these data, which is a typical value in our experimental setup. This small global phase shift is probably due to a small misalignment between the SLM and the holograms axes, or to a tiny difference of polarization between the qubit and the phase reference light, but leads only to a slight reduction in the fidelities calculated afterwards.

Storage of the OAM encoded qubits is performed, based on the dynamic EIT protocol, as detailed in section 4.1. Experimental interference fringes for the retrieved qubits are shown in figure 4.8(b). The offsets determined by fitting, $(-7.3°, 78.9°, 177.6°, 277.8°)$, are slightly different than the ones before storage, and result in a global phase shift of -4.5°.

The visibility can be calculated thanks to the fitting parameters, as $V = B/(2A + B)$. The average visibility for the four input states is 95.8 %, while it is 85.1 % for the four retrieved states. The visibility decreases after storage mostly because of the reduced signal-to-noise ratio. Indeed, the background noise level, displayed as the gray lines on figure 4.8(b), becomes non-negligible relatively to the detected number of photons. The background noise has different contributions. It results from the dark counts of the single-photon detectors, around 100 Hz, and from the residual leakage of the control field into the detected mode, around 500 Hz. After background subtraction, the visibility averaged over the retrieved qubit states becomes 95.7 %, so almost as large as for the input states. The coherence is therefore preserved during the reversible mapping of the qubit into the atomic ensemble.

For LG states, ideally no interference occurs. However, due to the finite distinction ratio between the two paths, small fringes are observed. They are presented in figure E.1 in appendix E, where the

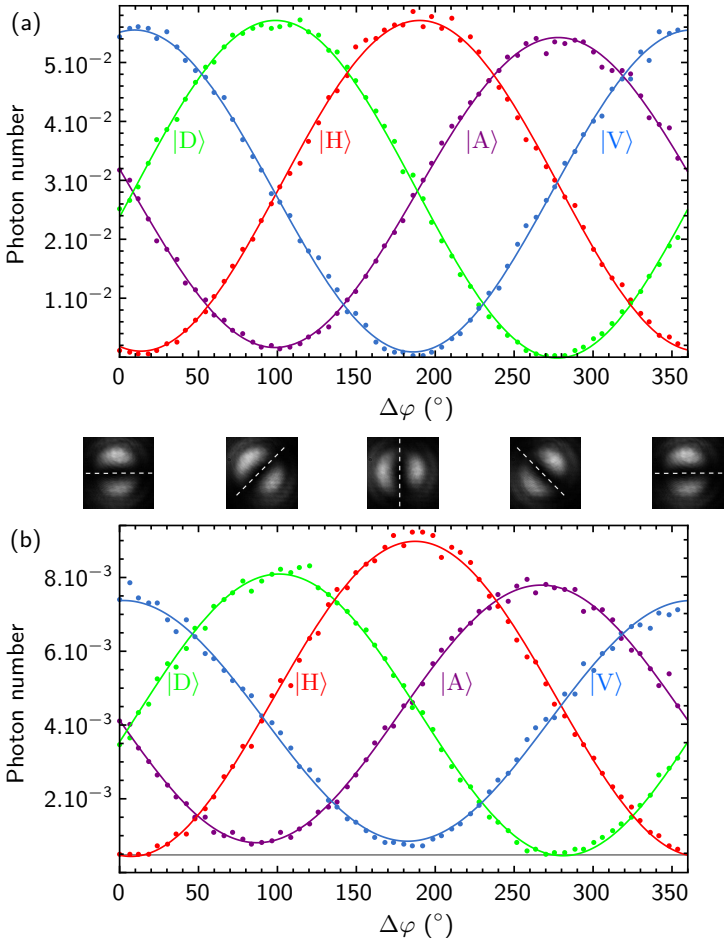

FIGURE 4.8 : Experimental fringes recorded before and after 1 µs storage into the atomic ensemble. The number of photon per pulse detected on APD 1 is displayed as a function of the interferometer phase $\Delta\varphi$ for the four qubit states $|\mathrm{H}\rangle$,$|\mathrm{D}\rangle$, $|\mathrm{V}\rangle$ and $|\mathrm{A}\rangle$, (a) without storage and (b) with storage. Experimental points are fitted by the function $P_b^{exp} = A + B\sin^2(\frac{\pi}{360}(\Delta\varphi + \phi))$, with a set of four offsets $(\phi_\mathrm{H}, \phi_\mathrm{D}, \phi_\mathrm{V}, \phi_\mathrm{A})$ equal to $(-10.1°, 81.5°, 173.8°, 262.1°)$ for the input qubit states and $(-7.3°, 78.9°, 177.6°, 277.8°)$ for the retrieved qubit states. The gray lines represents the background noise level. Images correspond to the phase reference light imaged on the CCD camera for several $\Delta\varphi$ values.

consequences for the fidelity are discussed.

Then, we perform state tomography of the retrieved qubits, and reconstruct the associated density matrices.

4.2.2 Quantum state tomography

Complete state tomography is performed by selecting measurements at some phase interferometer $\Delta\varphi$, and by blocking each arm, in order to project the qubit on the six basis states $|\mathrm{R}\rangle$, $|\mathrm{L}\rangle$, $|\mathrm{H}\rangle$, $|\mathrm{D}\rangle$, $|\mathrm{V}\rangle$, $|\mathrm{A}\rangle$. The density matrix reconstruction is done by calculating the Stokes parameters,

$$\begin{cases} S_1 = & (p_\mathrm{R} - p_\mathrm{L}) \\ S_2 = & (p_\mathrm{H} - p_\mathrm{V}) \\ S_3 = & (p_\mathrm{D} - p_\mathrm{A}) \end{cases}, \tag{4.10}$$

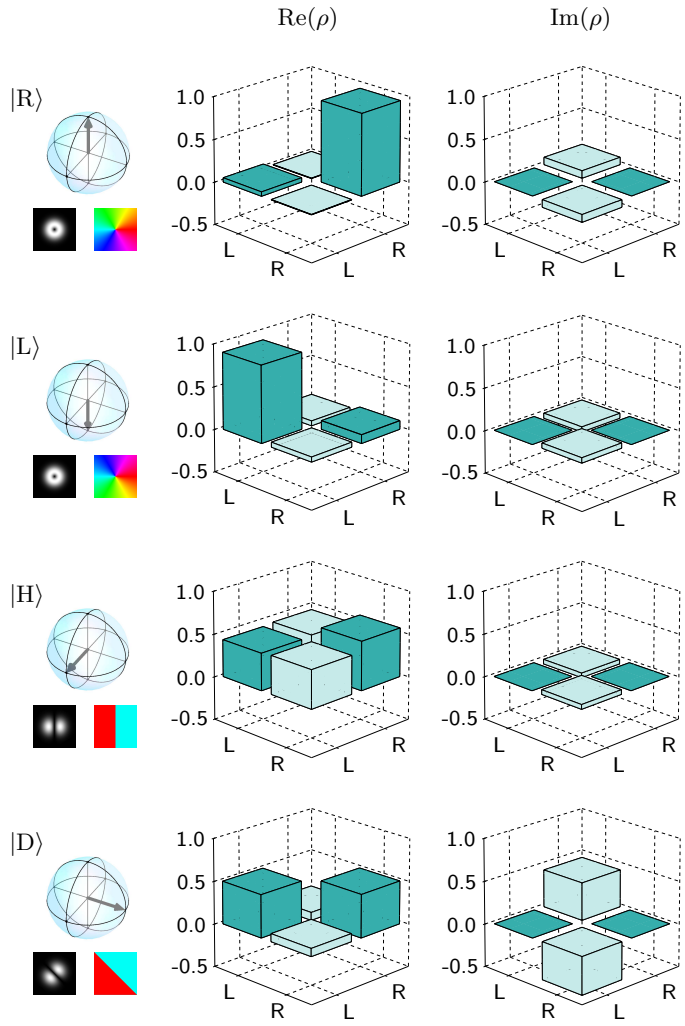

FIGURE 4.9 : Reconstructed density matrices for the four input states $|\mathrm{R}\rangle$, $|\mathrm{L}\rangle$, $|\mathrm{H}\rangle = (|\mathrm{R}\rangle + |\mathrm{L}\rangle)/\sqrt{2}$ and $|\mathrm{D}\rangle = (|\mathrm{R}\rangle + i\,|\mathrm{L}\rangle)/\sqrt{2}$. The mean number of photons per pulse is here $\bar{n}$ =0.6, and no background correction has been applied. The first column shows for each state its location in the Bloch sphere, the phase pattern imprinted by the SLM and the associated spatial mode.

where p_j is the normalized probability of the outcome i, obtained from the relative detected photon number at $\Delta\varphi = \pi - \phi_j^{th} \mod 2\pi$ for $j = \mathrm{H}, \mathrm{V}, \mathrm{D}, \mathrm{A}$, or on the j path with the opposite arm blocked for $j = \mathrm{R}, \mathrm{L}$. From the definition of equation 4.5, the density matrix $\hat{\rho}$ is then expressed and computed as

$$\hat{\rho} = \frac{1}{2}\begin{pmatrix} 1+S_1 & S_2 - iS_3 \\ S_2 + iS_3 & 1-S_1 \end{pmatrix}. \tag{4.11}$$

Density matrices are thus reconstructed from the raw fringes of figure 4.8(b), and from measurements with the arms of the interferometer blocked, which are similar to the measurements performed in section 4.1. Figure 4.9 displays the real and imaginary parts of the density matrices for the two qubit basis states $|\mathrm{R}\rangle$ and $|\mathrm{L}\rangle$, and for two coherent superpositions, $|\mathrm{H}\rangle$ and $|\mathrm{D}\rangle$. The form of the experimental density matrices is similar to the expected one for ideal states. In order to quantitatively determine the fidelity of retrieved qubit density matrices, and to prove that the memory process operates in the quantum regime, we compare to a classical bound.

Input state	Raw fidelity	Corrected fidelity
$\|\mathrm{R}\rangle$	95.1 $\pm$ 0.5 %	99.3 $\pm$ 0.5 %
$\|\mathrm{L}\rangle$	90.0 $\pm$ 0.8 %	97.7 $\pm$ 0.6 %
$\|\mathrm{H}\rangle$	94.7 $\pm$ 0.9 %	98.1 $\pm$ 0.5 %
$\|\mathrm{V}\rangle$	90.3 $\pm$ 1.1 %	98.8 $\pm$ 0.5 %
$\|\mathrm{D}\rangle$	94.0 $\pm$ 0.9 %	98.7 $\pm$ 0.5 %
$\|\mathrm{A}\rangle$	90.6 $\pm$ 1.1 %	96.2 $\pm$ 0.8 %

TABLE 4.2 : Fidelities between the readout states and the ideal states for the six input qubit states without and with background noise subtraction for a mean number of photon per pulse $\bar{n} = 0.6$. Errors were estimated assuming Poissonian statistics and taking into account the phase binning and residual error on the calibration of the interferometer.

4.2.3 Benchmarking

From the calculated density matrices, we compute the fidelity of the retrieved states and compare it to the best classically achievable fidelity.

4.2.3.1 Fidelity with the ideal state

The retrieved qubit state $\hat{\rho}$ is first compared to the ideal pure state $|\psi\rangle$ by computing the fidelity as

$$\mathcal{F} = \langle\psi|\,\hat{\rho}\,|\psi\rangle \ . \tag{4.12}$$

Raw and background corrected fidelities corresponding to a photon number $\bar{n} = 0.6$ are given in table 4.2. Raw fidelities are in average over the six states equal to 92.5 $\pm$ 2 % while averaging over background noise corrected fidelities gives a value of 98.1 $\pm$ 1 %. Thus, the preservation of the coherence during the memory process is once again confirmed. However, these high values correspond to low bounds for the memory characterization as they depend on any imperfections of the mode preparation and detection. In appendix E, we discuss about the influence of first the finite distinction ratio and the unbalancing between the two detection arms and second the offset in the measurement of the interferometer phase.

4.2.3.2 Fidelity with the input state

A way to measure only the memory effect is to compute the fidelity between the input and the output states of the qubit. Because both are mixed states, the fidelity is now expressed as

$$\mathcal{F}_{in/out} = \mathrm{Tr}\left[\sqrt{\sqrt{\hat{\sigma}}\hat{\rho}\sqrt{\hat{\sigma}}}\right]^2 , \tag{4.13}$$

where $\hat{\sigma}$ is the initial density matrix of the qubit. Table 4.3 presents the values of the "in/out" fidelities for the same data as table 4.2. Calculated from raw data, $\mathcal{F}_{in/out}$ is equal to 97.5 $\pm$ 2 % in average, while with background noise subtraction it is in average 99.2 $\pm$ 1 %. Thus, fidelities with the input qubit state exhibit higher values than previous fidelities, confirming that the state analysis limits the fidelity.

We now compute the upper bound for the classical fidelity in order to compare it with the fidelities presented here.

Input state	Raw in/out fidelity	Corrected in/out fidelity
$\|\mathrm{R}\rangle$	98.1 ± 0.5 %	100 ± 0.5 %
$\|\mathrm{L}\rangle$	95.6 ± 0.8 %	98.5 ± 0.6 %
$\|\mathrm{H}\rangle$	98.8 ± 0.9%	99.9 ± 0.5 %
$\|\mathrm{V}\rangle$	98.2 ± 1.1 %	99.1 ± 0.5 %
$\|\mathrm{D}\rangle$	97.5 ± 0.9 %	99.6 ± 0.5 %
$\|\mathrm{A}\rangle$	96.5 ± 1.1 %	98.4 ± 0.8 %

TABLE 4.3 : Fidelities between the readout states and the input states for the six input qubit without and with background noise subtraction for a mean number of photon per pulse $\bar{n}$ =0.6. Errors were estimated assuming Poissonian statistics and taking into account the phase binning and residual error on the calibration of the interferometer.

4.2.3.3 Classical limit

In order to conclude about the quantum character of the reversible mapping, we have to compare the measured fidelities with the best achievable ones using classical resources. The classical strategy consists in measuring the qubit state, classically storing the results and later preparing a new qubit based on the stored results. This corresponds to the so-called "measure-and-resend" attack. Following this strategy, it has been shown [Massar and Popescu, 1995] that the maximal achievable classical fidelity for a state with a fixed photon number N is

$$\mathcal{F}_{lim} = \frac{N+1}{N+2}\,, \tag{4.14}$$

giving the classical limit of 2/3 for single-photons. Using weak coherent states of light with mean photon number $\bar{n}$, this expression must be weighted by the poissonian distribution, and it results in:

$$\mathcal{F}_{lim} = \sum_{N=1}^{\infty} \frac{N+1}{N+2} \frac{e^{-\bar{n}}\bar{n}^N}{N!} \frac{1}{1-e^{-\bar{n}}}\,. \tag{4.15}$$

This classical bound is displayed on figure 4.10 as the blue dashed line. Closed to the single-photon bound of 2/3 for very low $\bar{n}$, the classical fidelity for a poissonian distribution increases up to 1 for large photon numbers. A range of $\bar{n}$ remains accessible for the demonstration of quantum memory, between 0.1 and 10.

Furthermore, if the memory efficiency η is not equal to one, an optimal classical strategy leads to higher values for $\mathcal{F}_{lim}$, making the bound more difficult to beat [Specht et al., 2011, Gündoğan et al., 2012]. A photon number threshold N_{min} is obtained from $\bar{n}$ and η such as the classical strategy is performed if $N > N_{min}$, otherwise losses are induced and no results is given. For $N = N_{min}$, measurement is performed with a probability p, that also depends on $\bar{n}$ and η. Thus, the expression of the best classical achievable fidelity is given by:

$$\mathcal{F}_{lim} = \frac{\frac{N_{min}+1}{N_{min}+2}p + \sum_{N>N_{min}} \frac{N+1}{N+2}\frac{e^{\bar{n}}\bar{n}^N}{N!}}{p + \sum_{N>N_{min}} \frac{e^{\bar{n}}\bar{n}^N}{N!}}\,. \tag{4.16}$$

This classical bound is shown on figure 4.10 for $\eta = 15 \pm 2\%$ as the red shaded region. Raw average fidelities are depicted as purple points, while corrected average fidelities are represented by the green points. Our results beat the classical limit by several standard deviations for a large range of mean photon number, ranging from $\bar{n} = 0.2$ to 20. Thus, we can conclude about the quantum character of our memory device. For very low $\bar{n}$, the fidelity drops below the classical bound because the signal-to-noise ratio becomes too small. At the opposite, for mean photon number above 20, the classical limit becomes too high to beat experimentally. This experiment constitutes the first demonstration of a reversible

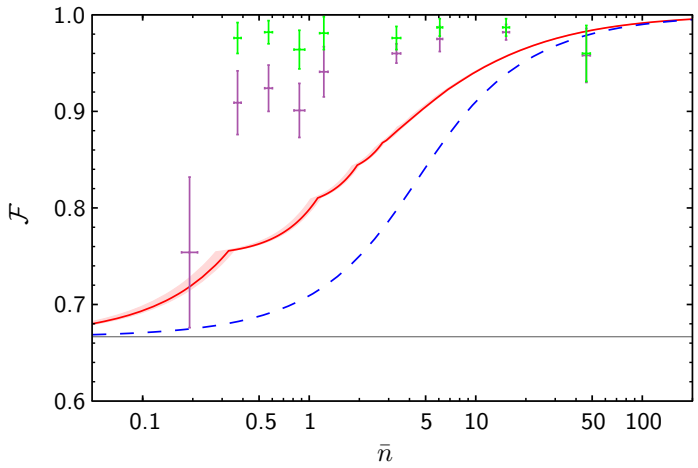

FIGURE 4.10 : Fidelity $\mathcal{F}$ of the retrieved qubit with the ideal state, averaged over the six qubit states, given as a function of the mean photon number per pulse $\bar{n}$. The purple points correspond to the raw data while the green ones are corrected for background noise. The blue dashed line gives the classical limit for a memory with unity storage and readout efficiency and the red line shows the classical limit for the actual efficiency of our memory device (the pink shaded area represents the error bar on the efficiency). Vertical and horizontal error bars indicate respectively standard deviation on the fidelity measurements and on the mean photon number.

quantum memory for photonic OAM encoded qubit. We emphasize here that no dual rail implementation with spatially separated ensembles is required, as usually done for the polarization degree of freedom, due to the intrinsic multimode nature of the storing medium for spatial modes.

Conclusion

What we have seen:

- We have demonstrated the preservation of light OAM upon an EIT-based memory protocol at the single-photon level.
- Furthermore, performing quantum state tomography of OAM encoded qubits, we have shown that the coherence of OAM state superpositions is preserved after storage inside the atomic ensemble.
- Finally, the fidelities of the retrieved qubit states beat the best classically achievable fidelity, demonstrating therefore that the memory operates in the quantum regime.

In consequence:

- This experiment provides the first demonstration of quantum memory for OAM encoded qubits, an important tool for the development of quantum communication protocols based on the OAM degree of freedom.
- This work opens the way towards further investigations, taking advantage of the high-dimensional possibility of OAM, and storing Laguerre-Gaussian states with higher l values.

Chapter 5

Generation of non-Gaussian state of light from atomic ensembles

Contents

Single photons are of major interest for quantum information, and in particular for quantum communications. Whereas faint laser pulses are now widely used in quantum key distribution protocol, single photons will help to implement for instance device-independent protocols, which enable to improve the security [Sangouard and Zbinden, 2012]. Moreover, single photons are also needed for the demonstration of quantum repeaters, which require in the same time light-matter interaction and storage into quantum memories.

The development of single-photon sources compatible with atomic systems is therefore motivated in this context. Main requirements on the single photons include a precise frequency that matches an atomic transition, and a narrow spectrum corresponding to the atomic linewidth. Hence,

atomic systems are naturally good candidates for single-photon generation, which can be realized via atomic cascade [Grangier et al., 1986], four-wave mixing [MacRae et al., 2012], Rydberg blockade [Peyronel et al., 2012, Li et al., 2013, **?**] or via the DLCZ building block [Chou et al., 2004, Laurat et al., 2006].

In the latter case of the DLCZ protocol, the single-photon is heralded by a first photon, emitted during the writing process and announcing the creation of a unique atomic collective excitation. In order to obtain a state with a high single-photon component, i.e. with a low admixture of vacuum, the retrieval of the atomic collective excitation must be efficient and the correlations between the two photons, the heralding and the heralded, have to be strongly non-classical.

The single-photon character is usually demonstrated by calculating the autocorrelation function of the second order, which vanishes in the case of single-photon. Several previous experiments have been performed in this way [Chou et al., 2004, Chanelière et al., 2005, Laurat et al., 2006, Chen et al., 2006]. However, complete state tomography via homodyne detection enables a full characterization in a well-defined spatiotemporal mode and highlights the non-gaussianity of the single-photon state through the Wigner function reconstruction. This has been demonstrated for the first time for a single-photon generated by parametric down conversion [Lvovsky et al., 2001], but has not been investigated for the heralded single-photon generated by DLCZ in an atomic ensemble. Furthermore, the quantum tomography of the heralded single-photon generated by an atomic ensemble is a step towards the quantum engineering of collective excitations, which can be efficiently transferred to light.

In this chapter we first remind how to characterize the implementation of the DLCZ building block in an atomic ensemble, via different parameters quantifying the memory efficiency or the correlations between the photons. Then, the implementation of the so-called DLCZ building block in our ensemble of cold cesium atoms is described, and its characterization is realized. Finally, we perform state tomography on the heralded single-photon via homodyne detection. The density matrix, as well as the Wigner function, are reconstructed.

5.1 Characterizing the DLCZ building block

The DLCZ scheme enables the generation of photon pairs, field 1 and field 2, which can exhibit strong non-classical correlations, as it is the case in parametric down conversion (section 1.2.2). The atomic ensemble can also be seen as a source of heralded single photons, the first scattered photon heralding the emission of a second photon after a programmable delay. The objective being to observe the non-Gaussian character of the heralded single-photon, the system must be optimized to retrieve efficiently the collective excitation into the field 2 photonic state with a low admixture of vacuum. Furthermore, the second photon must exhibit a high suppression of the two-photon contribution. Here we remind how to characterize this protocol via the following parameters: the retrieval efficiency, the correlations between the two photons of the pair, and the autocorrelation function for the heralded photon [Laurat et al., 2006].

Figure 5.1 displays the optical layout for the implementation of the DLCZ building block, and the detection setup for the characterization of the photon pair. We now define different useful quantities. The probability of detecting a photon in field i, either on detector D_{ia} or D_{ib} is noted p_i, with $i = 1$ or 2. In order to measure these quantities, only one detector for each field is sufficient. The conditional probability of having an event j after an event i in the same trial is noted here $p\left(j|i\right)$, with $i, j = 1, 2, 1a, 1b, 2a, 2b$. Then, joint probability p_{ij} corresponds to the probability of detecting in the same trial a photon either in field i or on detector D_i and a photon either in field j or on detector D_j. When $j = i$, p_{ii} is the

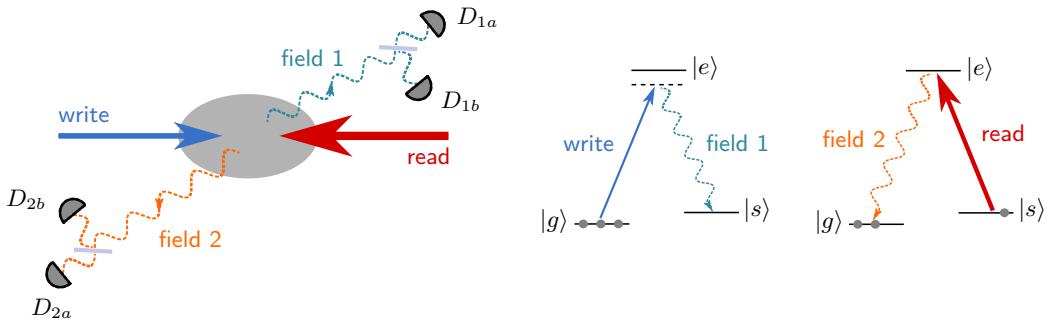

FIGURE 5.1 : DLCZ building block and detection setup for the determination of correlation and autocorrelation functions. A weak write pulse induces a spontaneous Raman transition into field 1. This mode is split by a 50/50 beam splitter and detected by a pair of single-photon counters, D_{1a} and D_{1b}. After a user-defined delay, a strong read pulse enables the transfer of the atomic collective excitation into a photonic mode, called field 2, also detected by a set of two single-photon counters, D_{2a} and D_{2b}.

probability of having an event on detector D_{ia} and another one on D_{ib}, in the same trial, so two photons in the same field i.

5.1.1 Conditional retrieval efficiency

The conditional probability p_c of detecting a field 2 photon after detecting a field 1 photon is in a certain sense equivalent of the storage efficiency for the EIT-based memory. We can write the conditional probability of detecting a field 2 by having a field 1 as

$$p_c \equiv p\,(2|1) = \frac{p_{12}}{p_1}\,. \tag{5.1}$$

It is related to the conditional probability q_c of field 2 emission given a field 1 detection,

$$p_c = \eta_2\, q_c\,, \tag{5.2}$$

where η_2 is the overall detection efficiency for the field 2 photon. This probability q_c is related to the vacuum component of the density matrix of the heralded photon, $q_c \propto 1 - \rho_{00}$. Hence, q_c, and so p_c must be as high as possible in order to observe strong non-gaussianity of the heralded photon. For increasing write power, the probability of creating multiple excitation becomes however non-negligible, and the single-photon character drops. It is therefore important to characterize the correlations between the two photons, as seen now.

5.1.2 Normalized intensity cross-correlation function

The correlations between the two photons are characterized by the normalized intensity cross-correlation function g_{12},

$$g_{12} = \frac{p_{12}}{p_1\, p_2}\,. \tag{5.3}$$

For classical field, the Cauchy-Schwarz inequality for coincidence detection of the two fields is expressed as [Clauser, 1974]

$$R = \frac{g_{12}^2}{g_{11}\, g_{22}} \leq 1 \tag{5.4}$$

where $g_{ii} = p_{ii}/p_i^2$, with p_{ii} being the joint probability of detecting two events on field i. Thus, the quantum character of the photon pair can be proved by the violation of this inequality. In the ideal case, $g_{11} = g_{22} = 2$, so the condition for non-classical correlations simplifies to

$$g_{12} > 2\,. \tag{5.5}$$

The normalized intensity cross-correlation function depends on the Raman scattering probability, $\chi \propto d_0 P_w t_w$, with d_0 the optical depth of the atomic ensemble, P_w the power, and t_w the duration of the write field, as defined in chapter 1 (section 1.2.2). For $\chi \ll 1$, the correlation function can be expressed as

$$g_{12} \approx 1 + \frac{1}{\chi}\,, \tag{5.6}$$

Thus, g_{12} increases when the excitation probability decreases, namely when the write power decreases.

5.1.3 Conditional autocorrelation function

The conditional autocorrelation function w for the detection of two photons from field 2, conditioned upon a field 1 detection is given by

$$w \equiv \frac{p\,(2a, 2b|1)}{p\,(2a|1)\,p\,(2b|1)} = \frac{p_1\,p_{1,2a,2b}}{p_{1,2a}\,p_{1,2b}}\,. \tag{5.7}$$

Ideally, two events are never detected within the same trial in field 2 after a photon is emitted in field 1, so $p_{1,2a,2b} = 0$ and $w = 0$. For a classical field, the Cauchy-Schwartz inequality leads to $w \geq 1$. Thus, fulfilling the condition

$$w < 1 \tag{5.8}$$

is a signature of the single-photon character of field 2. The conditional autocorrelation function is the equivalent to the second-order correlation function, usually noted $g^{(2)}(\tau = 0)$. It represents the extinction of higher excitation number relative to coherent states, and therefore is related to the diagonal elements of the heralded photon density matrix corresponding to photon numbers higher than one, i.e. ρ_{ii} with $i \geq 2$.

In the case of $\chi \ll 1$, the conditional autocorrelation function is simply $w \approx 4\chi$, and is therefore related to the normalized intensity cross-correlation function,

$$w \approx \frac{4}{g_{12}}\,. \tag{5.9}$$

Thus, the value of the conditional autocorrelation function w can be estimated from the measurement of g_{12}.

We now present how we experimentally implement the DLCZ building block and characterize it with the parameters introduced above, the conditional retrieval efficiency and the normalized intensity cross-correlation function, which require only one single-photon detector per photonic mode.

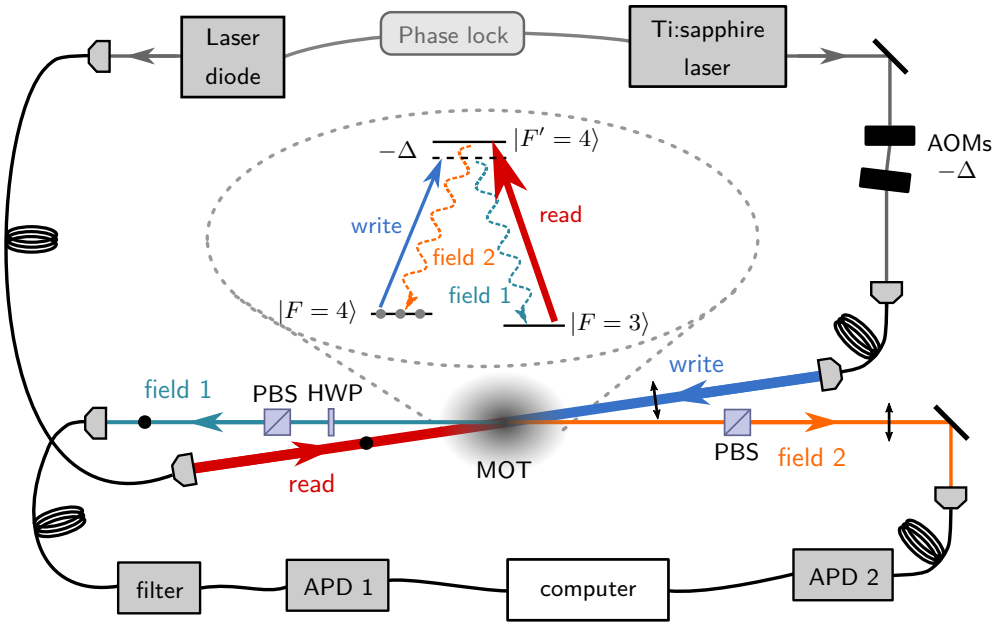

FIGURE 5.2 : Optical layout for the experimental DLCZ building block implementation. A weak detuned write pulse is sent into the ensemble of cold atoms and leads to Raman scattering into the field 1 mode, which is detected with a small angle on a single-photon counter, APD 1, after frequency filtering. The detection of a single-photon in this mode heralds the generation of a collective state in the atomic ensemble. After a programmable delay, a strong read pulse maps out the collective excitation into the field 2 mode, which can be detected on APD 2. Both detector outputs are recorded by computer for analysis. Polarization are indicated as dots for vertical and arrows for horizontal polarization.

5.2 Experimental implementation of the DLCZ building block

5.2.1 Experimental setup

We implement the DLCZ building block in an off-axis configuration, as shown in figure 5.2. The write field is generated by a Ti:Sapphire laser, locked on resonance with the $|F=4\rangle \rightarrow |F'=4\rangle$, and then detuned by $\Delta = -$ 10 MHz thanks to a setup consisting in two acousto-optic modulators. A 100 ns-long weak write pulse, with a power P_w and horizontally polarized, induces with a small probability χ spontaneous Raman scattering into the field 1 mode. This field, projected on a vertical polarization, is coupled into a single-mode fiber and frequency filtered through an atomic filter described in appendix F, in order to ensure that its frequency is around the $|F=3\rangle \rightarrow |F'=4\rangle$ transition. Photons emitted on the adjacent transition, which do not herald the creation of an atomic excitation, are therefore filtered out. The photon is finally detected by an avalanche photodiode (Perkin Elmer, SPCM-AQR-14-FC), APD 1, and heralds the generation of a collective spin state.

After a programmable delay, chosen in our case around 300 ns, short to operate at the maximum of efficiency, a second optical pulse is sent into the atomic ensemble with a vertical polarization to read the collective excitation. This read pulse comes from a laser diode, which is locked in phase and frequency with the Ti:Sapphire laser, and so couples the $|F=3\rangle$ ground state to the $|F'=4\rangle$ excited state. The read pulse has a power $P_r \sim 100$ µW and a duration of 150 ns. This value has been obtained by optimizing the retrieval efficiency. The field 2 photon is selected to be horizontally polarized and sent via an optical fiber to a second single-photon counter, APD 2. Both APD outputs are recorded

by computer and analyzed (appendix C), in order to determine the characteristic quantities introduced above.

The DLCZ trial lasts only 1 µs and occurs 1000 times per MOT cycle. Thus, the mean repetition rate is 67 kHz. Gaussian shapes for write and read pulses are obtained simply because the duration of the wanted pulses is shorter than both the rising and falling times of the acousto-optic modulators (AOM) that switch the light. Furthermore, depending on the alignment of the beam into the AOM, the resulting optical pulse can be much shorter than the trigger signal pulse. That is why they are first characterized using bright light and fast photodetector. After each DLCZ sequence, a second read pulse, with a duration of 200 ns, is used to repump all the atoms in $|F = 4\rangle$.

Some experimental parameters are crucial and must be optimized. In particular, the coupling between the write and the read paths, as well as the coupling between the field 1 and 2 modes, have to be as high as possible. We achieve values around 75 % for both. Moreover, we characterize the detection efficiency for photons in field 1 or field 2, and we obtain $\eta_1 \sim 0.25$ and $\eta_2 \sim 0.3$. These detection efficiencies include the coupling of the modes into the optical fibers, the filter efficiency, and the detection efficiency of the photon counters, which is around 45 % in our case.

5.2.2 Characterization

Thanks to the experimental setup described above, we characterize the DLCZ building block by measuring the two crucial parameters introduced in section 5.1: the conditional retrieval efficiency, q_c, and the normalized cross-correlation function, g_{12}.

5.2.2.1 Dependence with the excitation probability

We first study the behavior of these two parameters as a function of the probability p_1 of detecting a photon in field 1, which is proportional to the excitation probability $\chi = \eta_1 \, p_1$, where η_1 is the detection efficiency for a photon in field 1. In practice we change the write power from 50 nW to 80 µW, the probability of excitation per write photon being approximately 6×10^{-9} in our experiment. Figure 5.3 shows our experimental results as a function of p_1. The left panel gives the evolution of the normalized cross-correlation function g_{12}, which globally decreases when the excitation probability increases. However, all the values are above the classical limit of 2, and the highest value is $g_{12} = 165$, confirming the strong quantum character of the photon pairs. A saturation is observed at very low p_1, because of the background noise, almost equally due to dark counts of the single-photon counters and to leakage of the write and read pulses.

As it has been underlined in chapter 1, the filtering of the classical coupling fields is crucial when operating at the single-photon level. Here, the write and read pulses are filtered spatially, in polarization, and also in frequency. First, an angle of 2.5° is set between the two paths to enable spatial filtering, as discussed in section 2.1.3. Secondly, the horizontal polarization of the write field is orthogonal to the one of the field 1, which is vertically polarized (see figure 5.2). Similarly, the vertically polarized read field is orthogonal to the horizontally polarized field 2. A Glan cube is placed only on the read path before the chamber, to well-defined the read polarization, but not after to avoid loss due to a Glan cube on the field 2 path. Thus, standard polarization beam splitters (PBS) are used here to filter in polarization the coupling fields. Finally, the write pulse is filtered in frequency from the field 1 detection. Indeed, the field 1 is frequency filtered by an atomic filter, where all the atoms are pumped into the $|F = 4\rangle$ state. Hence, the write field is absorbed by this setup. No frequency filtering is realized here for the read pulse.

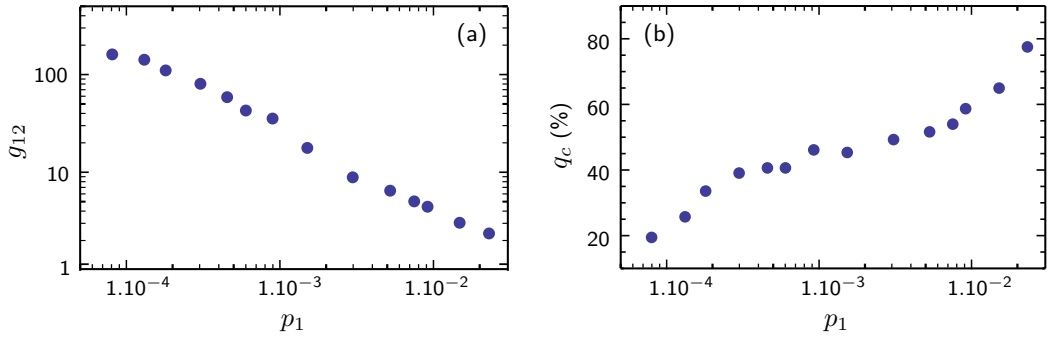

FIGURE 5.3 : DLCZ building block characterization. (a) Normalized correlation function g_{12} and (b) conditional retrieval efficiency q_c as a function of the probability p_1 to detect a photon in field 1. For these data, $d_0 = 30$, $\Delta = -10$ MHz, and $P_r = 90$ μW. Error bars are smaller than the symbol size.

However, during the second step, the homodyne detection will filter in frequency the read field.

On figure 5.3(b) the conditional retrieval efficiency q_c is displayed as a function of the excitation probability. We access to q_c from the conditional probability p_c of detecting a photon in field 2 given a field 1 event, corrected for the detection losses of field 2, $\eta_2 = 0.3$. Three different regimes can be observed on this plot. For high excitation probability, q_c increases with p_1 because of multiple excitations that scale with the write power. For lower excitation probabilities, a plateau is observed, q_c staying constant. This corresponds to the single-excitation regime, where the probability for multi-excitation is low. Finally, for very low values of p_1, the conditional retrieval efficiency decreases. Indeed, because p_1 as well as p_2 become close to the background noise, false field 1 events induced by the noise are appearing. Our region of interest is the single-photon regime, where we obtain a retrieval efficiency q_c of 45 ± 1 %, corresponding to $p_c = 13.5 \pm 0.3$ %. In this regime, for $P_w = 900$ nW, the normalized correlation function is 40 ± 1.

Optimizing the coupling beams In contrast with the dynamic EIT protocol, two different beams are used to "write" and "read" the collective excitation. The optimization is therefore easier.

- Write field. The power of the write beam plays a crucial role for the q_c and g_{12} parameters, as just seen previously. The excitation probability $\chi \propto p_1$ scales linearly with P_w, which should be adjusted to work in the single-photon regime. In our case, we find $P_w \sim 1$ μW. The duration and the shape of the write pulse must be similar to the ones of the first photon. The first photon pulse being close to a Gaussian with a width around 50 ns, we set the write pulse as a Gaussian with a width of 100 ns.
- Read field. The reading process here is close to the retrieval process in an EIT-based memory, but in a backward configuration, i.e. the the reading control beam is counter-propagative with the writing control beam. Thus, we want to open a large transparency window for the field 2 to avoid any absorption from the medium. Hence, a relatively high power is set for the read beam, and a saturation is observed around 100 μW. The duration of the read pulse is not very critical in our case, and set around 150 ns.

5.2.2.2 Dependence with the optical depth

In a second step the dependence of the retrieval efficiency with the optical depth is investigated. For this purpose we choose a write power of 0.6 μW to be in the single-excitation regime identified above.

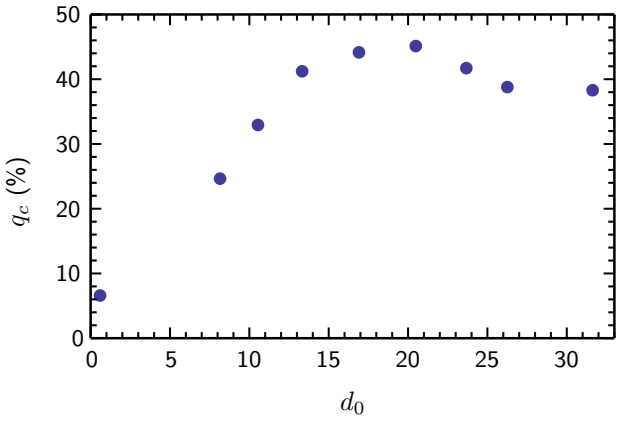

FIGURE 5.4 : Dependence of q_c with the optical depth. The conditional retrieval efficiency is shown as a function of the optical depth d_0. For this measurement, $\Delta = -$ 20 MHz, $P_w = 0.6$ μW and $P_r = 100$ μW. Error bars are smaller than the symbol size.

Figure 5.4 gives the experimental curve for q_c as a function of d_0, for optical depths between 0.6 and 32. We clearly see that the retrieval efficiency strongly increases with d_0 as expected, confirming that the retrieval process is enhanced for large optical depth. However, for $d_0 > 20$, q_c starts decreasing, meaning that unwanted processes, such as residual absorption, become stronger than the collective effects when the optical depth increases. We identify the optimum value of optical depth, the best value of q_c being obtained for an optical depth of 20. Further investigations in this direction must be conducted for a better understanding of the reasons causing this decrease in efficiency at high optical depth. Indeed this work would be now very important to take advantage of the large optical depths that we are able to obtain.

Given these results, the next step consists in characterizing the retrieved state, not only by photon counting, as commonly done, but by full quantum state tomography via homodyne detection.

5.3 Tomography of the retrieved single-photon state

Quantum state tomography enables to reconstruct the density matrix of the heralded single-photon emitted by the atomic ensemble. The method involves the measurement of marginal probabilities by high-efficiency homodyne detection, and the reconstruction of the density matrix via the so-called MaxLik algorithm.

5.3.1 Principle

5.3.1.1 Single-photon state in phase space

We describe here the state of a perfect single-photon in the phase space, i.e. in terms of quadrature operators. The latter are defined as

$$\begin{cases} \hat{x} = & \dfrac{\hat{a}^\dagger + \hat{a}}{\sqrt{2}} \\ \hat{p} = & i\,\dfrac{\hat{a}^\dagger - \hat{a}}{\sqrt{2}} \end{cases}, \tag{5.10}$$

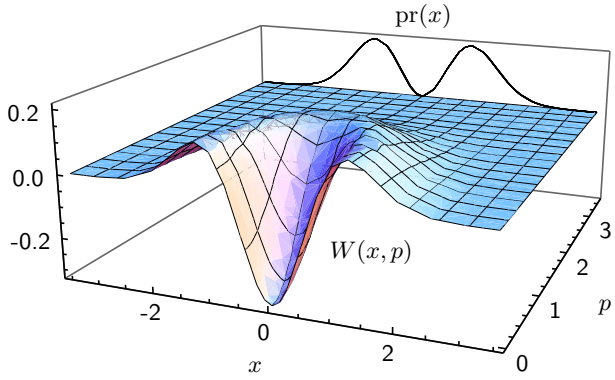

FIGURE 5.5 : The Wigner function $W(x,p)$ and the corresponding probability distribution $\mathrm{pr}(x)$ for a single-photon state.

where $\hat{a}^\dagger$ and $\hat{a}$ are respectively the creation and annihilation operators, with the canonical commutation relation

$$[\hat{x},\hat{p}] = 1\,, \tag{5.11}$$

with $\hbar = 1$. The x-representation of the wave function for a Fock state $|n\rangle$, which is phase independent, is expressed as [Leonhardt, 1997]

$$\Psi_n(x) = \frac{H_n(x)}{\sqrt{2^n n!\sqrt{\pi}}}\, e^{-x^2/2}\,, \tag{5.12}$$

where $H_n(x)$ are the Hermite polynomials. The wave function of the single-photon state is therefore given by

$$\Psi_1(x) = \sqrt{\frac{2}{\sqrt{\pi}}}\, x\, e^{-x^2/2}\,. \tag{5.13}$$

We now introduce the Wigner function, which enables to fully characterize a quantum state of light in phase space (x,p). The Wigner function is a quasi-probability distribution and the marginal distribution $\mathrm{pr}(x,\theta)$, as measured by an homodyne detection, for the quadrature $\hat{x}_\theta$ can be calculated as

$$\mathrm{pr}(x,\theta) = \int_{-\infty}^{+\infty} W(x\cos\theta + p\sin\theta, x\sin\theta - p\cos\theta)\, dp\,. \tag{5.14}$$

The Wigner's formula [Wigner, 1932], which relies the Wigner function and the density matrix can be demonstrated non-trivially, and can be written as

$$W(x,p) = \frac{1}{\pi}\int_{-\infty}^{+\infty} e^{2ipx'}\,\langle x - x'|\hat{\rho}|x + x'\rangle\, dx'\,. \tag{5.15}$$

In order to access to the Wigner function of the single-photon, we inject the wave function given in equation 5.13 in the Wigner formula, and we find

$$W_1(x,p) = \frac{1}{\pi}\left[2\left(x^2+p^2\right) - 1\right] e^{-(x^2+p^2)}\,. \tag{5.16}$$

We notice here that the single-photon state is symmetric by rotation around the origin, and in consequence, the probability distribution remains the same along any rotated quadrature. Figure 5.5 displays this Wigner function, as well as the corresponding probability distribution $\mathrm{pr}(x)$. First, the single-photon

state exhibits non-gaussian statistics, as opposed to coherent, squeezed or thermal states, which form a large range of states of light. Moreover, whereas the marginal distribution is always positive, the Wigner function exhibits negative values around the origin, which is a strong signature of non-classicality.

5.3.1.2 Quantum state tomography

The retrieval state is measured by homodyne detection. The field 2 is mixed on a 50/50 beam splitter with a strong classical field, called the local oscillator, and detected by two high efficiency photodiodes. This measurement leads to the projection of the signal state on the rotated quadrature $\hat{x}_\theta = \cos\theta\,\hat{x} + \sin\theta\,\hat{p}$, where θ corresponds to the relative phase between the local oscillator and the signal field. The principle of the homodyne detection is summarized in appendix G. In our case, since the single-photon state is phase independent, the homodyne measurement is phase averaged. Then, we reconstruct the density matrix ρ of the signal state via the iterative maximum likelihood algorithm (MaxLik). This method has been identified as a very efficient method in quantum optics and is now widely used [Lvovsky, 2004].

Let us quickly describe the iterative maximum likelihood algorithm. Here we assume that the experimental measurement is realized with infinitely small bins, and returns a data set $\{x_i, \theta_i\}$. The MaxLik algorithm aims to find the density matrix $\hat{\rho}$ that maximize the log-likelihood function,

$$\log \mathcal{L}(\hat{\rho}) = \sum_i \log(\mathrm{pr}(x_i, \theta_i))\,, \tag{5.17}$$

where the probability $\mathrm{pr}(x, \theta)$ of detecting the quadrature value x at the angle θ can be defined as

$$\mathrm{pr}(x, \theta) = \mathrm{Tr}\left[\hat{\Pi}(x, \theta), \hat{\rho}\right]\,, \tag{5.18}$$

with $\hat{\Pi}(x, \theta) = |x, \theta\rangle\langle x, \theta|$ the projection operator onto the quadrature eigenstate. In the Fock basis, the projection operator is expressed as

$$\hat{\Pi}_{m,n}(x, \theta) = \langle m|\hat{\Pi}(x, \theta)|n\rangle = \langle m|x, \theta\rangle\langle x, \theta|n\rangle\,, \tag{5.19}$$

where the overlap between the photon number and the rotated quadrature eigenstates is expressed similarly as in equation 5.12

$$\langle x, \theta|n\rangle = e^{i\theta n}\,\Psi_n(x) = e^{i\theta n}\frac{H_n(x)}{\sqrt{2^n n!\sqrt{\pi}}}e^{-x^2/2}\,. \tag{5.20}$$

We now introduce the operator

$$\hat{R}(\hat{\rho}) = \sum_i \frac{\hat{\Pi}(x_i, \theta_i)}{\mathrm{pr}(x_i, \theta_i)}\,, \tag{5.21}$$

which verifies the relation

$$\hat{R}(\hat{\rho})\,\hat{\rho}\,\hat{R}(\hat{\rho}) \propto \hat{\rho}\,. \tag{5.22}$$

Therefore, starting from an initial density matrix, for instance $\hat{\rho}^{(0)} = \mathcal{N}[\hat{1}]$, it is possible to apply the following iteration

$$\hat{\rho}^{(k+1)} = \mathcal{N}\left[\hat{R}(\hat{\rho}^{(k)})\,\hat{\rho}^{(k)}\,\hat{R}(\hat{\rho}^{(k)})\right]\,, \tag{5.23}$$

where $\mathcal{N}$ denotes normalization to a unitary trace. Thus, after several iteration, the algorithm returns the likeliest density matrix given the experimental data. Finally, the Wigner function can be calculated from the Wigner formula (equation 5.16).

In practice, because the Hilbert space corresponding to the Fock basis is infinite, a truncation is first realized. For a single-photon state with small higher photon number components, a truncation around $n = 5$ is well adapted. Moreover, because of the symmetry of the single-photon Wigner function, the marginal distribution can be averaged over θ,

$$\mathrm{pr}_{av}(x) = \langle \mathrm{pr}(x,\theta) \rangle_\theta \ , \tag{5.24}$$

before its introduction in the MaxLik algorithm. In practice, a random phase value is attributed to each data x_i.

Because of losses, the experimentally measured state, when neglecting the low two-photon component, is of the form

$$\rho = (1-\eta)\,|0\rangle\langle 0| + \eta\,|1\rangle\langle 1| \ , \tag{5.25}$$

where η is the overall field 2 efficiency, from the generation to the detection. In our case it corresponds to $q_c\,\eta_d^2\,V^2$ where η_d is the quantum efficiency of the photodiodes, V is the visibility between the field 2 and the local oscillator and q_c is the conditional retrieval efficiency of the DLCZ protocol. However, in order to observe the negativity of the Wigner function, the following condition should be satisfied

$$q_c\,\eta_d^2\,V^2 \geq 0.5\,. \tag{5.26}$$

In our case, a value of only 45 % for the retrieval probability is observed experimentally. Thus, in these conditions, the negativity of the Wigner function can not be demonstrated so far, but the non-gaussian character of the retrieval state can be shown. Works for increasing the retrieval efficiency, in particular about better exploiting the optical depth, are currently in progress.

In this section, we have seen how to reconstruct the density matrix and the Wigner function of a quantum state of light, and in particular of a single-photon state, via homodyne measurement. In the following, we describe the experimental setup that enables to perform the quantum state tomography of the heralded single-photon emitted by the atomic ensemble via the DLCZ protocol.

5.3.2 Experiment

In this section the experimental setup allowing the homodyne measurement of the heralded single-photon state retrieved by the atomic ensemble is presented. Then, we discuss the temporal mode of the photon, which is required to access to the value quadrature.

5.3.2.1 Experimental setup

Figure 5.6 shows the optical layout for the homodyne measurement of the heralded single-photon. The DLCZ building block is implemented as in section 5.2 and we highlight here the detection part. Instead of being detected by single-photon counters, the field 2 photon is mixed on a 50/50 beam splitter with the local oscillator, which comes from the Ti:Sapphire laser, locked on resonance with the $|F = 4\rangle \rightarrow |F' = 4\rangle$ transition. The local oscillator is continuous and has a power of 4 mW. Because we assume a phase independent state, no control of the local oscillator phase is required in our case, and we let the phase randomly varying. The optical transmission from the vacuum chamber to before the homodyne detection is 92 % for the field 2, while it is equal to 97 % in the homodyne detection part. The matching between the field 2 and the local oscillator modes results in a visibility of typically 94 %. Each output is measured by a photodiode (Hamamatsu, S5971) having a quantum efficiency

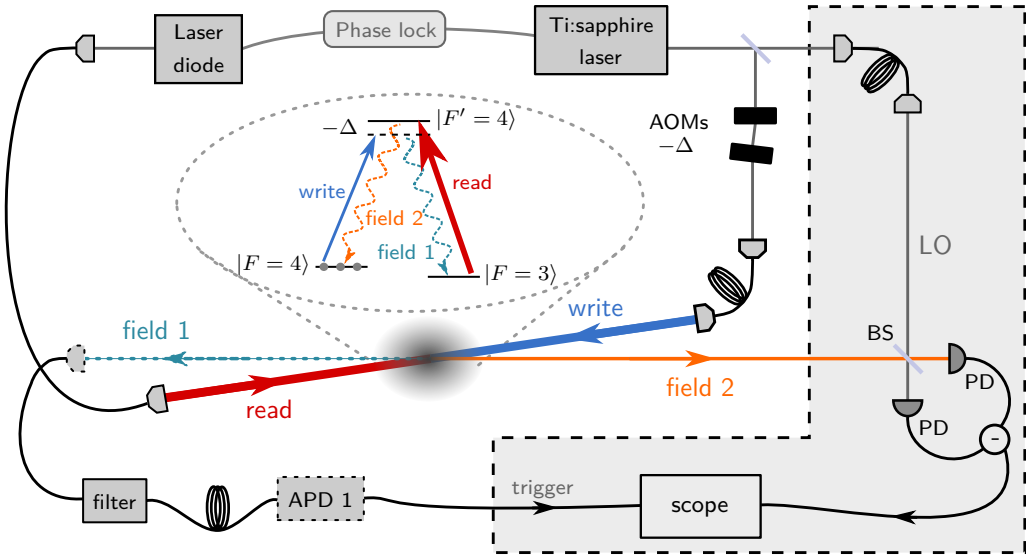

FIGURE 5.6 : Optical layout for homodyne measurement of single photons generated by the atomic ensemble via the DLCZ protocol. The field 2 is mixed on a 50/50 beam splitter with a strong local oscillator (LO) coming from the Ti:Sapphire laser. Both beam splitter outputs are detected by photodiodes (PD), and the currents are subtracted, amplified and finally sent to a scope. The recording of the homodyne detection signal is triggered by the previous detection of a field 1 photon on the single-photon detector APD 1.

$\eta_d = 92$ %. The overall detection efficiency for the field 2 is therefore 0.67.

The photocurrents of both detectors are directly subtracted and then amplified. The overall bandwidth is about 100 MHz. More experimental details about the implemented homodyne detection can be found in appendix G. The output of the homodyne detection is finally recorded and analyzed by a scope (Lecroy, Wavepro 7300A), which is triggered by the APD 1 output. Thus, the detection of a photon in field 1 leads to the recording of a 200 ns segment of the homodyne detection subtracted photocurrent within the same DLCZ trial. The time of arrival of the photon in field 2 has been observed previously on the single-photon counters. The acquisition of the homodyne output is then gated during the read process.

Before reconstructing the density matrix thanks to the homodyne measurement, we take a look at the temporal mode of the retrieved state. Indeed, the local oscillator being continuous, post processing is required in order to extract the temporal mode in which the photon is emitted.

5.3.2.2 Temporal mode

Thanks to the large bandwidth of the homodyne detection, the temporal shape of the heralded single-photon can be observed. Figure 5.7(a) represents the variance of the homodyne detection output as a function of time. The homodyne measurement is actually proportional to the electric field of the signal to measure, so the variance is proportional to the intensity. The data are fitted by a Gaussian distribution, $f(t) = A\exp(-t^2/(2\,\sigma)) + B$, with a standard deviation $\sigma = 27.4$ ns, which corresponds to a full width at half maximum (FWHM) of 64 ns. For comparison, the coincidence events on APDs are displayed on figure 5.7(b) as a function of time. The event number from the APD also scales with the intensity of the signal field. Despite of the 10 ns resolution of the acquisition card that records the APDs output, we also fit the data by a Gaussian distribution with a standard deviation of 23.4 ns,

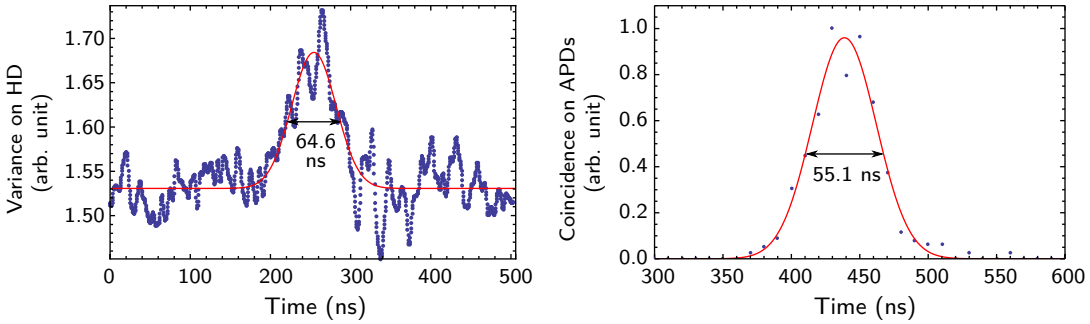

FIGURE 5.7 : Temporal mode of the single-photon measured via (a) the variance of the homodyne detection output, and (b) the coincidence between events detected on APD 1 and APD 2, as a function of the time. Experimental data (blue dots) are fitted by a gaussian distribution (red line). The full widths at half maximum resulting from these fits are displayed on the graphs, and are equal to 64.6 ns and 55.1 ns. The variance corresponds to an average over 5000 measurements.

corresponding to a FWHM of 55 ns. The standard deviation σ_e of the electric field is related to the standard deviation σ_i of the intensity, obtained by the variance of the homodyne detection output or by the photon number of the APD by

$$\sigma_e = \sqrt{2}\,\sigma_i\,. \tag{5.27}$$

These results are in agreement to the expected value of about 30 ns, the lifetime of the excited level $6^2P_{3/2}$ being 32.8 ns.

Accessing the quadrature values Determining the temporal mode of the heralded photon is crucial in order to access to the quadrature value x_i, which results from the projection by the homodyne detection of the state to measure. Thus, the output signal $x_i(t)$ of the i$^{\text{th}}$ measurement by the homodyne detection is multiplied by the temporal mode $f(t)$, and integrated, as

$$X_i = \int_0^T f(t)\,x_i(t)\,dt\,. \tag{5.28}$$

Then, the quadrature value is normalized by the vacuum variance V_0:

$$x_i = \frac{X_i}{V_0}\,. \tag{5.29}$$

A large number of measurements are recorded in order to obtain a large data set $\{x_i\}$. The histogram of this data set directly gives the experimental marginal probability $\mathrm{pr}(x_i)$.

In the following, preliminary experimental results are presented, from the marginal probability to the reconstructed Wigner function.

5.3.3 Preliminary results

Here are displayed our current results about the tomography of the retrieved state from our ensemble of cold atom via the DLCZ protocol.

Figure 5.8 shows the marginal probabilities, corresponding to the histogram of values obtained from a large number of quadrature measurements via homodyne detection. The blue area represents the reconstructed marginal probability for the vacuum, i.e. when no retrieved photon comes to the

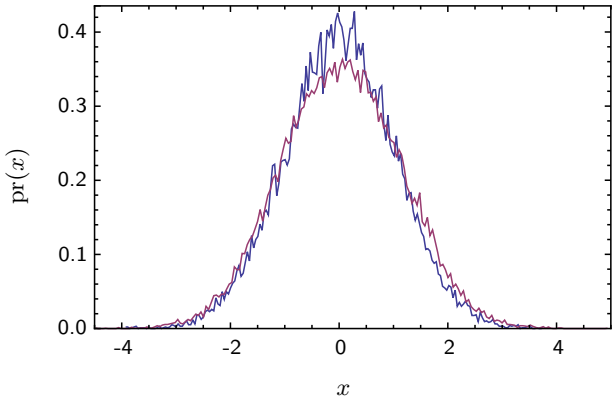

FIGURE 5.8 : Marginal probabilities $\mathrm{pr}(x)$ for the vacuum (blue area), and for the retrieved state (purple area).

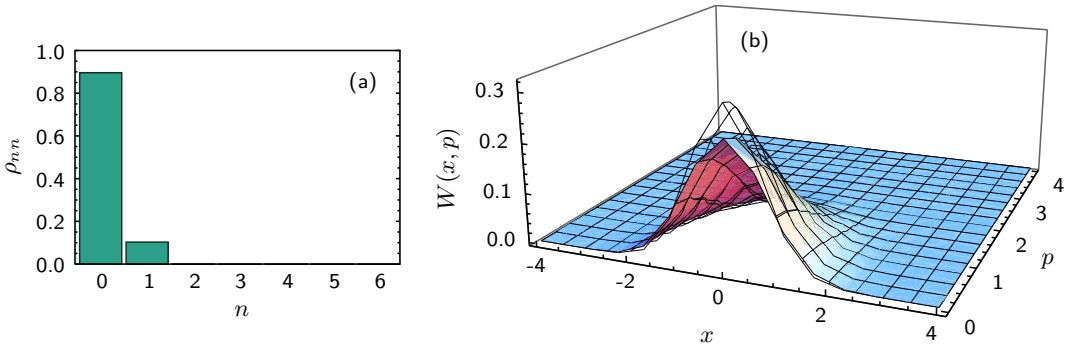

FIGURE 5.9 : Tomography of the retrieved state. (a) Diagonal elements of the reconstructed density matrix and (b) associated Wigner function.

homodyne detection, while the purple area corresponds to the retrieved state. Even though no dip is observed in the marginal probability of the retrieved state, the behavior starts to become different from the Gaussian distribution of the vacuum. The values around the origin, on the top of the distribution, are 10 % smaller than for the vacuum.

The complete tomography of the retrieved state is shown on figure 5.9. The reconstructed density matrix, displayed on panel (a), exhibits a large contribution of vacuum, $\rho_{00} = 89.6$ %, and a small component of single-photon, $\rho_{11} = 10.3$ %. The two-photon component is well-suppressed, with $\rho_{22} = 2.3 \times 10^{-4}$. By neglecting the two-photon component, the corresponding Wigner function is given by

$$W(x,p) = \rho_{00} W_0(x,p) + \rho_{11} W_1(x,p)\,. \tag{5.30}$$

The Wigner function of the retrieved state is plot on panel (b), together with the Wigner function of the vacuum (transparent black meshed curve). As seen with the marginal probability, we start observing the non-gaussianity of the retrieved state. Corrected for detection losses, the single-photon component reaches $\rho_{11}^{corrected} = 16$ %. We emphasize again that these results correspond to very preliminary results and improvements are ongoing.

These results are actually well below what we can expect currently in our system. Indeed, the single-photon contribution should be close to the measured retrieval probability $q_c = 45$ %, multiplied by the overall detection efficiency, here 67 %. Thus, a value around 0.3 for ρ_{11} should be observable in our experiment, but only 10 % is observed, meaning that additional losses may occur, or that the

mode that we detect on the photon counter is different than the one that we observed on the homodyne detection. The latter can come from the fact that the write and read beams are not plane waves in the atomic ensemble, leading to a bad definition of the phase-matching condition. Larger write and read beams would therefore help to better define the spatial mode of the retrieved state, and this investigation is currently conducted in our system. To go further, higher optical depth with a control of the effect coming from the multilevel structure, as well as cooling the atoms down to lower temperature via Sisyphus cooling will enable us to obtain higher retrieval efficiencies and longer storage times. We note that in the past few weeks, results of a similar experiment but operating in cavity setting have been reported on arXiv by the group of P. Grangier [Bimbard et al., 2013]. In contrast, our study focus on a "free-space" ensemble.

Conclusion

What we have seen:

- We have implemented the DLCZ building block in our ensemble of cold atoms, and we have characterized it by the retrieval efficiency and the normalized correlation function. Typical values of respectively 45 % and 40 are obtained, for an optimal optical depth of 25.
- An homodyne detection has been set up, in order to enable the reconstruction of the density matrix of the heralded single-photon via the iterative maximum likelihood algorithm.
- The complete quantum tomography of the photonic state generated by the atomic ensemble definitely revels a single-photon component, but smaller than expected. Work is still in progress to improve these preliminary results.

In consequence:

- With higher retrieval efficiency, our system will in principle allow the demonstration of the quantum character of a heralded single-photon generated by an atomic ensemble, via its complete reconstruction and negative Wigner function.
- The optical depth plays a crucial role in the DLCZ protocol. Further investigation will enable us to know how to take advantage of the large optical depths that we are able to produce. Moreover, the temporal mode of the retrieved photon must depend on the optical depth [Mendes et al., 2013], and this study will be conducted in our system.
- This work opens the way towards the tomography of a complete zoology of quantum state, as the two-photon state, $|2\rangle$, or $|3\rangle$, or to coherent superposition, such as $|0\rangle + |1\rangle$ or $|0\rangle + |2\rangle$. More generally, with further works on the retrieval efficiency, this opens the path to the quantum engineering of collective excitation that can be efficiently transferred to light.

Conclusion

In this thesis, quantum memory protocols based on collective excitations, the EIT-based memory and the DLCZ scheme, have been implemented in an ensemble of cold cesium atoms. Cold atomic ensembles are indeed good candidates to operate at the single-photon level with off-axis configuration. We first developed an atomic ensemble based on a pulse magneto-optical trap for cesium atoms with a relatively large optical depth of 40. The residual magnetic field is canceled down to few mG via microwave spectroscopy, which is crucial to avoid decoherence due to inhomogeneous broadening.

As a first experiment, we studied the electromagnetically induced transparency features in our system, via the experimental test of the criterion proposed by the authors of [Anisimov et al., 2011] for the discrimination between the EIT and the Autler-Townes splitting models. Identifying the presence of coherent effects is indeed crucial for optically controlled light slowing, or optical quantum storage. We tested and analyzed in details the transition between the EIT and ATS models, showing that the proposed criterion gives consistent conclusion for discerning between the two phenomena and is experimentally suitable. Moreover, the witness is very sensitive to the specific medium properties. The multilevel structure and residual inhomogeneous broadening had to be considered to explain the difference between the experimental behavior and the simple three-level model. Thus, the proposed criterion potentially provides a characterization tool for complex systems.

Then, an EIT-based quantum memory for orbital angular momentum of light was realized. First, we demonstrated that the memory device preserves the handedness of twisted photons, i.e. the helical wavefront structure of first-order Laguerre-Gaussian modes in the single-photon regime. With a current decay time of 15 µs, the storage time will be improved by cooling the atoms down to lower temperatures via Sisyphus cooling or even further via dipole trap techniques. Second, the storage of OAM encoded qubits was performed, along with the quantum tomography of the retrieved qubit states. The obtained fidelities beat the best classically achievable ones, demonstrating therefore the quantum character of the implemented optical memory. This experiment provides the first demonstration of quantum memory for OAM encoded qubits, opening the way towards multimode quantum storage involving higher OAM numbers. This constitutes an important tool for the development of quantum communication protocols based on the unbounded OAM degree of freedom with high-dimensional potential.

Finally, we have implemented the DLCZ building block in our ensemble of cold atoms. A characterization of the system in the photon counting regime has been performed, highlighting the strong correlations between the two generated photons. Preliminary results about the state tomography of the heralded single-photon via homodyne detection have been reported. Higher retrieval efficiencies will allow us to demonstrate the quantum character of the retrieved state. Quantum tomography of the heralded single-photon generated by DLCZ in an atomic ensemble is a step towards the quantum engineering of collective excitations that can be transferred to light. Since the optical depth is a crucial parameter, a better understanding of the effects occurring in our multilevel system will give clues to

take advantage of the large optical depths that we are able to produce. Moreover, the optical depth must influence the temporal mode of the retrieved photon, this study will be conducted in our system.

Appendix A

Phase-frequency locking

The phase-frequency locking aims at setting the frequency difference between the Ti:Sapphire laser and an extended cavity laser diode at the hyperfine transition frequency of cesium atom, $\omega_{hf} = 9.192631770$ GHz, or around if the two-photon detuning needs to be scanned. The phase is also stabilized between the two lasers, which is important to observe EIT. This phase-frequency locking has been developed by Jérémie Ortalo and Sidney Burks [Burks, 2010], but has been improved since then, and I give here an overview of the current version.

A.1 Lasers

The first laser is a titanium-sapphire laser (Spectra-Physics Matisse) that is locked on resonance with the $|F = 4\rangle \rightarrow |F' = 4\rangle$ transition. First a fast stabilization is performed by locking the laser cavity on an ultra-stable reference cavity [Burks, 2010], and then a slow stabilization consists in locking the reference cavity on the $|F = 4\rangle \rightarrow |F' = 4\rangle$ transition via saturated absorption spectroscopy. For this purpose, the length of the reference cavity is modulated around 30 kHz and the error signal is obtained via demodulation of the saturated absorption signal by a lock-in amplifier. The light coming from this laser is temporally shaped into pulses by a pair of two acousto-optic modulators (AOM) diffracting both at the same frequency, one in the $+1$, the other one in the -1 order, in order to keep unchanged the laser frequency.

The second laser is an extended-cavity laser diode that was at first a Littrow type with a diffraction grating to select the wavelength and then has been replaced during this PhD by an interference-filter one (Radiant Dyes Laser NarrowDiode via Laserlabs), which is more stable. The change took place in November 2012, so before the results about the complete tomography of orbital angular momentum encoded qubits. The laser diode is temporally shaped by an AOM at 200 MHz, and the first order is used for the memory experiment. Thus, to set the laser diode frequency on resonance with the $|F = 3\rangle \rightarrow |F' = 4\rangle$ transition, the lock point has to be equal to 9.192631770 - 0.2 = 8.992361770 GHz.

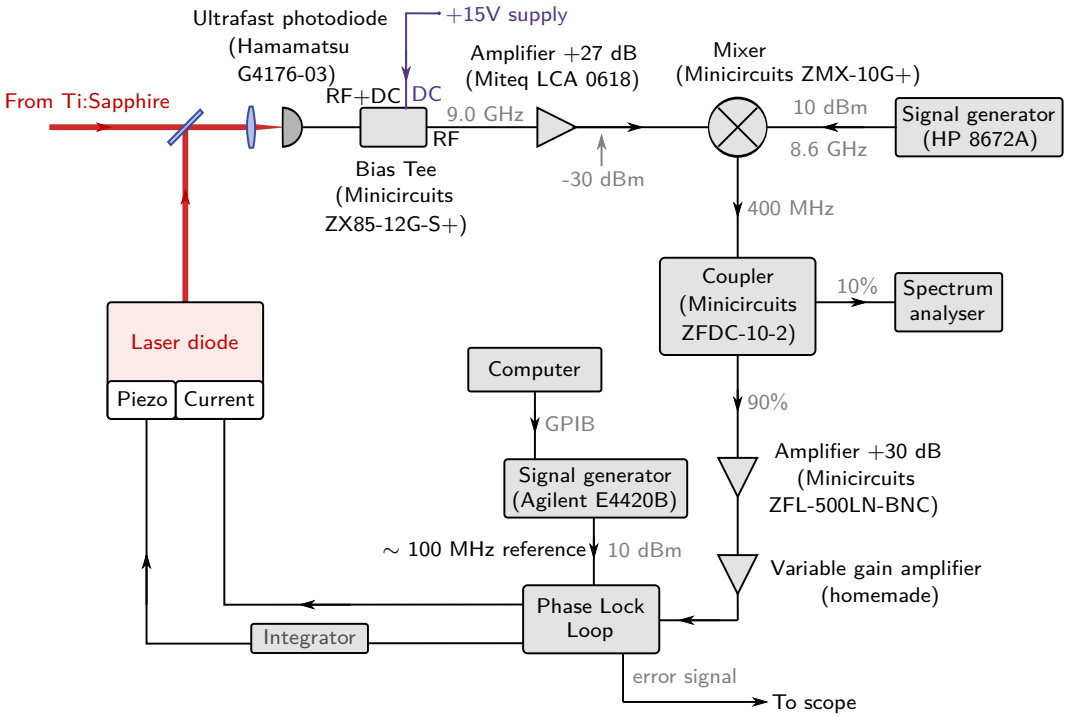

FIGURE A.1 : Setup of the phase-frequency locking. The beating between the two lasers, around 9 GHz, is detected by a fast photodiode, then mixed with a signal around 8.6 GHz. The resulting 400 MHz signal is amplified and analyzed by a phase lock loop system, where a 100 MHz stable signal is used as a reference. Finally, the error signal is directly sent to the current of the laser diode, while another part is integrated and acts on the piezoelectric transducer of the laser cavity.

A.2 Operation

Figure A.1 shows the setup of the phase-frequency locking. A small amount of light of the extended-cavity laser diode is mixed on a non-polarizing beam splitter with a beam coming from the Ti:Sapphire laser via optical fiber. They are focused on a very fast photodiode with a time response of 30 ps (Hamamatsu G4176-03) which is supplied by a + 15 V source via a bias tee. Then the electronic beating signal pass through a + 27 dB amplifier and is mixed with a 8.592632 GHz signal (HP 8672A). This results to a 400 MHz signal which is easier to handle than a high frequency signal.

A small part of the 400 MHz signal is sent to a spectrum analyzer for monitoring (the signal must be at least 20 dB above the noise), while the rest is amplified and sent to the phase-lock loop, which is the main part of the locking. This electronic box was realized at the LKB and the principle is well described in [Burks, 2010]. It consists first in a frequency divider by 4 and then a phase-frequency detector which compares the beating signal to a 100 MHz reference generated by a very stable synthesizer (Agilent E4420B). The set point of the locking can be modified by changing the frequency of the signal generator output. Moreover the synthesizer can be controlled by the Labview program via GPIB in order to operate a frequency scan of the laser diode for instance.

Finally the feedback occurs in two steps. First, the error signal is directly sent towards the current of the diode for a very fast response. With the new diode, the error signal passes through the current supply with a gain of 1 A/mV, without loss in terms of bandwidth. Secondly, an integrated error signal part enables a slow drift compensation by acting on the piezoelectric transducer controlling the length

of the external laser diode cavity. Thus, the laser diode is locked on phase and frequency with the Ti:Sapphire laser at or around the hyperfine frequency $\omega_{hf} = 9.192631770$ GHz.

Figure A.2 shows the beating between the two lasers, when they are locked together. Here, the resolution does not enable us to observe the width of the peak, which has been measured around 1 Hz. However, sidebands can be remarked, approximately 800 kHz away from the central peak, this frequency corresponding to the bandwidth of the locking.

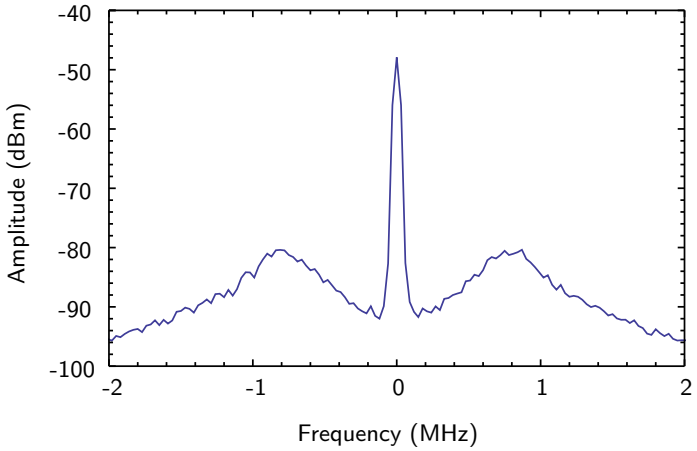

FIGURE A.2 : Beating observed at the spectrum analyzer. Sidebands are observed at 800 kHz around the central peak.

Appendix B

Labview managed spectroscopy

This appendix describes the device control part, as well as the data acquisition and analysis part, that are run by Labview and used for both the microwave spectroscopy and the acquisition of EIT profiles.

B.1 Frequency scans

The Labview program `Host.vi`, which runs on the computer, can operate two different types of frequency scans. The first option is the frequency sweeping of a microwave pulse produced by a signal generator (Rohde & Schwarz, SMB100A) in order to obtain the Zeeman structure spectrum, as presented in chapter 2. The second possibility is to scan the two-photon detuning between the two phase-locked lasers described in appendix A. This scan is obtained by tuning the frequency of the 100 MHz reference generated by a signal generator (Agilent E 4420B), corresponding to changing the set point of the phase-frequency locking. This second option is used for the EIT study but has been developed initially for a Raman spectroscopy scheme. In both options the signal generators are controlled by the Labview program via GPIB (General Purpose Interface Bus). They perform a sweep by steps, and the user can choose the start and stop frequencies, as well as the number of steps via the front panel shown in figure B.2. The change of frequency occurs once per MOT cycle and is triggered by the process of recording the probe pulse detection signal.

B.2 Absorption measurement

Figure B.1 shows the principle of the Labview managed spectroscopy via the recording of absorption measurements. Light pulses are sent through the atomic ensemble to probe the system. Two pulses are actually needed, one enables us to get a pulse intensity reference I_0 while the other measures the effect of the medium by its intensity I. The aim is to calculate the absorption, $A = -\ln(I_0/I)$. Both probe pulses are detected by a home-made high-gain photodiode whose output is recorded by Labview via an acquisition card (National Instrument, PCI-6110). The probe pulse duration, usually 15 µs, is chosen as short as possible while remaining compatible with the bandwidth of the high-gain photodiode. The acquisition card is triggered by a FPGA signal trigger and the data are transferred to the `Host.vi` Labview program (see figure B.3). Data analysis is made using Labview environment as the following.

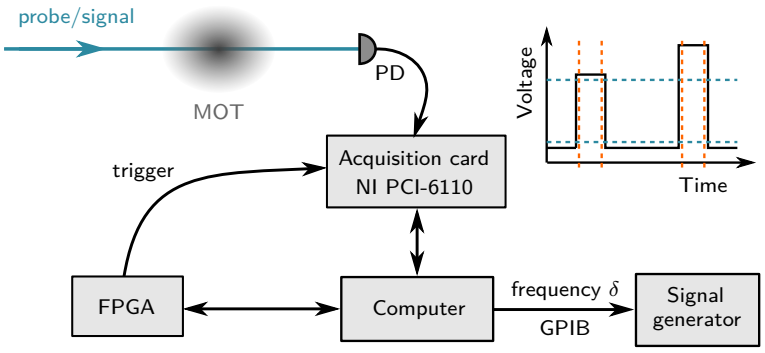

FIGURE B.1 : Principle of Labview managed spectroscopy. Probe or signal pulses are detected by a photodiode, and its output is recorded by an acquisition card and transferred to the computer where it is analyzed with Labview, by setting horizontal or vertical thresholds. The computer communicates also via Labview with the FPGA (Field-programmable gate array), which triggers the acquisition and the shaping of the optical pulses. Finally, the Labview program on the computer commands the frequency detuning δ to a signal generator via GPIB.

Thresholds are set on each measured pulse, a high one, just below the top plateau of the pulse, and a low one, just above the floor noise of the photodiode. Then, averages are done over all the points above the higher threshold and over all the points below the lower threshold. Heights of the probe and reference pulses, respectively I and I_0, are thus given by the differences between the higher and lower means values for each pulse. However this method for measuring the light pulse intensity is not practical in the EIT study case because the absorption of the signal pulse varies drastically and is sometimes very strong. Therefore, vertical bars are set up on each side of pulses, and averaging is performed over the points between the vertical bars. After background noise subtraction we obtain I and I_0. Thus, the probe beam absorption is given by $A = -\ln(I_0/I)$ using one of the methods.

Finally, the calculated value for the absorption is placed in an array with the corresponding frequency value after each MOT cycle. At the end of the scan of the detuning δ, the spectrum is displayed and saved into a text file.

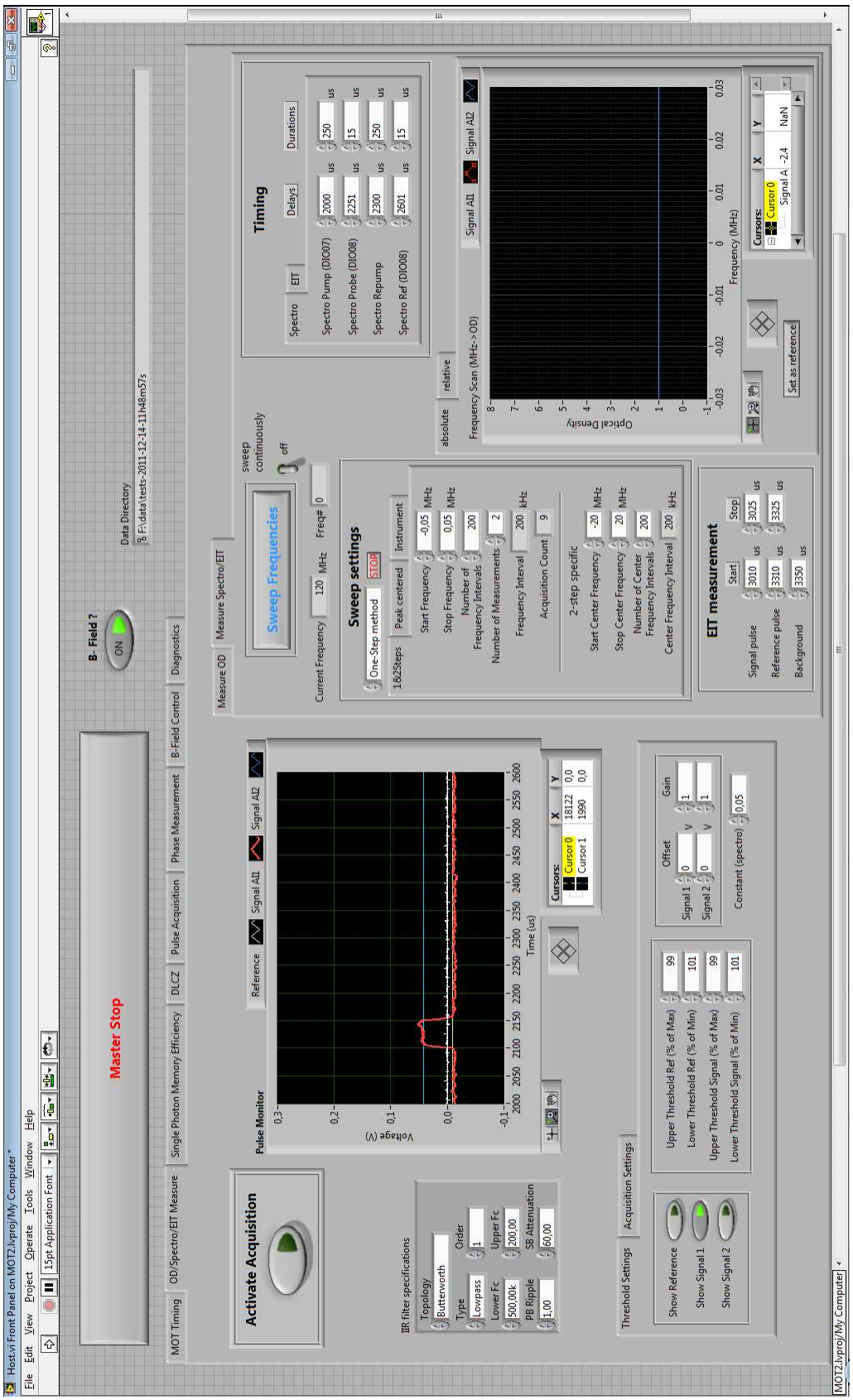

FIGURE B.2 : Front panel, i.e. the user interface, of the `Host.vi` for the spectroscopy.

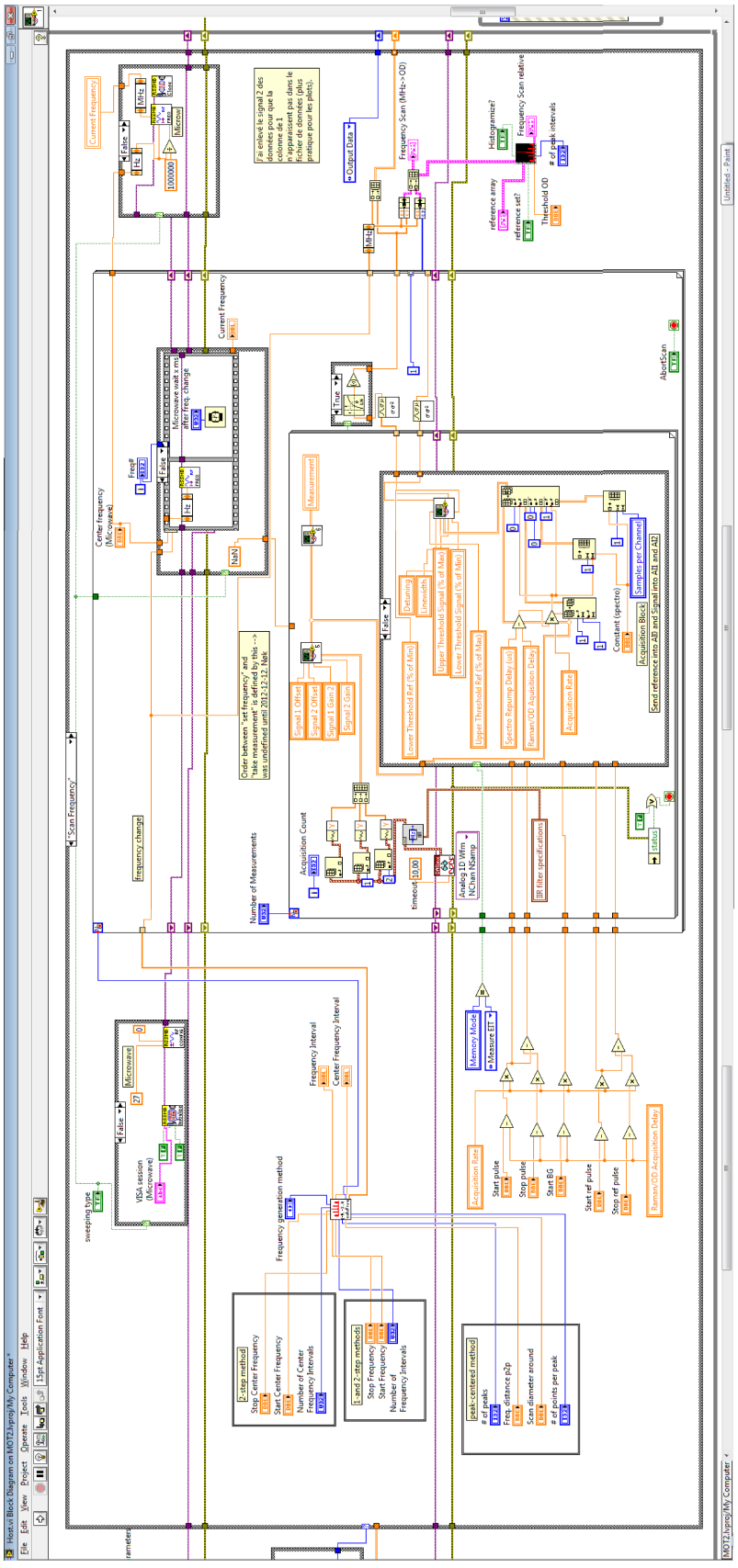

FIGURE B.3 : Part of the block diagram of the `Host.vi` program for the spectroscopy.

Appendix C

Analysis of single-photon detector outputs

In this thesis, several experiments are realized in the single-photon regime. Avalanche photodiodes (APD) are indeed used to detect the different optical pulses involved in the protocols. Because the detection setup sometimes consists in two parts, we dispose of two APDs. Our single-photon counters (Perkin Elmer, SPCM-AQR-14-FC) have a quantum efficiency of approximately 45 % at 852 nm, a dead time of 30 ns, and a dark count rate between 50 and 100 Hz. An event on the detector leads to an output signal with a decreasing exponential shape, with a typical duration of 30 ns. The detectors would be damaged by the strong illumination of the atomic ensemble during the MOT build-up stage. Thus, they are gated by the FPGA to be on only during the memory sequence.

The APD outputs are recorded by an acquisition card (National Instrument, PCI 5122) at 100 Ms/s, given a time binning of 10 ns, and then analyzed by the `Host.vi` Labview program. The acquisition card is also triggered by the FPGA, and records in once the data for all the trials of a MOT cycle. Usually the memory trials are contained in 1 ms within a MOT cycle. Then, the data are cut into elementary memory sequence. A threshold is set on the analogue signal from the APD in order to digitize it. Using this method, it is important to prevent double counts. Thus, when an event is detected, the program skips the following data during 50 ns, which is slightly longer than the dead time of the detector.

C.1 EIT-based memory experiment

During the EIT-based memory experiment, the goal is to observe the memory histogram as a function of time, and to calculate the memory efficiency.

C.1.1 Histograms

The timing for the EIT-based memory for OAM of light is displayed on figure C.1. The gate for the APDs and the acquisition window starts 2 ms after the extinction of the trapping magnetic field and last 1 ms. During this time, 100 memory trials occur, with a duration of 10 µs. The program sums up progressively the data from all the trials, after each MOT cycle. After a user-defined number of

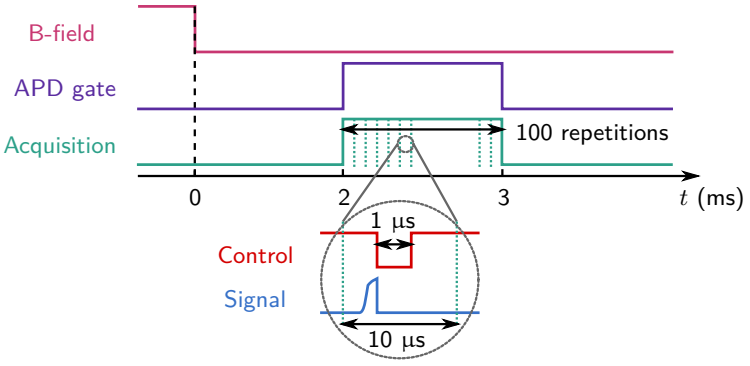

FIGURE C.1 : Timing for the EIT-based memory acquisition. At $t = 2$ ms, the APD gate and the acquisition trigger signal are switched on, for a duration of 1 ms. During this time, 100 trials of the memory protocol occur, each with a duration of 10 µs. The memory trial involves a control field which is off only during the storage time, and a signal pulse which is sent just before the extinction of the control. The stored signal is then retrieved and detected when the control is turned on again.

trials, the acquisition stops and the histograms representing the sum of each APDs output are displayed. The histograms are finally saved in a text file. They enable us to show memory curves, as presented in section 4.1.2 for the storage of twisted photons in the single-photon regime.

C.1.2 Efficiency calculation

The memory efficiency η_m is defined as the number of photons in the retrieval over the number of photons in the input pulse, which is measured without the trapped atoms. Thus, two acquisitions are needed, one without the atomic ensemble, called the reference, and one with the atomic ensemble, the memory acquisition. In the case of EIT-based memory, the detection efficiency does not affect the memory efficiency, because the same losses occur on both the reference and the retrieval. Moreover, it is also very useful to obtain the leakage α_l, defined as the percentage of the number of photons which pass through the atomic ensemble without being stored. Indeed, leakage of the signal is purely loss, and must be minimized.

We dispose of two histograms, the reference one, $N_{ref}(t)$, and the memory one, $N_{mem}(t)$, as shown in figure C.3. The user sets vertical cursors on the histograms to define the initial and final time bin t_i^{ref} and t_f^{ref} for the reference pulse and t_i^{mem} and t_f^{mem} for the memory retrieval pulse. The leakage is then defined by the same timing as the reference, but in the memory acquisition data. The number of events is calculated within the defined pulses for the reference, the retrieval, and the leakage. Background noise is also measured outside of the areas of interest, at a time t_i^{BG}, for a number of time bins equivalent to the reference on the reference acquisition, and to the leakage and the retrieval on the memory acquisition. Subtracting the background noise is important in this context. Since the retrieval is smaller than the reference, it is more sensitive to the presence of background than the reference. Thus, the calculated efficiency would appear higher than what it really is without background noise subtraction. Therefore, the efficiency is calculated as

$$\eta_m = \frac{\sum_{t=t_i^{mem}}^{t_f^{mem}} N_{mem}(t) - \sum_{t=t_i^{BG}}^{t_f^{mem}-t_i^{mem}} N_{mem}(t)}{\sum_{t=t_i^{ref}}^{t_f^{ref}} N_{ref}(t) - \sum_{t=t_i^{BG}}^{t_f^{ref}-t_i^{ref}} N_{ref}(t)}, \tag{C.1}$$

as well as the leakage,

$$\alpha_l = \frac{\sum_{t=t_i^{ref}}^{t_f^{ref}} N_{mem}(t) - \sum_{t=t_i^{BG}}^{t_f^{ref}-t_i^{ref}} N_{mem}(t)}{\sum_{t=t_i^{ref}}^{t_f^{ref}} N_{ref}(t) - \sum_{t=t_i^{BG}}^{t_f^{ref}-t_i^{ref}} N_{ref}(t)}\,, \tag{C.2}$$

This information is given automatically after the acquisition ends, and helps to optimize the efficiency of the memory by changing parameters such as the control power or switching time.

C.1.3 With interferometry

The demonstration of coherence of the OAM encoded qubit stored in our EIT-based memory involves an interferometry technique (section 4.2.1). Here, we want to associate to each memory trial a value of the interferometer phase, so the program does not average over the trials, but gives a timestamp to each one. Actually, because the acquisition time of the picture which gives the interferometer phase is much longer than the MOT cycle duration, we give one timestamp per MOT cycle. The data are written after each MOT cycle into a text file in a JSON (JavaScript Object Notation) format, which derives from the JavaScript scripting language and is an open standard format that uses human-readable text to transmit data objects consisting of attribute–value pairs. The data are analyzed afterwards with the interferometer phase information via Python.

C.2 DLCZ building block experiment

C.2.1 Timing

The timing is similar to the one for the EIT-based memory, and shown on figure C.2. Between $t = 2$ and 3 ms, the APD gate and the acquisition trigger are on. During this time, 1000 trials of 1 µs are performed, which involve a write followed by two read pulse, the second playing the role of a repump.

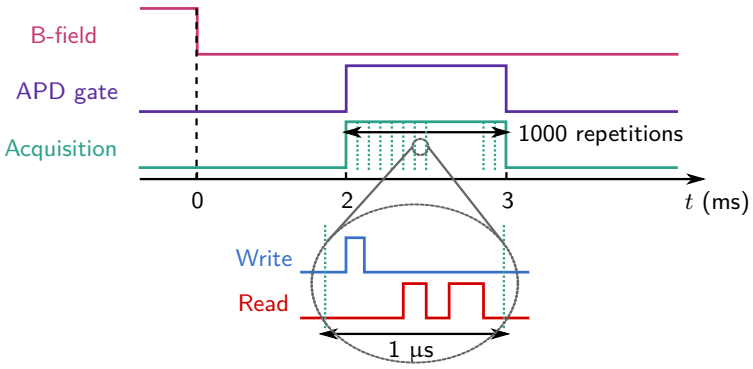

FIGURE C.2 : Timing for the DLCZ protocol acquisition. At $t = 2$ ms, the APD gate and the acquisition trigger signal are switched on, for a duration of 1 ms. During this time, 1000 trials occur, with a duration of 1 µs. Each trial involves a write and a read pulse, followed by a second read pulse which is used as a repump.

C.2.2 Parameter calculation

We want to measure the conditional probability of detecting a second photon, $p_c = p_{12}/p_1$, and the normalized cross-correlation function $g_{12} = p_{12}/(p_1 p_2)$. Thus, we need the values of the probabilities to detect a first photon, p_1, a second photon, p_2, and the joint probability p_{12}. The user defined temporal windows for the field 1 and 2, and events of each trial are analyzed separately, before any summation. The Labview program, shown in figure C.4, detects events from the APD 1 and 2, within the corresponding temporal windows, and also the presence of both events. The goal is to display the results in real time, but some statistic is needed, so we average over M MOT cycles, the number M being user-defined. Therefore, the program sums the detected events over $n = M\times$ 1000 trials, and obtains n_1, n_2 and n_{12} the number of events from APD 1, 2, and joint events respectively. Thus, the probabilities are simply given by $p_1 = n_1/N$, $p_2 = n_2/N$ and $p_{12} = n_{12}/N$. Finally, the parameters are calculated as

$$p_c = \frac{n_{12}}{n_1} \tag{C.3}$$

$$g_{12} = \frac{n_{12}N}{n_1 n_2}\,, \tag{C.4}$$

displayed in real time, and saved.

Moreover, histogram are computed in order to see the temporal shape of the photons, as well as the leakage from the coupling beams. The histogram of all the events is realized over all the trials, and also displayed in real time.

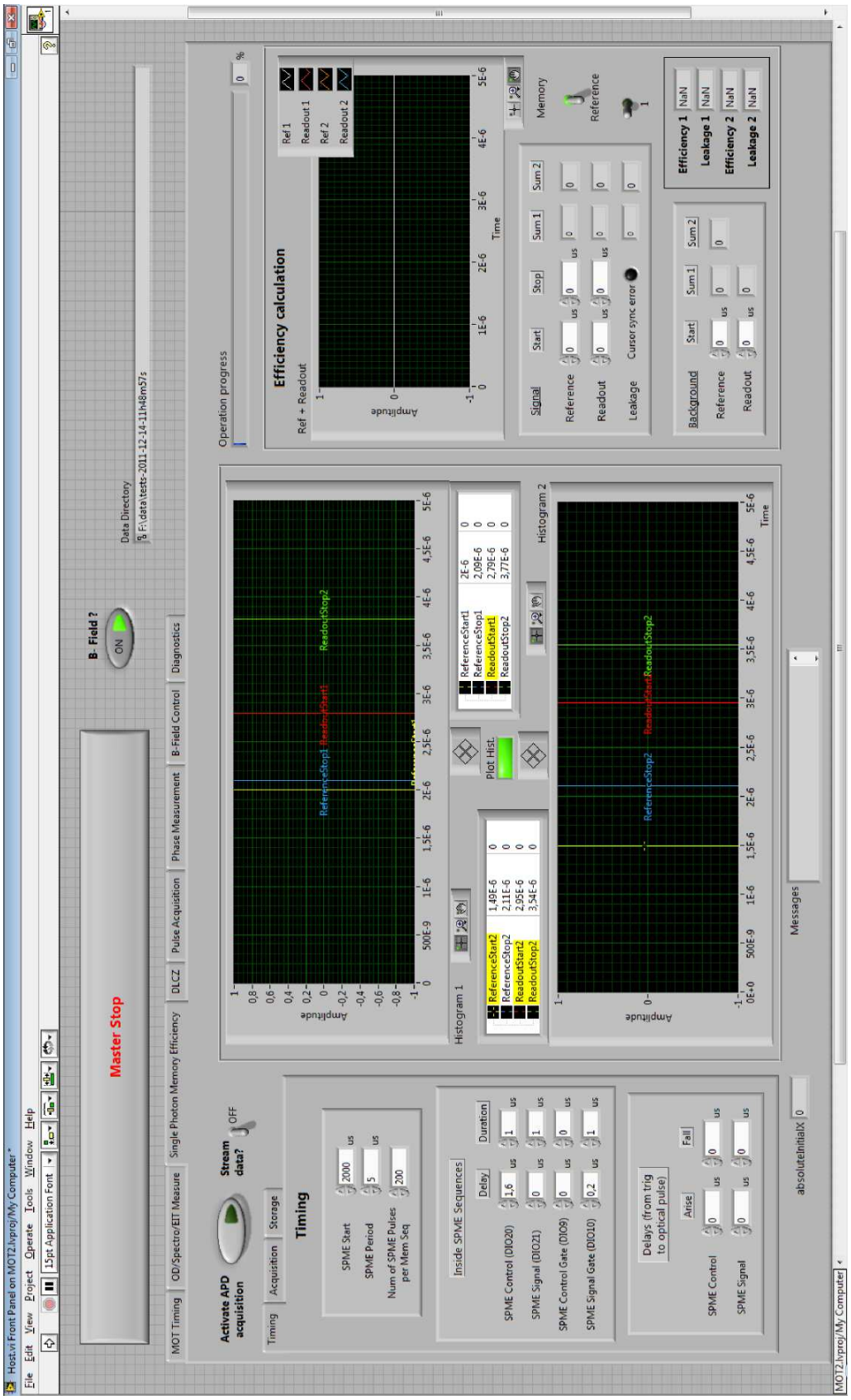

FIGURE C.3 : Front panel, i.e. the user interface, of the `Host.vi` for EIT-based memory implementation.

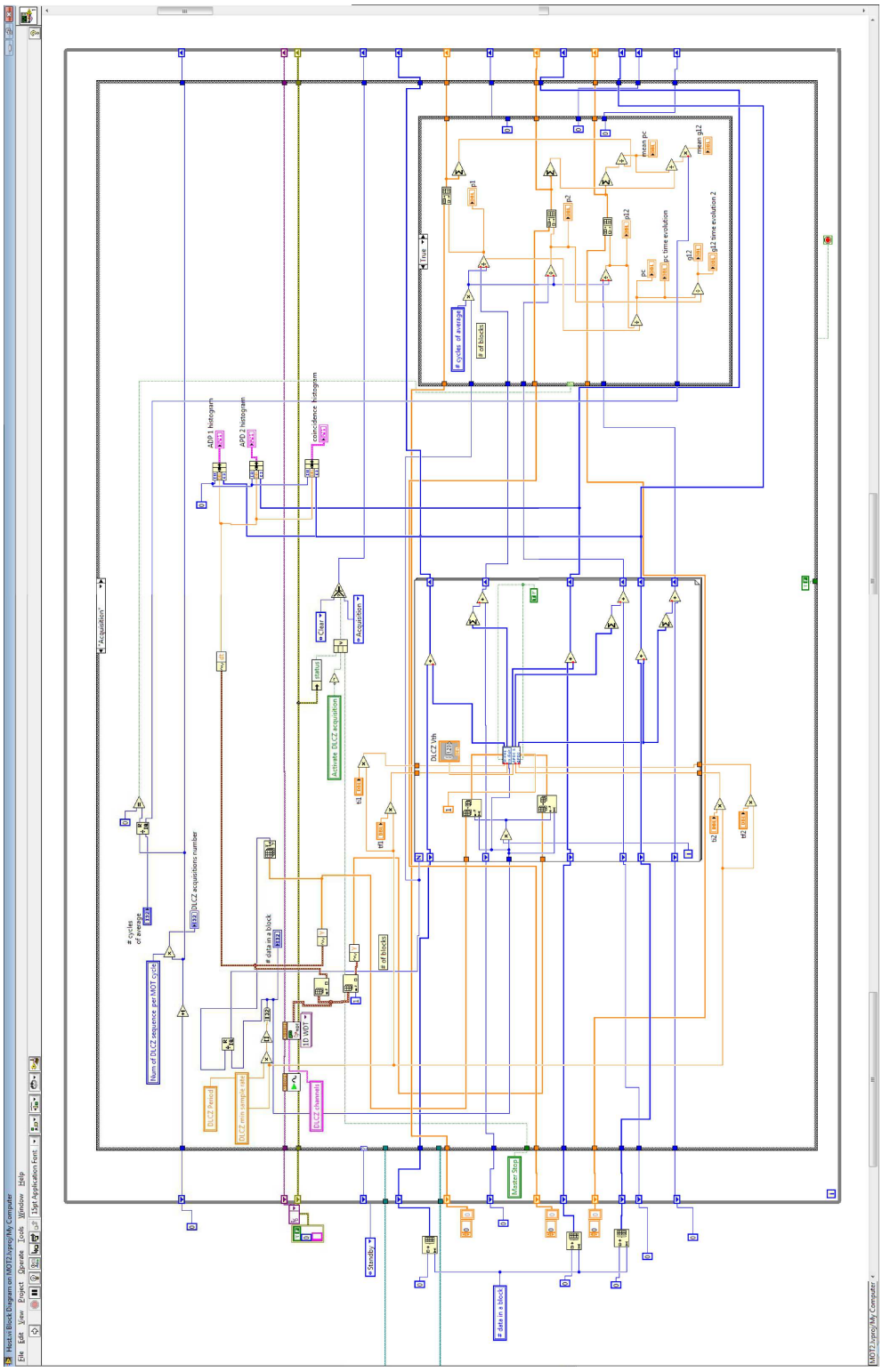

FIGURE C.4 : Part of the block diagram of the `Host.vi` program for the acquisition in the DLCZ protocol.

Appendix D

From Laguerre-Gaussian to Hermite-Gaussian modes

In this appendix, we remind the expression of the electric field amplitude for light beams in Laguerre-Gaussian or Hermite-Gaussian modes of the first order. Then, relations between the two family modes are given.

D.1 Generalities

Laguerre-Gaussian modes as well as Hermite-Gaussian modes form complete sets of solutions of the paraxial wave equation. The Hermite-Gaussian modes, having a rectangular symmetry, are usually expressed in Cartesian coordinates (x, y, z), while the Laguerre-Gaussian modes, having a cylindrical symmetry, are expressed in coordinates cylindrical (r, ϕ, z). Figure D.1 shows the two coordinates systems, related by

$$\begin{cases} x = & r\cos\phi \\ y = & r\sin\phi \\ r^2 = & x^2 + y^2 \end{cases} . \tag{D.1}$$

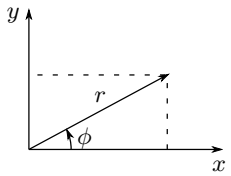

FIGURE D.1 : Two-dimensional Cartesian (x, y) and cylindrical (r, ϕ) coordinates systems.

Omitting the propagation term, the electric field amplitude of the fundamental Gaussian mode TEM_{00}, of waist w_0, is given by

$$E(r,z) = E_0 \frac{w_0}{w(z)} e^{-ik\frac{r^2}{2q(z)}} e^{i\zeta(z)} , \tag{D.2}$$

where the remarkable quantities are

- the Rayleigh range $z_R = \dfrac{\pi w_0^2}{\lambda}$,
- the beam size $w(z) = w_0\sqrt{1+\left(\frac{z}{z_R}\right)^2}$,
- the radius of curvature $R(z) = z\left[1+\left(\frac{z}{z_R}\right)^2\right]$,
- the Gouy phase shift $\zeta(z) = \arctan\left(\frac{z}{z_R}\right)$,
- the complex beam parameter $q(z) = z + iz_R$, with the relation $\dfrac{1}{q(z)} = \dfrac{1}{R(z)} - i\dfrac{\lambda}{\pi w^2(z)}$.

D.2 Laguerre-Gaussian modes

Laguerre-Gaussian modes form a set of optical modes having a helical wavefront, therefore they well describe light beams carrying orbital angular momentum (OAM). Figure D.2 gives the intensity profiles of the first LG_p^l modes depending on the two indexes, l and p. The trivial $\mathrm{LG}_{p=0}^{l=0}$ mode corresponds to the fundamental Gaussian TEM_{00} mode. On the first row, for $p = 0$ and $l \neq 0$, the intensity profiles exhibit a ring shape. These so-called "doughnut modes" present an optical vortex in the center and carry an OAM equal to $l\hbar$. Indeed, the azimuthal l index denotes the circulation of the rotating phase around the beam axis. On the vertical direction, when p increases, the intensity profiles of the modes include additional rings. The radial p index in fact represents the number of electric field cancellation along the beam radius.

For a mode LG_p^l, the field amplitude is expressed as

$$E_{lp}^{\mathrm{LG}}(r,\phi,z) = \sqrt{\frac{p\,!}{2\pi\,(p+l)!}}\,\frac{1}{w(z)}\,e^{il\phi}\left(\frac{\sqrt{2}\,r}{w(z)}\right)^{|l|} L_p^{|l|}\left(\frac{2\,r^2}{w(z)^2}\right) e^{-ik\frac{r^2}{2q(z)}}\,e^{i(2p+|l|+1)\zeta(z)}\,, \qquad \text{(D.3)}$$

where $L_p^l(x)$ are the generalized Laguerre polynomials. Given that $L_0^1(x) = 1$, we can write the amplitude

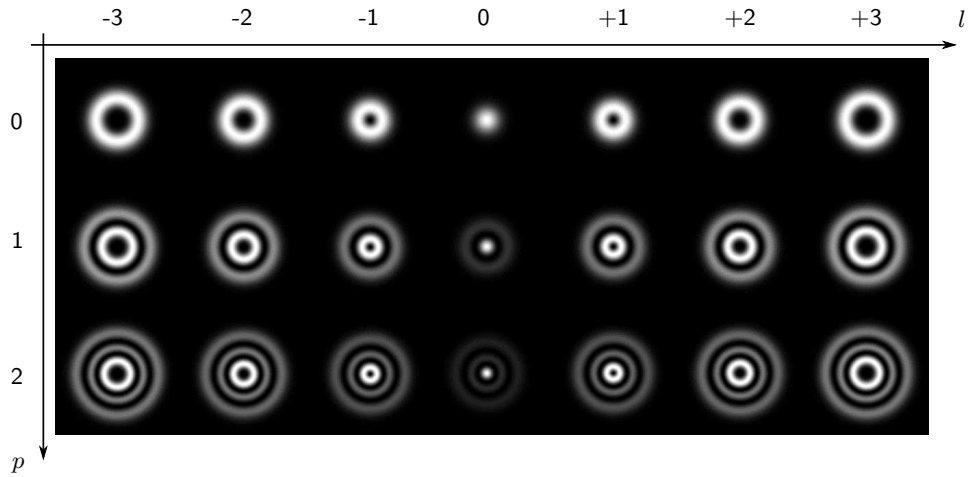

FIGURE D.2 : Laguerre-Gaussian modes. Table of the intensity profiles with p up to 2 and l ranging from -3 to +3.

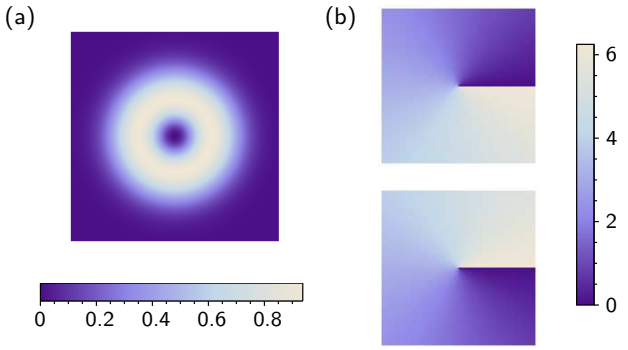

FIGURE D.3 : Laguerre-Gaussian modes LG^{+1} and LG^{-1}. (a) Intensity profiles of the two modes. (b) Phase profile of LG^{+1} and LG^{-1} modes.

of the first-order modes, $\mathrm{LG}_0^{\pm 1}$, as

$$E_{\pm 10}^{\mathrm{LG}}(r,\phi,z) = \frac{1}{\sqrt{\pi}\, w(z)^2}\, e^{il\phi} r\, e^{-ik\frac{r^2}{2q(z)}} e^{2i\zeta(z)}\,. \tag{D.4}$$

These modes carry an OAM equal to $\pm\hbar$. The wavefront is a single helix, corresponding to the fact that the phase rotates by 2π in one wavelength. The handedness is determined by the sign of l, so the LG^{+1} mode is right-handed while the LG^{-1} is left-handed. We sometimes call them right (R) and left (L) modes here.

D.3 Hermite-Gaussian modes

The Hermite-Gaussian modes exhibit a rectangular symmetry and are expressed in Cartesian coordinates. Here is the form of the field amplitude for a mode HG_{mn}

$$E_{mn}^{\mathrm{HG}}(x,y,z) = \sqrt{\frac{1}{2^{m+n-1}\,\pi\, m!\, n!}}\, \frac{1}{w(z)} H_m\left(\frac{\sqrt{2}\,x}{w(z)}\right) H_n\left(\frac{\sqrt{2}\,y}{w(z)}\right) e^{-ik\frac{(x^2+y^2)}{2q(z)}} e^{i(m+n+1)\zeta(z)}, \tag{D.5}$$

with m, n integers, and $H_n(x)$ the Hermite polynomials. For Hermite-Gaussian modes of the first order, the first two polynomials are used

$$\begin{aligned} H_0(x) &= 1 \\ H_1(x) &= x \end{aligned} \tag{D.6}$$

In the following we explicit the expression of the horizontal and vertical modes as first and of the diagonal and antidiagonal modes then, and show how they can be written as superposition of Laguerre-Gaussian modes.

D.3.1 Horizontal and vertical modes

The electric field amplitude of the horizontal mode HG_{10} is

$$E_{10}^{\mathrm{HG}}(x,y,z) = \sqrt{\frac{2}{\pi}}\, \frac{1}{w(z)^2}\, x\, e^{-ik\frac{(x^2+y^2)}{2q(z)}} e^{2i\zeta(z)}, \tag{D.7}$$

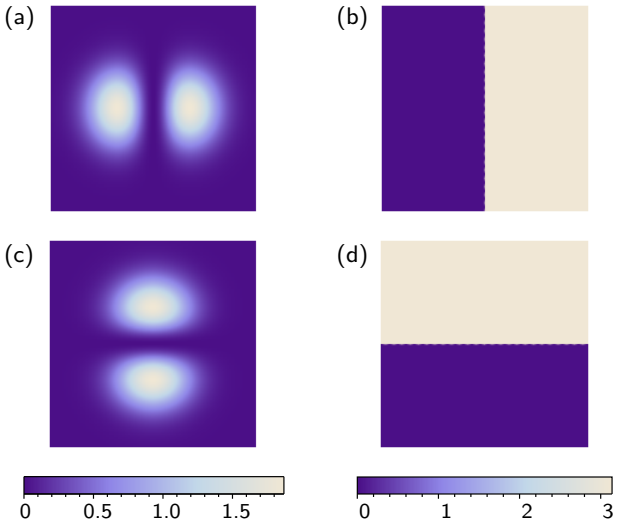

FIGURE D.4 : Horizontal and vertical Hermite-Gaussian modes. (a) Intensity and (b) phase profile of the HG_{10} mode. (c) Intensity and (d) phase profile of the HG_{01} mode.

while the one for the vertical mode HG_{01} is

$$E_{01}^{\mathrm{HG}}(x,y,z) = \sqrt{\frac{2}{\pi}}\frac{1}{w(z)^2}\, y\, e^{-ik\frac{(x^2+y^2)}{2q(z)}} e^{2i\zeta(z)}. \tag{D.8}$$

These modes exhibit two lobes, with a π phase offset, either in the horizontal or vertical direction, as shown in figure D.4.

Relation with $\mathrm{LG}^{\pm 1}$ modes One can already notice that the term $e^{-ik\frac{(x^2+y^2)}{2q(z)}}$ is present in the expressions of both Laguerre-Gaussian modes and Hermite-Gaussian modes. Moreover, the effective Gouy phase term is the same in the four introduced modes. Thus, it appears directly

$$\begin{aligned}
\frac{1}{\sqrt{2}}\left(E_{+10}^{\mathrm{LG}} + E_{-10}^{\mathrm{LG}}\right) &= \frac{1}{\sqrt{2\pi}\, w(z)^2}\, r\,(e^{i\phi} + e^{-i\phi}) e^{-ik\frac{(x^2+y^2)}{2q(z)}} e^{2i\zeta(z)} \\
&= \sqrt{\frac{2}{\pi}}\frac{1}{w(z)^2}\, x e^{-ik\frac{(x^2+y^2)}{2q(z)}} e^{2i\zeta(z)} \\
&= E_{10}^{\mathrm{HG}}\,,
\end{aligned} \tag{D.9}$$

and

$$\begin{aligned}
\frac{1}{\sqrt{2}}\left(E_{+10}^{\mathrm{LG}} - E_{-10}^{\mathrm{LG}}\right) &= \frac{1}{\sqrt{2\pi}\, w(z)^2}\, r\,(e^{i\phi} - e^{-i\phi}) e^{-ik\frac{(x^2+y^2)}{2q(z)}} e^{2i\zeta(z)} \\
&= \sqrt{\frac{2}{\pi}}\frac{1}{w(z)^2}\, y e^{-ik\frac{(x^2+y^2)}{2q(z)}} e^{2i\zeta(z)} \\
&= i E_{01}^{\mathrm{HG}}\,.
\end{aligned} \tag{D.10}$$

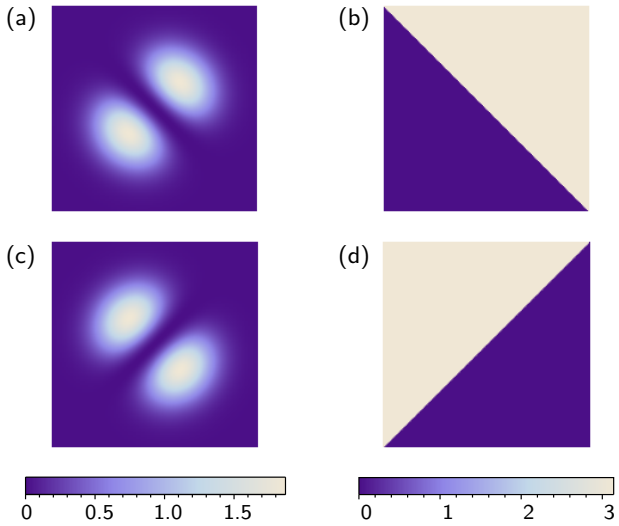

FIGURE D.5 : Diagonal and antidiagonal Hermite-Gaussian modes. (a) Intensity and (b) phase profiles of HG'_{10}. (c) Intensity and (d) phase profiles of HG'_{01}.

The inverse relations can be obtained easily

$$E^{\mathrm{LG}}_{+10} = \frac{1}{\sqrt{2}}\left(E^{\mathrm{HG}}_{10} + E^{\mathrm{HG}}_{01}\right), \tag{D.11}$$

$$E^{\mathrm{LG}}_{-10} = \frac{1}{\sqrt{2}}\left(E^{\mathrm{HG}}_{10} - E^{\mathrm{HG}}_{01}\right). \tag{D.12}$$

D.3.2 Diagonal and antidiagonal modes

Two other interesting modes are the diagonal HG'_{10} and antidiagonal HG'_{01} modes, which correspond to HG_{10} and HG_{01} respectively, rotated by $+45°$. Their intensity and phase profiles are shown in figure D.5. We can write their field amplitudes as the following

$$E^{\mathrm{HG}'}_{10}(x,y,z) = \frac{2}{\sqrt{\pi}}\frac{1}{w(z)^2}(x+y)\, e^{-i\frac{k}{2q(z)}(x^2+y^2)} e^{2i\zeta(z)}, \tag{D.13}$$

$$E^{\mathrm{HG}'}_{01}(x,y,z) = \frac{2}{\sqrt{\pi}}\frac{1}{w(z)^2}(y-x)\, e^{-i\frac{k}{2q(z)}(x^2+y^2)} e^{2i\zeta(z)}. \tag{D.14}$$

Relation with $\mathrm{LG}^{\pm 1}$ modes These two modes can be also expressed as superposition of Laguerre-Gaussian modes. Firstly, the diagonal HG'_{10} mode can be written as

$$\begin{aligned} E^{\mathrm{HG}'}_{10} &= \frac{2}{\sqrt{\pi}}\frac{1}{w(z)^2}(\cos\phi + \sin\phi)\, r\, e^{-i\frac{k}{2q(z)}(x^2+y^2)} e^{2i\zeta(z)} \\ &= \frac{1}{\sqrt{\pi}}\frac{1}{w(z)^2}(1-i)\left(e^{i\phi} + ie^{-i\phi}\right) r\, e^{-i\frac{k}{2q(z)}(x^2+y^2)} e^{2i\zeta(z)} \\ &= \frac{1-i}{\sqrt{2}}\left(E^{\mathrm{LG}}_{+10} + iE^{\mathrm{LG}}_{-10}\right). \end{aligned} \tag{D.15}$$

Secondly, the antidiagonal HG'_{01} mode can be expressed in the same manner as:

$$\begin{aligned} E_{01}^{\mathrm{HG}'} &= \frac{2}{\sqrt{\pi}}\frac{1}{w(z)^2}\,(\sin\phi-\cos\phi)\; r\, e^{-i\frac{k}{2q(z)}(x^2+y^2)}e^{2i\zeta(z)} \\ &= \frac{1}{\sqrt{\pi}}\frac{1}{w(z)^2}\,|-1-i|\left(e^{i\phi}-ie^{-i\phi}\right) r\, e^{-i\frac{k}{2q(z)}(x^2+y^2)}e^{2i\zeta(z)} \\ &= -\frac{1+i}{\sqrt{2}}\left(E_{+10}^{\mathrm{LG}}-iE_{-10}^{\mathrm{LG}}\right)\,. \end{aligned} \tag{D.16}$$

All these relations can be useful for a better understanding of the description of qubits encoded in orbital angular momentum of light in chapter 4.

Appendix E

Effects of detection imperfections on the fidelity

This appendix is related to the state tomography of OAM encoded qubit, performed in chapter 4. Here we detail the effects of imperfections in the detection part, such as the finite extinction ratio and the offset in the measurement of the interferometer phase, on the fidelity between the retrieved state and the ideal state.

We remind the intensity I resulting from the interference between two fields of intensity I_1 and I_2

$$I(\Delta\varphi) = I_1 + I_2 + 2\sqrt{I_1 I_2}\cos(\Delta\varphi)\,, \tag{E.1}$$

leading to a visibility

$$V = \frac{2\sqrt{I_2 I_2}}{I_1 + I_2}\,. \tag{E.2}$$

E.1 For LG states

For the LG states $|\mathrm{R}\rangle$ and $|\mathrm{L}\rangle$, the problem comes from the finite distinction ratio: a small part of a LG^l can be detected on the $-l$ path. As a consequence, small interference fringes are observed at the output of the interferometer when a LG state is sent into. Figure E.1 shows these residual interference fringes, after storage, for both $|\mathrm{R}\rangle$ and $|\mathrm{L}\rangle$ states, with visibilities of 10.3 % and 19.5 % respectively. The residual visibility is larger for the $|\mathrm{L}\rangle$ state, because the distinction ratio is smaller in the R path.

Here we calculate how the fidelity depends on the contamination of the wrong LG mode into the detection paths. We note ε the quantity of LG^l detected on the $-l$ path. Thus, the intensity in both arms are $I_1 = 1-\varepsilon$ and $I_2 = \varepsilon$ for respectively the l and $-l$ path. Thus, the visibility is in this case $2\sqrt{\varepsilon}$. For a $|\mathrm{R}\rangle$ state, the experimental Stokes parameters, defined in section 4.2.2, can be written here as

$$\begin{aligned} S_1 &= 1-\varepsilon \\ S_2 &= 2\sqrt{\varepsilon} \\ S_3 &= 0 \end{aligned} \tag{E.3}$$

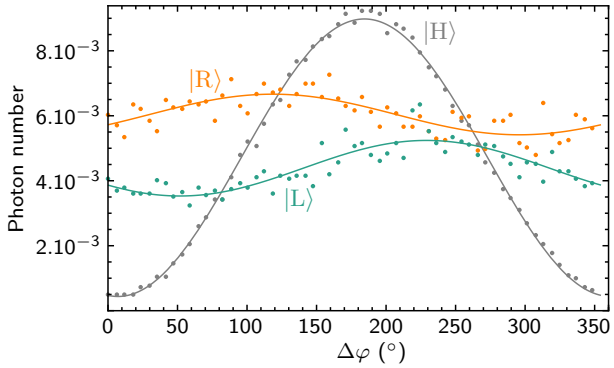

FIGURE E.1 : Residual interference fringes resulting from the finite distinction ratio of the detection. Number of photon per pulse detected on APD 1 is displayed as a function of the interferometer phase $\Delta\varphi$ for the two qubit basis states $|\mathrm{R}\rangle$ and $|\mathrm{L}\rangle$, after storage. Experimental points are fitted by the function $P_1^{exp} = A + B\sin^2(\frac{\pi}{360}(\Delta\varphi + \theta))$, and the resulting visibility $V = B/(2A + B)$ is 10.3 % for the $|\mathrm{R}\rangle$ state and 19.5 % for the $|\mathrm{L}\rangle$. For comparison, the gray lines indicates the same measurement for the $|\mathrm{H}\rangle$ state, with a visibility of 90.7 %.

which gives the following density matrix

$$\hat{\rho} = \begin{pmatrix} 1-\varepsilon/2 & \sqrt{\varepsilon} \\ \sqrt{\varepsilon} & \varepsilon/2 \end{pmatrix}. \tag{E.4}$$

In consequence, the fidelity to the ideal state $|\mathrm{R}\rangle$ is given by

$$\mathcal{F} = 1 - \varepsilon/2\,. \tag{E.5}$$

Figure E.2 displays both the fidelity and the visibility, $V = 2\sqrt{\varepsilon}$, as a function of ε, for distinction ratios ranging from -13 dB to infinity. The fidelity decreases much slower than the visibility increases with the contamination. For our typical value of distinction ratio of -23 dB, corresponding to $\varepsilon = 0.5$ %, the fidelity is 99.75 %, while the visibility of the residual fringes is 14.1 %. The visibilities measured from figure E.1 for $|\mathrm{R}\rangle$ and $|\mathrm{L}\rangle$ state, 10.3 % and 19.5 %, can be explained by a contamination of respectively 0.3 % (-25 dB) and 1 % (-20 dB). Following this simple model, these values of contamination lead to $\mathcal{F} = 99.5$ % and $\mathcal{F} = 99.85$ %. In consequence, the distinction ratio of our detection setup is sufficiently high to obtain in principle good values of the fidelity for the two LG states.

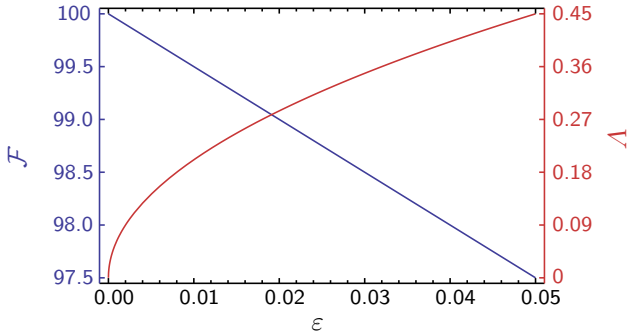

FIGURE E.2 : Fidelity $\mathcal{F}$ and visibility V for the LG states $|\mathrm{R}\rangle$ and $|\mathrm{L}\rangle$, as a function of the quantity ε of LG^l detected on the $-l$ path. The corresponding distinction ratio varies from infinity to -13 dB.

E.2 For HG states

For HG states, two defects can induce a decrease in fidelity, first the unbalancing between the two detection paths (see section 4.1.1.3), and secondly the global phase offset between the theoretical and the experimental fringes. Indeed, we observe in section 4.2.1.3 an offset between the theoretical values $\left(\phi_{\mathrm{H}}^{th}, \phi_{\mathrm{D}}^{th}, \phi_{\mathrm{V}}^{th}, \phi_{\mathrm{A}}^{th}\right) = (0°, 90°, 180°, 270°)$ of the HG state phases, and the values obtained from the fitting of the experimental fringes. This can lead to a decreasing in the fidelity.

Here we take into account both effects. We note the unbalancing 2α, so we obtain $I_1 = 1/2 + \alpha$ and $I_2 = 1/2 - \alpha$, and we note the phase offset β. We take the example of the $|\mathrm{H}\rangle$ state, with $\phi_H^{th} = 0$, but the following is also valid for the three other HG states. For a $|\mathrm{H}\rangle$ state the intensity at the interferometer output can be written as

$$I = 1 + 2\sqrt{1/4 - \alpha^2}\,\cos(\Delta\varphi + \beta)\,. \tag{E.6}$$

Then, the experimental Stokes parameters are expressed as

$$\begin{aligned} S_1 &= 2\alpha \\ S_2 &= 2\sqrt{1/4 - \alpha^2}\,\cos\beta \\ S_3 &= 2\sqrt{1/4 - \alpha^2}\,\sin\beta\,, \end{aligned} \tag{E.7}$$

which gives the following density matrix

$$\hat{\rho} = \begin{pmatrix} 1/2 + \alpha & \sqrt{1/4 - \alpha^2}\,e^{-i\beta} \\ \sqrt{1/4 - \alpha^2}\,e^{i\beta} & 1/2 - \alpha \end{pmatrix}. \tag{E.8}$$

In consequence, we can write the fidelity with the ideal state $|\mathrm{H}\rangle$ as

$$\mathcal{F} = 1/2 + \sqrt{1/4 - \alpha^2}\,\cos\beta\,. \tag{E.9}$$

The fidelity is represented on figure E.3 for a large range of α and β. For the extreme case of an unbalancing of 1 and/or a phase offset of 90 %, the fidelity decreases down to 50 %, which is the value for two orthogonal states. In our experimental setup, the unbalancing is typically around 15 %, and the

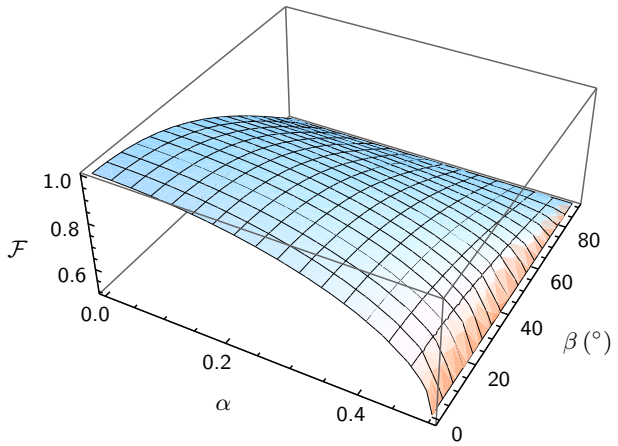

FIGURE E.3 : Fidelity $\mathcal{F}$ as a function of the unbalancing of the detection for HG state α, and of the offset β in the measurement of the interferometer phase.

offset difference around 10°. For these values, we find $\mathcal{F} = 98.7$ %, which is in agreement with the corrected fidelities given in table 4.2.

Appendix F

Atomic filter for the DLCZ experiment

In the DLCZ experiment described in chapter 5 , the first emitted photon is filtered in frequency in order to ensure that the field 1 frequency is around the $|F = 3\rangle \rightarrow |F' = 4\rangle$ transition. Indeed, if the atom excited by the write pulse decays in the initial $|F = 4\rangle$ state, no collective excitation is created in the atomic ensemble, and no second photon will be emitted during the read process. Thus, the conditional probability p_c to detect the second photon, as well as the correlation function g_{12} would decrease. Because of this filter, the effective repetition rate of the experiment, namely p_1 decreases, but the quality of the source is improved.

We chose the simple solution of an atomic filter, which consists in a cesium cell, where the atoms are pumped into a unique hyperfine ground state, $|F = 4\rangle$, by an auxiliary beam (see figure F.1). The pump beam, on resonance with the $|F = 3\rangle \rightarrow |F' = 4\rangle$ transition, is sent off-axis during the build-up of the MOT and the atomic preparation stage, but not during the memory implementation. Thus, despite the large power of about 10 mW, the pump beam does not induce noise on the single-photon detector. Furthermore, by using a paraffin-coated cell, we obtain population lifetimes around 10 ms, which is long in front of the duration of the memory implementation.

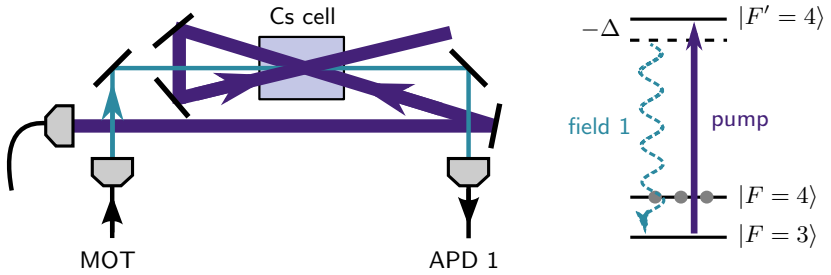

FIGURE F.1 : Atomic filter for the field 1 photon. In order to detect the field 1 around the $|F = 3\rangle \rightarrow |F' = 4\rangle$ transition and to absorb photons around the $|F = 4\rangle \rightarrow |F' = 4\rangle$, the field 1 passes through a cesium cell, where all the atoms are pumped into $|F = 4\rangle$ thanks to a large and strong pump beam on resonance with the $|F = 3\rangle \rightarrow |F' = 4\rangle$ transition.

We tested the filtering performances with low power coherent light. A light beam on resonance with the $|F = 3\rangle \rightarrow |F' = 4\rangle$ transition is sent to estimate the transmission of the field 1 photons, and light

that couples the $|F = 4\rangle$ to the $|F' = 4\rangle$ states enables us to measure the absorption of the photons we do not want to detect. The cell is heated in order to increase the number of atoms, and thus to increase the absorption of the unwanted field. For this purpose, heating wires are wrapped around the stem and around the body cell, and the temperature of each region is measured thanks to thermistors. The heating wire is twisted so as to not induce any magnetic field in the atomic cell, and its resistance is 12 Ω/m, the length being around 30 cm. The wires are supplied in current through a load resistance of 10 Ω. Thus, the stem and the cell are heated up to two different temperatures, respectively T_{stem} and T_{cell}.

We observe the normalized intensity of the two transmitted beams as a function of time. In the experiment, the pump is switched off few microseconds before the several trials of the DLCZ scheme start for 1 ms. Thus, we are mainly interested of the filter performances during the first millisecond after the switching time of the pump. Figure F.2 shows the filter performances for two heating configurations. First, for $T_{cell} = 34°C$ and $T_{stem} = 32°C$ (panel (a)), the transmission of the $|F = 3\rangle \rightarrow |F' = 4\rangle$ light is 0.75 between $t = 0$ and $t = 1$ ms, while it is 5×10^{-2} for the $|F = 4\rangle \rightarrow |F' = 4\rangle$ light. Second, for $T_{cell} = 38°C$ and $T_{stem} = 40°C$ (panel (b)), the transmission of the $|F = 3\rangle \rightarrow |F' = 4\rangle$ light is 0.6 at $t = 0$, and 3×10^{-2} for the $|F = 4\rangle \rightarrow |F' = 4\rangle$ light.

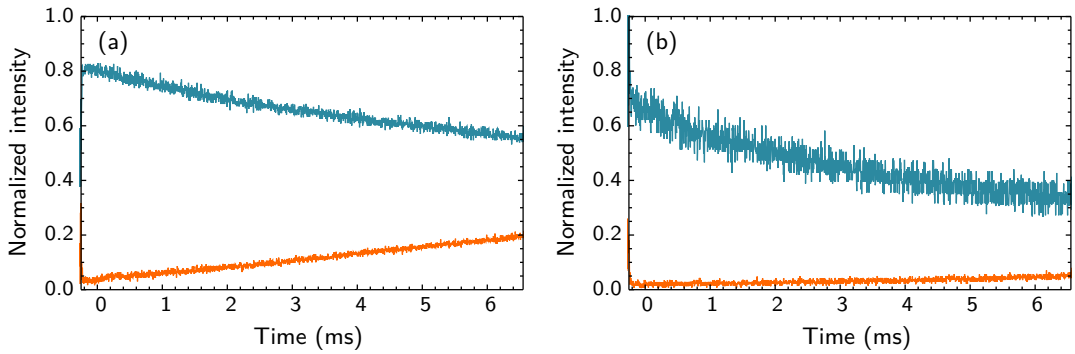

FIGURE F.2 : Atomic filter performances for two heating configurations, (a) $T_{cell} = 34°C$ and $T_{stem} = 32°C$ and (b) $T_{cell} = 38°C$ and $T_{stem} = 40°C$. Normalized intensities of weak coherent beams as a function of time, the pump being turned off at $t = 0$. Blue lines correspond to a $|F = 3\rangle \rightarrow |F' = 4\rangle$ light, orange lines to $|F = 4\rangle \rightarrow |F' = 4\rangle$ light.

Appendix G

Homodyne detection

G.1 Principle

The homodyne detection aims at detecting the quadrature components of a single-mode electromagnetic field of frequency ω, which can be expressed as

$$\hat{E}(t) = \frac{\mathcal{E}}{\sqrt{2}}\left(\hat{a}e^{-i\omega t} + \hat{a}^{\dagger}e^{i\omega t}\right) = \mathcal{E}\left(\hat{x}\cos(\omega t) + \hat{p}\sin(\omega t)\right) , \tag{G.1}$$

where $\hat{a}$ and $\hat{a}^{\dagger}$ are the annihilation and creation operators, $\hat{x}$ and $\hat{p}$ the quadrature operators.

A scheme of the homodyne detection operation is displayed in figure G.1(a). The signal field to measure, $\hat{a}_s$, is mixed on a 50/50 beam splitter with a strong local oscillator field, $\hat{a}_{LO}$ with a phase

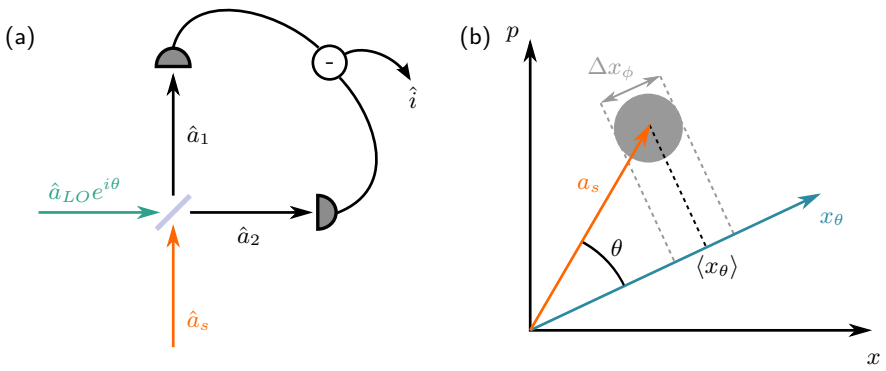

FIGURE G.1 : Homodyne detection principle. (a) The homodyne detection scheme involves a strong local oscillator, $\hat{a}_{LO}e^{i\theta}$, mixed on a 50/50 beam splitter with the signal to measure, $\hat{a}_s$. Both outputs are detected by photodiodes, and the currents are subtracted. (b) Optical phase diagram where the signal field is represented with its area of uncertainty. The homodyne measurement projects the signal field on the rotated quadrature $\hat{x}_\theta$, and gives access to the fluctuations of the quadrature component x_θ of the signal field.

difference θ. The output fields can be written as:

$$\hat{a}_{1,2} = \frac{\hat{a}_s \pm \hat{a}_{LO} e^{i\theta}}{\sqrt{2}} \,. \tag{G.2}$$

Each field is detected by a photodiode, which provides in the ideal case a current $\hat{i}_j$ proportional to the photon number $\hat{a}_j^\dagger \hat{a}_j$ where $j = 1, 2$,

$$\hat{i}_{1,2} \propto \hat{a}_s^\dagger \hat{a}_s + \hat{a}_{LO}^\dagger \hat{a}_{LO} \pm \hat{a}_s^\dagger \hat{a}_{LO} e^{i\theta} \pm \hat{a}_s \hat{a}_{LO}^\dagger e^{-i\theta} \tag{G.3}$$

$$\propto |E_s|^2 + |E_{LO}|^2 \pm |E_{LO}| \left(\hat{a}_s^\dagger e^{i\theta} + \hat{a}_s e^{-i\theta} \right) \,. \tag{G.4}$$

Therefore, the subtraction of the two photocurrents gives

$$\hat{i} = \hat{i}_1 - \hat{i}_2 \propto |E_{LO}| \hat{x}_\theta \,, \tag{G.5}$$

where $\hat{x}_\theta$ is the rotated quadrature operators, defined as

$$\hat{x}_\theta = \frac{\hat{a}^\dagger e^{i\theta} + \hat{a} e^{-i\theta}}{\sqrt{2}} = \cos\theta \, \hat{x} + \sin\theta \, \hat{p} \,. \tag{G.6}$$

Thus, the homodyne measurement corresponds to a projection of the signal field along x_θ in the optical phase diagram, as shown in figure G.1(b). By performing a large amount of measurement with the phase θ randomly evolving, the fluctuations of the quadrature components can be accessed. Starting from this raw data set, we can perform a complete tomography of the signal state, via the iterative maximum likelihood algorithm, leading to the reconstruction of the density matrix and the associated Wigner function.

G.2 Details about the experimental setup

We realized an homodyne detection in order to perform the state tomography of the retrieved photon from our atomic ensemble via the DLCZ protocol, as described in chapter 5.

We use photodiodes (Hamamatsu, S5971) having a efficiency $\eta_d = 92$ % without the protective window (88 % with the window) at 852 nm. Diodes with high efficiency, higher than 98 %, may be obtained soon from Hamamatsu (special order, in collaboration with A. Furusawa). At the polarization

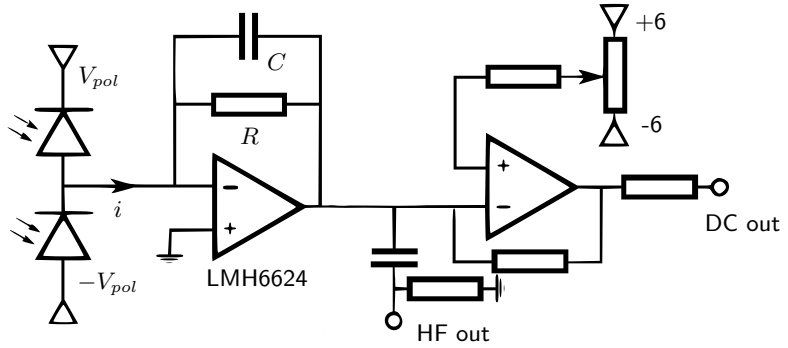

FIGURE G.2 : Schematic electronic circuit of the homodyne detection. The photodiode currents are subtracted, converted into voltages and amplified. The high frequency signal is taken right after the amplification, while the constant component is obtained after filtering.

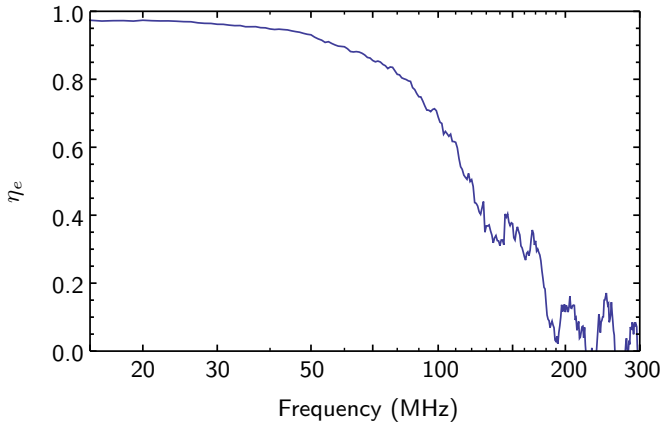

FIGURE G.3 : Effective efficiency η_e of the homodyne detection as a function of the frequency.

voltage $V_{pol} = 10$ V, the capacitance is only 3 pF. Photocurrents of both detectors are directly subtracted before amplification, using an electronic circuit designed in the LKB, schematically displayed on figure G.2.

The homodyne detection must exhibit a flat response within its bandwidth range. Moreover, the gain must be sufficiently high to obtain a signal far above the electronic noise, the latter being considered as an optical loss channel [Kumar et al., 2012]. The resistance R is adjusted to set the gain, whereas the capacitance C is adjusted to optimize the flatness of the homodyne response. The bandwidth of the homodyne detection results from these two adjustments. A trade-off is found with $R = 3$ kΩ, the value of C being tunable from 1.5 and 10 pF. We then measure the effective efficiency η_e of the homodyne detection, expressed as

$$\eta_e = 1 - 10^{-(SN+EN)/10}, \tag{G.7}$$

with SN the shot noise, and EN the electronic noise, both in dBm [Kumar et al., 2012]. Figure G.3 displays η of the resulting setup, which shows a bandwidth of 100 MHz. The behavior at low frequencies is not visible here, but a cutting occurs around 1 MHz.

Bibliography

A

[Abi-Salloum, 2010] Abi-Salloum, T. Y. (2010). Electromagnetically induced transparency and autler-townes splitting: Two similar but distinct phenomena in two categories of three-level atomic systems. *Phys. Rev. A*, 81(5):053836.

[Afzelius et al., 2009] Afzelius, M., Simon, C., de Riedmatten, H., and Gisin, N. (2009). Multimode quantum memory based on atomic frequency combs. *Phys. Rev. A*, 79(5):052329.

[Afzelius et al., 2010] Afzelius, M., Usmani, I., Amari, A., Lauritzen, B., Walther, A., Simon, C., Sangouard, N., Minář, J., de Riedmatten, H., Gisin, N., and Kröll, S. (2010). Demonstration of atomic frequency comb memory for light with spin-wave storage. *Phys. Rev. Lett.*, 104(4):040503.

[Alexander et al., 2007] Alexander, A., Longdell, J., Sellars, M., and Manson, N. (2007). Coherent information storage with photon echoes produced by switching electric fields. *Journal of Luminescence*, 127(1):94–97.

[Alexander et al., 2006] Alexander, A. L., Longdell, J. J., Sellars, M. J., and Manson, N. B. (2006). Photon echoes produced by switching electric fields. *Phys. Rev. Lett.*, 96(4):043602.

[Allen et al., 2003] Allen, L., Barnett, S. M., and Padgett, M. J. (2003). *Optical Angular Momentum*. Institute of Physics Publishing, Bristol, UK.

[Alzetta et al., 1976] Alzetta, G., Gozzini, A., Moi, L., and Orriols, G. (1976). An experimental method for the observation of r.f. transitions and laser beat resonances in oriented na vapour. *Nuov Cim B*, 36(1):5–20.

[André, 2005] André, A. (2005). *Nonclassical States of Light and Atomic Ensembles: Generation and New Applications*. PhD thesis, Harvard University, Cambridge, Massachusetts.

[Anisimov and Kocharovskaya, 2008] Anisimov, P. and Kocharovskaya, O. (2008). Decaying-dressed-state analysis of a coherently driven three-level lambda system. *Journal of Modern Optics*, 55(19-20):3159–3171.

[Anisimov et al., 2011] Anisimov, P. M., Dowling, J. P., and Sanders, B. C. (2011). Objectively discerning autler-townes splitting from electromagnetically induced transparency. *Phys. Rev. Lett.*, 107(16):163604.

[Appel et al., 2008] Appel, J., Figueroa, E., Korystov, D., Lobino, M., and Lvovsky, A. I. (2008). Quantum memory for squeezed light. *Phys. Rev. Lett.*, 100(9):093602.

[Arikawa et al., 2010] Arikawa, M., Honda, K., Akamatsu, D., Nagatsuka, S., Akiba, K., Furusawa, A., and Kozuma, M. (2010). Quantum memory of a squeezed vacuum for arbitrary frequency sidebands. *Phys. Rev. A*, 81(2):021605.

[Arimondo, 1996] Arimondo, E. (1996). Coherent population trapping in laser spectroscopy. In E. Wolf, editor, *Progress in Optics*, volume Volume 35, pages 257–354. Elsevier.

[Autler and Townes, 1955] Autler, S. H. and Townes, C. H. (1955). Stark effect in rapidly varying fields. *Phys. Rev.*, 100(2):703–722.

B

[Baillard et al., 2006] Baillard, X., Gauguet, A., Bize, S., Lemonde, P., Laurent, P., Clairon, A., and Rosenbusch, P. (2006). Interference-filter-stabilized external-cavity diode lasers. *Optics Communications*, 266(2):609–613.

[Bao et al., 2012] Bao, X.-H., Reingruber, A., Dietrich, P., Rui, J., Dück, A., Strassel, T., Li, L., Liu, N.-L., Zhao, B., and Pan, J.-W. (2012). Efficient and long-lived quantum memory with cold atoms inside a ring cavity. *Nat Phys*, 8(7):517–521.

[Bennett and Brassard, 1984] Bennett, C. H. and Brassard, G. (1984). Quantum cryptography: Public key distribution and coin tossing. In *Proceedings of IEEE International Conference on Computers, Systems, and Signal Processing*, page 175, Bangalore.

[Berkhout et al., 2010] Berkhout, G. C. G., Lavery, M. P. J., Courtial, J., Beijersbergen, M. W., and Padgett, M. J. (2010). Efficient sorting of orbital angular momentum states of light. *Phys. Rev. Lett.*, 105(15):153601.

[Bernien et al., 2012] Bernien, H., Childress, L., Robledo, L., Markham, M., Twitchen, D., and Hanson, R. (2012). Two-photon quantum interference from separate nitrogen vacancy centers in diamond. *Phys. Rev. Lett.*, 108(4):043604.

[Bernien et al., 2013] Bernien, H., Hensen, B., Pfaff, W., Koolstra, G., Blok, M. S., Robledo, L., Taminiau, T. H., Markham, M., Twitchen, D. J., Childress, L., and Hanson, R. (2013). Heralded entanglement between solid-state qubits separated by three metres. *Nature*, 497(7447):86–90.

[Bimbard et al., 2013] Bimbard, E., Boddeda, R., Vitrant, N., Grankin, A., Parigi, V., Stanojevic, J., Ourjoumtsev, A., and Grangier, P. (2013). Homodyne tomography of a single photon retrieved on demand from a cavity-enhanced cold atom memory. arXiv e-print 1310.1228.

[Boller et al., 1991] Boller, K.-J., Imamolu, A., and Harris, S. E. (1991). Observation of electromagnetically induced transparency. *Phys. Rev. Lett.*, 66(20):2593–2596.

[Braje et al., 2004] Braje, D. A., Balić, V., Goda, S., Yin, G. Y., and Harris, S. E. (2004). Frequency mixing using electromagnetically induced transparency in cold atoms. *Phys. Rev. Lett.*, 93(18):183601.

[Briegel et al., 1998] Briegel, H.-J., Dür, W., Cirac, J. I., and Zoller, P. (1998). Quantum repeaters: The role of imperfect local operations in quantum communication. *Phys. Rev. Lett.*, 81(26):5932–5935.

[Burks, 2010] Burks, S. (2010). *Towards a quantum memory for non-classical light with cold atomic ensembles*. PhD thesis, Université Pierre et Marie Curie, Paris, France.

[Burnham and Anderson, 2002] Burnham, K. P. and Anderson, D. R. (2002). *Model Selection and Multimodel Inference - A Practical Information-Theoretic Approach*. Springer-Verlag, New York, 2nd edition.

[Bussieres et al., 2013] Bussieres, F., Sangouard, N., Afzelius, M., de Riedmatten, H., Simon, C., and Tittel, W. (2013). Prospective applications of optical quantum memories. arXiv e-print 1306.6904.

C

[Chabé et al., 2007] Chabé, J., Lignier, H., Szriftgiser, P., and Garreau, J. C. (2007). Improving raman velocimetry of laser-cooled cesium atoms by spin-polarization. *Optics Communications*, 274(1):254–259.

[Chanelière et al., 2005] Chanelière, T., Matsukevich, D. N., Jenkins, S. D., Lan, S.-Y., Kennedy, T. a. B., and Kuzmich, A. (2005). Storage and retrieval of single photons transmitted between remote quantum memories. *Nature*, 438(7069):833–836.

[Chen et al., 2006] Chen, S., Chen, Y.-A., Strassel, T., Yuan, Z.-S., Zhao, B., Schmiedmayer, J., and Pan, J.-W. (2006). Deterministic and storable single-photon source based on a quantum memory. *Phys. Rev. Lett.*, 97(17):173004.

[Chen et al., 2008] Chen, Y.-A., Chen, S., Yuan, Z.-S., Zhao, B., Chuu, C.-S., Schmiedmayer, J., and Pan, J.-W. (2008). Memory-built-in quantum teleportation with photonic and atomic qubits. *Nat Phys*, 4(2):103–107.

[Chen et al., 2013] Chen, Y.-H., Lee, M.-J., Wang, I.-C., Du, S., Chen, Y.-F., Chen, Y.-C., and Yu, I. A. (2013). Coherent optical memory with high storage efficiency and large fractional delay. *Phys. Rev. Lett.*, 110(8):083601.

[Choi, 2011] Choi, K. S. (2011). *Coherent control of entanglement with atomic ensembles*. PhD thesis, California Institute of Technology, Pasadena, California, US.

[Choi et al., 2008] Choi, K. S., Deng, H., Laurat, J., and Kimble, H. J. (2008). Mapping photonic entanglement into and out of a quantum memory. *Nature*, 452(7183):67–71.

[Choi et al., 2010] Choi, K. S., Goban, A., Papp, S. B., van Enk, S. J., and Kimble, H. J. (2010). Entanglement of spin waves among four quantum memories. *Nature*, 468(7322):412–416.

[Chou et al., 2005] Chou, C. W., de Riedmatten, H., Felinto, D., Polyakov, S. V., van Enk, S. J., and Kimble, H. J. (2005). Measurement-induced entanglement for excitation stored in remote atomic ensembles. *Nature*, 438(7069):828–832.

[Chou et al., 2004] Chou, C. W., Polyakov, S. V., Kuzmich, A., and Kimble, H. J. (2004). Single-photon generation from stored excitation in an atomic ensemble. *Phys. Rev. Lett.*, 92(21):213601.

[Chuu et al., 2008] Chuu, C.-S., Strassel, T., Zhao, B., Koch, M., Chen, Y.-A., Chen, S., Yuan, Z.-S., Schmiedmayer, J., and Pan, J.-W. (2008). Quantum memory with optically trapped atoms. *Phys. Rev. Lett.*, 101(12):120501.

[Clausen et al., 2012] Clausen, C., Bussières, F., Afzelius, M., and Gisin, N. (2012). Quantum storage of heralded polarization qubits in birefringent and anisotropically absorbing materials. *Phys. Rev. Lett.*, 108(19):190503.

[Clausen et al., 2011] Clausen, C., Usmani, I., Bussières, F., Sangouard, N., Afzelius, M., de Riedmatten, H., and Gisin, N. (2011). Quantum storage of photonic entanglement in a crystal. *Nature*, 469(7331):508–511.

[Clauser, 1974] Clauser, J. F. (1974). Experimental distinction between the quantum and classical field-theoretic predictions for the photoelectric effect. *Phys. Rev. D*, 9(4):853–860.

[Cohen-Tannoudji et al., 1992] Cohen-Tannoudji, C., Dupont-Roc, J., and Grynberg, G. (1992). *Atom-photon interactions: basic processes and applications*. Wiley Interscience, New York.

[Cohen-Tannoudji and Reynaud, 1977] Cohen-Tannoudji, C. and Reynaud, S. (1977). Simultaneous saturation of two atomic transitions sharing a common level. *J. Phys. B: At. Mol. Phys.*, 10(12):2311.

[Cviklinski et al., 2008] Cviklinski, J., Ortalo, J., Laurat, J., Bramati, A., Pinard, M., and Giacobino, E. (2008). Reversible quantum interface for tunable single-sideband modulation. *Phys. Rev. Lett.*, 101(13):133601.

D

[Dada et al., 2011] Dada, A. C., Leach, J., Buller, G. S., Padgett, M. J., and Andersson, E. (2011). Experimental high-dimensional two-photon entanglement and violations of generalized bell inequalities. *Nature Physics*, 7(9):677–680.

[Damon et al., 2011] Damon, V., Bonarota, M., Louchet-Chauvet, A., Chanelière, T., and Gouët, J.-L. L. (2011). Revival of silenced echo and quantum memory for light. *New J. Phys.*, 13(9):093031.

[Dantan et al., 2006] Dantan, A., Cviklinski, J., Pinard, M., and Grangier, P. (2006). Dynamics of a pulsed continuous-variable quantum memory. *Phys. Rev. A*, 73(3):032338.

[De Greve et al., 2012] De Greve, K., Yu, L., McMahon, P. L., Pelc, J. S., Natarajan, C. M., Kim, N. Y., Abe, E., Maier, S., Schneider, C., Kamp, M., Höfling, S., Hadfield, R. H., Forchel, A., Fejer, M. M., and Yamamoto, Y. (2012). Quantum-dot spin-photon entanglement via frequency downconversion to telecom wavelength. *Nature*, 491(7424):421–425.

[de Riedmatten et al., 2008] de Riedmatten, H., Afzelius, M., Staudt, M. U., Simon, C., and Gisin, N. (2008). A solid-state light–matter interface at the single-photon level. *Nature*, 456(7223):773–777.

[Deutsch and Jozsa, 1992] Deutsch, D. and Jozsa, R. (1992). Rapid solution of problems by quantum computation. In *Proceedings of the Royal Society of London. Series A: Mathematical and Physical Sciences*, volume 439, pages 553–558.

[Ding et al., 2013] Ding, D.-S., Zhou, Z.-Y., Shi, B.-S., and Guo, G.-C. (2013). Single-photon-level quantum image memory based on cold atomic ensembles. arXiv e-print 1305.2675.

[Duan et al., 2002] Duan, L. M., Cirac, J. I., and Zoller, P. (2002). Three-dimensional theory for interaction between atomic ensembles and free-space light. *Phys. Rev. A*, 66(2):023818.

[Duan et al., 2001] Duan, L.-M., Lukin, M. D., Cirac, J. I., and Zoller, P. (2001). Long-distance quantum communication with atomic ensembles and linear optics. *Nature*, 414(6862):413–418.

[Duan and Monroe, 2010] Duan, L.-M. and Monroe, C. (2010). Colloquium: Quantum networks with trapped ions. *Rev. Mod. Phys.*, 82(2):1209–1224.

[Dudin et al., 2013] Dudin, Y. O., Li, L., and Kuzmich, A. (2013). Light storage on the time scale of a minute. *Phys. Rev. A*, 87(3):031801.

E

[Eisaman et al., 2005] Eisaman, M. D., André, A., Massou, F., Fleischhauer, M., Zibrov, A. S., and Lukin, M. D. (2005). Electromagnetically induced transparency with tunable single-photon pulses. *Nature*, 438(7069):837–841.

[England et al., 2012] England, D. G., Michelberger, P. S., Champion, T. F. M., Reim, K. F., Lee, K. C., Sprague, M. R., Jin, X.-M., Langford, N. K., Kolthammer, W. S., Nunn, J., and Walmsley, I. A. (2012). High-fidelity polarization storage in a gigahertz bandwidth quantum memory. *J. Phys. B: At. Mol. Opt. Phys.*, 45(12):124008.

F

[Fano, 1961] Fano, U. (1961). Effects of configuration interaction on intensities and phase shifts. *Phys. Rev.*, 124(6):1866–1878.

[Felinto et al., 2005] Felinto, D., Chou, C. W., de Riedmatten, H., Polyakov, S. V., and Kimble, H. J. (2005). Control of decoherence in the generation of photon pairs from atomic ensembles. *Phys. Rev. A*, 72(5):053809.

[Feynman, 1982] Feynman, R. P. (1982). Simulating physics with computers. *Int J Theor Phys*, 21(6-7):467–488.

[Fickler et al., 2012] Fickler, R., Lapkiewicz, R., Plick, W. N., Krenn, M., Schaeff, C., Ramelow, S., and Zeilinger, A. (2012). Quantum entanglement of high angular momenta. *Science*, 338(6107):640–643.

[Fleischhauer et al., 2005] Fleischhauer, M., Imamoglu, A., and Marangos, J. P. (2005). Electromagnetically induced transparency: Optics in coherent media. *Rev. Mod. Phys.*, 77(2):633–673.

[Fleischhauer and Lukin, 2000] Fleischhauer, M. and Lukin, M. D. (2000). Dark-state polaritons in electromagnetically induced transparency. *Phys. Rev. Lett.*, 84(22):5094–5097.

[Fleischhauer and Lukin, 2002] Fleischhauer, M. and Lukin, M. D. (2002). Quantum memory for photons: Dark-state polaritons. *Phys. Rev. A*, 65(2):022314.

G

[Gao et al., 2012] Gao, W. B., Fallahi, P., Togan, E., Miguel-Sanchez, J., and Imamoglu, A. (2012). Observation of entanglement between a quantum dot spin and a single photon. *Nature*, 491(7424):426–430.

[Giner, 2013] Giner, L. (2013). *Etude de la transparence électromagnétiquement induite dans un ensemble d'atomes froids et applications aux mémoires quantiques*. PhD thesis, Université Pierre et Marie Curie, Paris, France.

[Giovannetti et al., 2011] Giovannetti, V., Lloyd, S., and Maccone, L. (2011). Advances in quantum metrology. *Nat Photon*, 5(4):222–229.

[Gündoğan et al., 2012] Gündoğan, M., Ledingham, P. M., Almasi, A., Cristiani, M., and de Riedmatten, H. (2012). Quantum storage of a photonic polarization qubit in a solid. *Phys. Rev. Lett.*, 108(19):190504.

[Gündoğan et al., 2013] Gündoğan, M., Mazzera, M., Ledingham, P. M., Cristiani, M., and Riedmatten, H. d. (2013). Coherent storage of temporally multimode light using a spin-wave atomic frequency comb memory. *New J. Phys.*, 15(4):045012.

[Gorshkov et al., 2007a] Gorshkov, A. V., André, A., Fleischhauer, M., Sørensen, A. S., and Lukin, M. D. (2007a). Universal approach to optimal photon storage in atomic media. *Phys. Rev. Lett.*, 98(12):123601.

[Gorshkov et al., 2007b] Gorshkov, A. V., André, A., Lukin, M. D., and Sørensen, A. S. (2007b). Photon storage in lambda-type optically dense atomic media. II. free-space model. *Phys. Rev. A*, 76(3):033805.

[Grangier et al., 1986] Grangier, P., Roger, G., and Aspect, A. (1986). Experimental evidence for a photon anticorrelation effect on a beam splitter: A new light on single-photon interferences. *EPL*, 1(4):173.

[Gröblacher et al., 2006] Gröblacher, S., Jennewein, T., Vaziri, A., Weihs, G., and Zeilinger, A. (2006). Experimental quantum cryptography with qutrits. *New Journal of Physics*, 8(5):75–75.

[Grimm et al., 2000] Grimm, R., Weidemüller, M., and Ovchinnikov, Y. B. (2000). Optical dipole traps for neutral atoms. In Benjamin Bederson and Herbert Walther, editor, *Advances In Atomic, Molecular, and Optical Physics*, volume 42, pages 95–170. Academic Press.

[Grover, 1996] Grover, L. K. (1996). A fast quantum mechanical algorithm for database search. In *Proceedings, 28th Annual ACM Symposium on the Theory of Computing (STOC)*, pages 212–219.

H

[Hammerer et al., 2010] Hammerer, K., Sørensen, A. S., and Polzik, E. S. (2010). Quantum interface between light and atomic ensembles. *Rev. Mod. Phys.*, 82(2):1041–1093.

[Harris, 1997] Harris, S. E. (1997). Electromagnetically induced transparency. *Physics Today*, 50(7):36–42.

[Harris et al., 1990] Harris, S. E., Field, J. E., and Imamoğlu, A. (1990). Nonlinear optical processes using electromagnetically induced transparency. *Phys. Rev. Lett.*, 64(10):1107–1110.

[Hau et al., 1999] Hau, L. V., Harris, S. E., Dutton, Z., and Behroozi, C. H. (1999). Light speed reduction to 17 metres per second in an ultracold atomic gas. *Nature*, 397(6720):594–598.

[Hedges et al., 2010] Hedges, M. P., Longdell, J. J., Li, Y., and Sellars, M. J. (2010). Efficient quantum memory for light. *Nature*, 465(7301):1052–1056.

[Heinze et al., 2013] Heinze, G., Hubrich, C., and Halfmann, T. (2013). Stopped light and image storage by electromagnetically induced transparency up to the regime of one minute. *Phys. Rev. Lett.*, 111(3):033601.

[Honda et al., 2008] Honda, K., Akamatsu, D., Arikawa, M., Yokoi, Y., Akiba, K., Nagatsuka, S., Tanimura, T., Furusawa, A., and Kozuma, M. (2008). Storage and retrieval of a squeezed vacuum. *Phys. Rev. Lett.*, 100(9):093601.

[Hosseini et al., 2011a] Hosseini, M., Campbell, G., Sparkes, B. M., Lam, P. K., and Buchler, B. C. (2011a). Unconditional room-temperature quantum memory. *Nat Phys*, 7(10):794–798.

[Hosseini et al., 2011b] Hosseini, M., Sparkes, B. M., Campbell, G., Lam, P. K., and Buchler, B. C. (2011b). High efficiency coherent optical memory with warm rubidium vapour. *Nat Commun*, 2:174.

[Hosseini et al., 2009] Hosseini, M., Sparkes, B. M., Hétet, G., Longdell, J. J., Lam, P. K., and Buchler, B. C. (2009). Coherent optical pulse sequencer for quantum applications. *Nature*, 461(7261):241–245.

[Hétet et al., 2008a] Hétet, G., Hosseini, M., Sparkes, B. M., Oblak, D., Lam, P. K., and Buchler, B. C. (2008a). Photon echoes generated by reversing magnetic field gradients in a rubidium vapor. *Opt. Lett.*, 33(20):2323–2325.

[Hétet et al., 2008b] Hétet, G., Peng, A., Johnsson, M. T., Hope, J. J., and Lam, P. K. (2008b). Characterization of electromagnetically-induced-transparency-based continuous-variable quantum memories. *Phys. Rev. A*, 77(1):012323.

I

[Inoue et al., 2006] Inoue, R., Kanai, N., Yonehara, T., Miyamoto, Y., Koashi, M., and Kozuma, M. (2006). Entanglement of orbital angular momentum states between an ensemble of cold atoms and a photon. *Phys. Rev. A*, 74(5):053809.

[Inoue et al., 2009] Inoue, R., Yonehara, T., Miyamoto, Y., Koashi, M., and Kozuma, M. (2009). Measuring qutrit-qutrit entanglement of orbital angular momentum states of an atomic ensemble and a photon. *Phys. Rev. Lett.*, 103(11):110503.

J

[James et al., 2001] James, D. F. V., Kwiat, P. G., Munro, W. J., and White, A. G. (2001). Measurement of qubits. *Phys. Rev. A*, 64(5):052312.

[Jiang et al., 2009] Jiang, S., Luo, X.-M., Chen, L.-Q., Ning, B., Chen, S., Wang, J.-Y., Zhong, Z.-P., and Pan, J.-W. (2009). Observation of prolonged coherence time of the collective spin wave of an atomic ensemble in a paraffin-coated 87Rb vapor cell. *Phys. Rev. A*, 80(6):062303.

[Julsgaard et al., 2001] Julsgaard, B., Kozhekin, A., and Polzik, E. S. (2001). Experimental long-lived entanglement of two macroscopic objects. *Nature*, 413(6854):400–403.

K

[Kelly et al., 2010] Kelly, W. R., Dutton, Z., Schlafer, J., Mookerji, B., Ohki, T. A., Kline, J. S., and Pappas, D. P. (2010). Direct observation of coherent population trapping in a superconducting artificial atom. *Phys. Rev. Lett.*, 104(16):163601.

[Kimble, 2008] Kimble, H. J. (2008). The quantum internet. *Nature*, 453(7198):1023–1030.

[Knill et al., 2001] Knill, E., Laflamme, R., and Milburn, G. J. (2001). A scheme for efficient quantum computation with linear optics. *Nature*, 409(6816):46–52.

[Kok et al., 2007] Kok, P., Munro, W. J., Nemoto, K., Ralph, T. C., Dowling, J. P., and Milburn, G. J. (2007). Linear optical quantum computing with photonic qubits. *Rev. Mod. Phys.*, 79(1):135–174.

[Krauter et al., 2013] Krauter, H., Salart, D., Muschik, C. A., Petersen, J. M., Shen, H., Fernholz, T., and Polzik, E. S. (2013). Deterministic quantum teleportation between distant atomic objects. *Nat Phys*, 9(7):400–404.

[Kumar et al., 2012] Kumar, R., Barrios, E., MacRae, A., Cairns, E., Huntington, E., and Lvovsky, A. (2012). Versatile wideband balanced detector for quantum optical homodyne tomography. *Optics Communications*, 285(24):5259–5267.

[Kuzmich et al., 2003] Kuzmich, A., Bowen, W. P., Boozer, A. D., Boca, A., Chou, C. W., Duan, L.-M., and Kimble, H. J. (2003). Generation of nonclassical photon pairs for scalable quantum communication with atomic ensembles. *Nature*, 423(6941):731–734.

L

[Langford et al., 2004] Langford, N. K., Dalton, R. B., Harvey, M. D., O'Brien, J. L., Pryde, G. J., Gilchrist, A., Bartlett, S. D., and White, A. G. (2004). Measuring entangled qutrits and their use for quantum bit commitment. *Phys. Rev. Lett.*, 93(5):053601.

[Laurat et al., 2007a] Laurat, J., Choi, K. S., Deng, H., Chou, C. W., and Kimble, H. J. (2007a). Heralded entanglement between atomic ensembles: Preparation, decoherence, and scaling. *Phys. Rev. Lett.*, 99(18):180504.

[Laurat et al., 2007b] Laurat, J., Chou, C.-w., Deng, H., Choi, K. S., Felinto, D., Riedmatten, H. d., and Kimble, H. J. (2007b). Towards experimental entanglement connection with atomic ensembles in the single excitation regime. *New J. Phys.*, 9(6):207.

[Laurat et al., 2006] Laurat, J., de Riedmatten, H., Felinto, D., Chou, C.-W., Schomburg, E. W., and Kimble, H. J. (2006). Efficient retrieval of a single excitation stored in an atomic ensemble. *Opt. Express*, 14(15):6912–6918.

[Lavery et al., 2012] Lavery, M. P. J., Robertson, D. J., Berkhout, G. C. G., Love, G. D., Padgett, M. J., and Courtial, J. (2012). Refractive elements for the measurement of the orbital angular momentum of a single photon. *Opt. Express*, 20(3):2110–2115.

[Leach et al., 2002] Leach, J., Padgett, M. J., Barnett, S. M., Franke-Arnold, S., and Courtial, J. (2002). Measuring the orbital angular momentum of a single photon. *Phys. Rev. Lett.*, 88(25):257901.

[Leonhardt, 1997] Leonhardt, U. (1997). *Measuring the Quantum State of Light*. Cambridge University Press.

[Li et al., 2013] Li, L., Dudin, Y. O., and Kuzmich, A. (2013). Entanglement between light and an optical atomic excitation. *Nature*, 498(7455):466–469.

[Li et al., 2012] Li, Z.-H., Li, Y., Dou, Y.-F., and Zhang, J.-X. (2012). The difference in noise property between the Autler—Townes splitting medium and the electromagnetically induced transparent medium. *Chinese Physics B*, 21(3):034204.

[Liu et al., 2001] Liu, C., Dutton, Z., Behroozi, C. H., and Hau, L. V. (2001). Observation of coherent optical information storage in an atomic medium using halted light pulses. *Nature*, 409(6819):490–493.

[Lukin, 2003] Lukin, M. D. (2003). Colloquium: Trapping and manipulating photon states in atomic ensembles. *Rev. Mod. Phys.*, 75(2):457–472.

[Lvovsky, 2004] Lvovsky, A. I. (2004). Iterative maximum-likelihood reconstruction in quantum homodyne tomography. *J. Opt. B: Quantum Semiclass. Opt.*, 6(6):S556.

[Lvovsky et al., 2001] Lvovsky, A. I., Hansen, H., Aichele, T., Benson, O., Mlynek, J., and Schiller, S. (2001). Quantum state reconstruction of the single-photon fock state. *Phys. Rev. Lett.*, 87(5):050402.

[Lvovsky et al., 2009] Lvovsky, A. I., Sanders, B. C., and Tittel, W. (2009). Optical quantum memory. *Nat Photon*, 3(12):706–714.

M

[MacRae et al., 2012] MacRae, A., Brannan, T., Achal, R., and Lvovsky, A. I. (2012). Tomography of a high-purity narrowband photon from a transient atomic collective excitation. *Phys. Rev. Lett.*, 109(3):033601.

[Mair et al., 2001] Mair, A., Vaziri, A., Weihs, G., and Zeilinger, A. (2001). Entanglement of the orbital angular momentum states of photons. *Nature*, 412(6844):313–316.

[Manz et al., 2007] Manz, S., Fernholz, T., Schmiedmayer, J., and Pan, J.-W. (2007). Collisional decoherence during writing and reading quantum states. *Phys. Rev. A*, 75(4):040101.

[Marangos, 1998] Marangos, J. P. (1998). Electromagnetically induced transparency. *Journal of Modern Optics*, 45(3):471–503.

[Massar and Popescu, 1995] Massar, S. and Popescu, S. (1995). Optimal extraction of information from finite quantum ensembles. *Phys. Rev. Lett.*, 74(8):1259–1263.

[Matsukevich et al., 2005] Matsukevich, D. N., Chanelière, T., Bhattacharya, M., Lan, S.-Y., Jenkins, S. D., Kennedy, T. A. B., and Kuzmich, A. (2005). Entanglement of a photon and a collective atomic excitation. *Phys. Rev. Lett.*, 95(4):040405.

[Maurer et al., 2012] Maurer, P. C., Kucsko, G., Latta, C., Jiang, L., Yao, N. Y., Bennett, S. D., Pastawski, F., Hunger, D., Chisholm, N., Markham, M., Twitchen, D. J., Cirac, J. I., and Lukin, M. D. (2012). Room-temperature quantum bit memory exceeding one second. *Science*, 336(6086):1283–1286. PMID: 22679092.

[Mendes et al., 2013] Mendes, M. S., Saldanha, P. L., Tabosa, J. W. R., and Felinto, D. (2013). Dynamics of the reading process of a quantum memory. *New J. Phys.*, 15(7):075030.

[Miller et al., 2005] Miller, R., Northup, T. E., Birnbaum, K. M., Boca, A., Boozer, A. D., and Kimble, H. J. (2005). Trapped atoms in cavity QED: coupling quantized light and matter. *J. Phys. B: At. Mol. Opt. Phys.*, 38(9):S551.

[Mishina et al., 2011] Mishina, O. S., Scherman, M., Lombardi, P., Ortalo, J., Felinto, D., Sheremet, A. S., Bramati, A., Kupriyanov, D. V., Laurat, J., and Giacobino, E. (2011). Electromagnetically induced transparency in an inhomogeneously broadened lambda transition with multiple excited levels. *Phys. Rev. A*, 83(5):053809.

[Molina-Terriza et al., 2005] Molina-Terriza, G., Vaziri, A., Ursin, R., and Zeilinger, A. (2005). Experimental quantum coin tossing. *Phys. Rev. Lett.*, 94(4):040501.

[Moretti et al., 2009] Moretti, D., Felinto, D., and Tabosa, J. W. R. (2009). Collapses and revivals of stored orbital angular momentum of light in a cold-atom ensemble. *Phys. Rev. A*, 79(2):023825.

N

[Nicolas et al., 2013] Nicolas, A., Veissier, L., Giner, L., Giacobino, E., Maxein, D., and Laurat, J. (2013). A quantum memory for orbital angular momentum photonic qubits. arXiv e-print 1308.0238.

[Novikova et al., 2007] Novikova, I., Gorshkov, A. V., Phillips, D. F., Sørensen, A. S., Lukin, M. D., and Walsworth, R. L. (2007). Optimal control of light pulse storage and retrieval. *Phys. Rev. Lett.*, 98(24):243602.

[Nunn et al., 2008] Nunn, J., Reim, K., Lee, K. C., Lorenz, V. O., Sussman, B. J., Walmsley, I. A., and Jaksch, D. (2008). Multimode memories in atomic ensembles. *Phys. Rev. Lett.*, 101(26):260502.

[Nunn et al., 2007] Nunn, J., Walmsley, I. A., Raymer, M. G., Surmacz, K., Waldermann, F. C., Wang, Z., and Jaksch, D. (2007). Mapping broadband single-photon wave packets into an atomic memory. *Phys. Rev. A*, 75(1):011401.

O

[Ortalo et al., 2009] Ortalo, J., Cviklinski, J., Lombardi, P., Laurat, J., Bramati, A., Pinard, M., and Giacobino, E. (2009). Atomic-ensemble-based quantum memory for sideband modulations. *J. Phys. B: At. Mol. Opt. Phys.*, 42(11):114010.

P

[Peyronel et al., 2012] Peyronel, T., Firstenberg, O., Liang, Q.-Y., Hofferberth, S., Gorshkov, A. V., Pohl, T., Lukin, M. D., and Vuletić, V. (2012). Quantum nonlinear optics with single photons enabled by strongly interacting atoms. *Nature*, 488(7409):57–60.

[Phillips et al., 2008] Phillips, N. B., Gorshkov, A. V., and Novikova, I. (2008). Optimal light storage in atomic vapor. *Phys. Rev. A*, 78(2):023801.

[Pugatch et al., 2007] Pugatch, R., Shuker, M., Firstenberg, O., Ron, A., and Davidson, N. (2007). Topological stability of stored optical vortices. *Phys. Rev. Lett.*, 98(20):203601.

R

[Radnaev et al., 2010] Radnaev, A. G., Dudin, Y. O., Zhao, R., Jen, H. H., Jenkins, S. D., Kuzmich, A., and Kennedy, T. a. B. (2010). A quantum memory with telecom-wavelength conversion. *Nat Phys*, 6(11):894–899.

[Reim et al., 2011] Reim, K. F., Michelberger, P., Lee, K. C., Nunn, J., Langford, N. K., and Walmsley, I. A. (2011). Single-photon-level quantum memory at room temperature. *Phys. Rev. Lett.*, 107(5):053603.

[Reim et al., 2010] Reim, K. F., Nunn, J., Lorenz, V. O., Sussman, B. J., Lee, K. C., Langford, N. K., Jaksch, D., and Walmsley, I. A. (2010). Towards high-speed optical quantum memories. *Nat Photon*, 4(4):218–221.

[Rieländer et al., 2013] Rieländer, D., Kutluer, K., Ledingham, P., Gündoğan, M., Fekete, J., Mazzera, M., and de Riedmatten, H. (2013). Quantum storage of heralded single photons in a praseodymium doped crystal. *arXiv:1310.8261 [quant-ph]*.

[Ringot et al., 2001] Ringot, J., Szriftgiser, P., and Garreau, J. C. (2001). Subrecoil raman spectroscopy of cold cesium atoms. *Phys. Rev. A*, 65(1):013403.

[Ritter et al., 2012] Ritter, S., Nölleke, C., Hahn, C., Reiserer, A., Neuzner, A., Uphoff, M., Mücke, M., Figueroa, E., Bochmann, J., and Rempe, G. (2012). An elementary quantum network of single atoms in optical cavities. *Nature*, 484(7393):195–200.

S

[Sabooni et al., 2010] Sabooni, M., Beaudoin, F., Walther, A., Lin, N., Amari, A., Huang, M., and Kröll, S. (2010). Storage and recall of weak coherent optical pulses with an efficiency of 25%. *Phys. Rev. Lett.*, 105(6):060501.

[Safavi-Naeini et al., 2011] Safavi-Naeini, A. H., Alegre, T. P. M., Chan, J., Eichenfield, M., Winger, M., Lin, Q., Hill, J. T., Chang, D. E., and Painter, O. (2011). Electromagnetically induced transparency and slow light with optomechanics. *Nature*, 472(7341):69–73.

[Saglamyurek et al., 2011] Saglamyurek, E., Sinclair, N., Jin, J., Slater, J. A., Oblak, D., Bussières, F., George, M., Ricken, R., Sohler, W., and Tittel, W. (2011). Broadband waveguide quantum memory for entangled photons. *Nature*, 469(7331):512–515.

[Sangouard et al., 2011] Sangouard, N., Simon, C., de Riedmatten, H., and Gisin, N. (2011). Quantum repeaters based on atomic ensembles and linear optics. *Rev. Mod. Phys.*, 83(1):33–80.

[Sangouard and Zbinden, 2012] Sangouard, N. and Zbinden, H. (2012). What are single photons good for? *Journal of Modern Optics*, 59(17):1458–1464.

[Scherman, 2012] Scherman, M. (2012). *Transparence induite électromagnétiquement et mémoires quantiques sur la raie D2 du césium : effet de l'élargissement inhomogène dans une structure atomique multi-niveaux*. PhD thesis, Université Pierre et Marie Curie, Paris, France.

[Scherman et al., 2012] Scherman, M., Mishina, O. S., Lombardi, P., Giacobino, E., and Laurat, J. (2012). Enhancing electromagnetically-induced transparency in a multilevel broadened medium. *Opt. Express*, 20(4):4346–4351.

[Sherson et al., 2006] Sherson, J. F., Krauter, H., Olsson, R. K., Julsgaard, B., Hammerer, K., Cirac, I., and Polzik, E. S. (2006). Quantum teleportation between light and matter. *Nature*, 443(7111):557–560.

[Shor, 1994] Shor, P. (1994). Algorithms for quantum computation: discrete logarithms and factoring. In *Proceedings, 35th Annual Symposium on Foundations of Computer Science, 1994 Proceedings*, pages 124–134.

[Simon et al., 2010] Simon, C., Afzelius, M., Appel, J., Boyer de la Giroday, A., Dewhurst, S. J., Gisin, N., Hu, C. Y., Jelezko, F., Kröll, S., Müller, J. H., Nunn, J., Polzik, E. S., Rarity, J. G., De Riedmatten, H., Rosenfeld, W., Shields, A. J., Sköld, N., Stevenson, R. M., Thew, R., Walmsley, I. A., Weber, M. C., Weinfurter, H., Wrachtrup, J., and Young, R. J. (2010). Quantum memories. *The European Physical Journal D*, 58(1):1–22.

[Simon et al., 2007] Simon, J., Tanji, H., Thompson, J. K., and Vuletić, V. (2007). Interfacing collective atomic excitations and single photons. *Phys. Rev. Lett.*, 98(18):183601.

[Sipahigil et al., 2012] Sipahigil, A., Goldman, M. L., Togan, E., Chu, Y., Markham, M., Twitchen, D. J., Zibrov, A. S., Kubanek, A., and Lukin, M. D. (2012). Quantum interference of single photons from remote nitrogen-vacancy centers in diamond. *Phys. Rev. Lett.*, 108(14):143601.

[Specht et al., 2011] Specht, H. P., Nölleke, C., Reiserer, A., Uphoff, M., Figueroa, E., Ritter, S., and Rempe, G. (2011). A single-atom quantum memory. *Nature*, 473(7346):190–193.

[Steck, 1998] Steck, D. A. (1998). Cesium d line data. Available onlive at http://steck.us/alkalidata (revision 2.1.4, 23 December 2010).

T

[Timoney et al., 2013] Timoney, N., Usmani, I., Jobez, P., Afzelius, M., and Gisin, N. (2013). Single-photon-level optical storage in a solid-state spin-wave memory. arXiv e-print 1301.6924.

[Tittel et al., 2010] Tittel, W., Afzelius, M., Chaneliére, T., Cone, R., Kröll, S., Moiseev, S., and Sellars, M. (2010). Photon-echo quantum memory in solid state systems. *Laser & Photonics Reviews*, 4(2):244–267.

[Togan et al., 2010] Togan, E., Chu, Y., Trifonov, A. S., Jiang, L., Maze, J., Childress, L., Dutt, M. V. G., Sørensen, A. S., Hemmer, P. R., Zibrov, A. S., and Lukin, M. D. (2010). Quantum entanglement between an optical photon and a solid-state spin qubit. *Nature*, 466(7307):730–734.

[Torres and Torner, 2011] Torres, J. P. and Torner, L. (2011). *Twisted Photons: Applications of Light with Orbital Angular Momentum*. Wiley-VHC.

[Tremblay and Jacques, 1990] Tremblay, P. and Jacques, C. (1990). Optical pumping with two finite linewidth lasers. *Phys. Rev. A*, 41(9):4989–4999.

V

[Vaziri et al., 2002] Vaziri, A., Weihs, G., and Zeilinger, A. (2002). Superpositions of the orbital angular momentum for applications in quantum experiments. *Journal of Optics B: Quantum and Semiclassical Optics*, 4(2):S47–S51.

[Veissier et al., 2013] Veissier, L., Nicolas, A., Giner, L., Maxein, D., Sheremet, A. S., Giacobino, E., and Laurat, J. (2013). Reversible optical memory for twisted photons. *Opt. Lett.*, 38(5):712–714.

W

[Wal et al., 2003] Wal, C. H. v. d., Eisaman, M. D., André, A., Walsworth, R. L., Phillips, D. F., Zibrov, A. S., and Lukin, M. D. (2003). Atomic memory for correlated photon states. *Science*, 301(5630):196–200. PMID: 12764202.

[Wigner, 1932] Wigner, E. (1932). On the quantum correction for thermodynamic equilibrium. *Phys. Rev.*, 40(5):749–759.

[Wootton, 2012] Wootton, J. R. (2012). Quantum memories and error correction. *Journal of Modern Optics*, 59(20):1717–1738.

X

[Xu et al., 2008] Xu, X., Sun, B., Berman, P. R., Steel, D. G., Bracker, A. S., Gammon, D., and Sham, L. J. (2008). Coherent population trapping of an electron spin in a single negatively charged quantum dot. *Nat Phys*, 4(9):692–695.

Z

[Zhang et al., 2011] Zhang, S., Zhou, S., Loy, M. M. T., Wong, G. K. L., and Du, S. (2011). Optical storage with electromagnetically induced transparency in a dense cold atomic ensemble. *Opt. Lett.*, 36(23):4530–4532.

[Zhao et al., 2009] Zhao, R., Dudin, Y. O., Jenkins, S. D., Campbell, C. J., Matsukevich, D. N., Kennedy, T. a. B., and Kuzmich, A. (2009). Long-lived quantum memory. *Nat Phys*, 5(2):100–104.

[Zhou et al., 2012a] Zhou, S., Zhang, S., Liu, C., Chen, J. F., Wen, J., Loy, M. M. T., Wong, G. K. L., and Du, S. (2012a). Optimal storage and retrieval of single-photon waveforms. *Opt. Express*, 20(22):24124–24131.

[Zhou et al., 2012b] Zhou, Z.-Q., Lin, W.-B., Yang, M., Li, C.-F., and Guo, G.-C. (2012b). Realization of reliable solid-state quantum memory for photonic polarization qubit. *Phys. Rev. Lett.*, 108(19):190505.